Modeling, Analysis and Advanced Control of Voltage- and Current-Source Converters in Renewable Energy-Based Active Distribution Systems

by

Amr Ahmed Abdelsalam Radwan

A thesis submitted in partial fulfillment of the requirements for the degree of

Doctor of Philosophy

in

Energy Systems

Department of Electrical and Computer Engineering
University of Alberta

Abstract

This thesis addresses the integration of renewable energy resources into the grid-connected and isolated distribution systems using voltage- and current-source converters. Motivated by its promising potential and attractive features, a one-stage current-source converter (CSC) is selected as an effective interfacing device for the photovoltaic (PV) generators to the utility-grid. The operation of the grid-connected CSC-based PV system is investigated under different operating conditions, parameters variation, and control topologies. From the dc-side, it is found that the variation in the weather conditions, e.g., solar irradiance levels, might affect the dynamic performance of the vector-controlled grid-connected CSCs. Small-signal dc-side impedance models for the CSC and the PV generators are developed to investigate the system stability. Active compensation techniques are proposed so that the system performance is well maintained under different operating points. From the ac-side, a susceptible potential to instabilities is yielded under the very weak grid conditions. This potential significantly increases in the vector-controlled converters. The implementation of the phase-locked loop (PLL) is found to have a detrimental impact on the system stability as the grid impedance increases. Two solutions for the very weak grid integration have been proposed. Firstly, the power synchronization control (PSC) scheme is developed for CSCs in PV applications so that the PLL is no longer needed, and hence a seamless integration to the very weak grid is achieved. Secondly, supplementary compensation loops are proposed and added to the conventional PLL-based vector-controlled CSC so that the negative impacts of the PLL are completely alleviated. In both cases, small-signal state-space models are developed to investigate the system stability and provide a detailed design approach for the proposed controllers.

A larger system level integration is considered in this thesis by interfacing multiple distributed generation (DG) units to the conventional distribution system. A generalized hybrid alternating-current (ac)/direct-current (dc) system that constitutes ac and dc subgrids is created to efficiently accommodate the dc-type renewable sources (such as PVs, batteries, fuel cells, etc.) to the ac-type conventional distribution system. Both subgrids are interconnected using voltage-source converters (VSCs) to facilitate a bidirectional power exchange via multiple inversion-rectification processes. To achieve an accurate and efficient operation, a supervisory power management algorithm is proposed. The algorithm operates successfully regardless of the control mode of the individual DG units. However, the integration of severe dynamic loads, such as direct online inductions motors (IMs) into the ac-side of the hybrid system reflects very lightly damped modes, which in turns induce instabilities, particularly in the isolated mode of operation. Therefore, active compensation techniques have been proposed to increase the system damping.

Throughout this thesis, time domain simulations under Matlab/Simulink® environment for the systems under study are presented to validate the analytical results and show the effectiveness of the proposed techniques.

Preface

This thesis is an original work by Amr Radwan. As detailed in the following, some chapters of this thesis have been published or accepted for publication as scholarly articles in which Prof. Yasser A.-R. I. Mohamed was the supervisory author and has contributed to concepts formations and the manuscript composition.

Chapter 3 of this thesis has been published as Amr A. A. Radwan and Y. A.-R. I. Mohamed, “Analysis and active suppression of ac- and dc-side instabilities in grid-connected current-source converter-based photovoltaic system,” *IEEE Transactions on Sustainable Energy*, vol. 4, no. 3, pp. 630-642, July 2013.

Chapter 4 has been submitted for possible publication in *IEEE Transactions on Energy Conversion*.

Chapter 5 has been published as Amr A. A. Radwan and Y. A.-R. I. Mohamed, “Improved vector control strategy for current-source converters connected to very weak grids,” *IEEE Transactions on Power Systems*, in press [available online].

Chapter 6 of this thesis has been published as Amr A. A. Radwan and Y. A.-R. I. Mohamed, “Stabilization of medium-frequency modes in isolated microgrids supplying direct online induction motor loads,” *IEEE Transactions on Smart Grid*, vol. 5, no. 1, pp. 358-370, January 2014.

Chapter 7 of this thesis has been accepted for publication as Amr A. A. Radwan and Y. A.-R. I. Mohamed, “Networked power management and control of AC-DC hybrid microgrid,” *IEEE Systems Journal*, in press [available online].

Acknowledgements

I would like to express my deep gratitude to my supervisor, Prof. Yasser A.-R. I. Mohamed, for his guidance and assistance during my research. I appreciate all his contributions of time and invaluable discussions during my Ph.D. program. This thesis would not have been in this shape without his continuous encouragement and support.

I would like to express my thanks to the examiners committee for their valued time and interests in my thesis.

I would also like to acknowledge the financial support provided by the Alberta Innovates – Technology Futures Graduate Student Scholarships.

Table of Contents

List of Tables

List of Figures

List of Acronyms

3PG	Three-phase-to-ground
AC	Alternating-current
BP	Band-pass
BPF	Band-pass filter
CL	Capacitive-inductive
CSC	Current-source converter
CSR	Current-source rectifier
d-	Direct
DC	Direct-current
DG	Distributed generation
HP	High-pass
HPF	High-pass filter
HVDC	High-voltage-dc
IGBT	Insulated-gate-bipolar-transistor
IGCT	Integrated-gate commutated-thyristor
IM	Induction motor
LCL	Inductive-capacitive-inductive
LPF	Low-pass filter
MIMO	Multi-input-multi-output
MPP	Maximum power point
MTDC	Multi-terminal-dc

p.u.	Per unit
PCC	Point-of-common-coupling
PI	Proportional-and-integral
PLL	Phase-locked-loop
PSC	Power synchronization control
PV	Photovoltaic
PWM	Pulse-width-modulation
q-	Quadrature
SCR	Short circuit ratio
SISO	Single-input-single-output
SLG	Single-line-to-ground
SRF	Synchronous reference-frame
VSC	Voltage-source converter
VSI	Voltage-source inverter
VSR	Voltage-source rectifier

Chapter 1

Introduction

1.1 Research Motivations

Driven by environmental and economic concerns against the fossils-based power generation, distributed generation (DG) systems are gaining a high momentum to facilitate the integration of renewable energy resources into the alternating-current (ac) system. The ongoing deployment of individual DG units naturally creates active distribution systems, referred to as microgrids, which can operate in the grid-connected or the islanded mode.

In the grid-connected systems, power electronic converters are utilized as interfacing devices to regulate the injected ac current, support the utility-grid, and achieve a satisfied level of power quality. Voltage-source converters (VSCs) are widely adopted as a grid interface. However, many attractive features give the current-source converter (CSC) the potential to be a competitive interfacing device in the grid-connected applications. In this thesis, the interconnection of the CSC as an interfacing device between the renewable energy resources and the grid is investigated. Amongst renewable energy resources, the utilization of photovoltaic (PV) generators is increasing with no signs of slowing down, and hence they are considered as the main source of the direct-current (dc) power of the grid-connected CSCs in this thesis.

On the device-level integration of renewable energy resources, the interconnection of the CSC-based PV generator to the utility-grid is subjected to several challenges that might affect the system performance and stability. From the dc-side, the system performance can be affected following the variations in the solar irradiation levels. On the ac-side, the impedance of the grid might interact with the CSC dynamics and eventually leading to instabilities. Moreover, the lightly damped modes influenced by the resonance of the equivalent capacitive-inductive (CL) filter negatively affect the system performance.

The device-level integration of the grid-connected CSC systems is expanded to a large-scale level where multiple DG units are interconnected. As the nature of renewable energy resources, e.g., PV systems, is dc whereas the conventional distribution system is ac, a hybrid mix of an interconnected ac and dc power electronic-based distribution system is created. A typical hybrid system constitutes two (or more) ac and dc subgrids (or microgrids); each combines local loads (static and dynamic) and individual DG units. The interconnection of the ac and dc subgrids is achieved by one (or more) VSC to facilitate a bidirectional power exchange. As the renewable energy resources are intermittent, the main challenge is to secure a continuous and adequate supply under all modes of operation especially when the utility-grid is intentionally disconnected; i.e., the hybrid system operates in the standalone mode. In this situation, preserving the system reliability with minimal energy disruptions or load shedding is at the highest priority. The coordination control of the hybrid system can be achieved by autonomous schemes. However, it is shown that the autonomous control fails to operate in large-scale islanded hybrid systems owing to the multiple variations in the power generation characteristics of the individual DG units (such as droop coefficients or set points variations, loss/connection of individual DG units, etc.) Therefore, a smart power management algorithm is necessary to maximize the benefits from the renewable energy resources, minimize the power losses, and increase the system reliability. The algorithm should be attributed by its generality and scalability such that it can be easily implemented in the large scale hybrid systems. It should also be independent of the local generation characteristics and control topologies. Beside the static loading conditions, e.g., resistive loads, direct online induction motors (IMs) are considered as dynamic loads at the ac-side of the hybrid system in order to investigate their influence on the overall system stability.

1.2 Research Objectives

This thesis aims to facilitate the integration of the renewable energy resources on two levels. The first is a device-level where the integration of PV generators to the utility-grid is effectively achieved by CSCs with proposed compensation techniques and controllers. The second is a system-level where multiple DG units as well as distributed static and dynamic loads are integrated via the hybrid ac/dc grid structure. The objectives of this thesis are as follows.

- Preserving the stability of the vector-controlled grid-connected CSC-based PV systems under different operating points and weather conditions by developing linear active compensation techniques.
- Facilitating a seamless integration of the grid-connected CSC-based PV systems to the very weak grid by developing the power synchronization control (PSC) for CSCs.

- The mitigation of the negative impacts of the phase-locked-loop (PLL)-based vector control of the CSCs in the very weak grid systems using supplementary linear active compensation techniques.
- The development of a supervisory coordination algorithm in the hybrid ac/dc system to allow accurate, efficient, and reliable operation following variable loading conditions especially in the isolated mode of operation.
- The development of active compensation techniques to facilitate the integration of direct online IM loads to the supplying vector-controlled VSCs at the ac-side of the hybrid ac/dc system in the isolated mode of operation.

1.3 Thesis Contributions

The key contributions of this thesis are as follows.

- Enabling effective and stable integration of PV generators using the actively-compensated vector-controlled CSCs under a wide variation range of operating points.
- Enabling a successful operation of the grid-connected CSC-based PV systems under the very-weak grid conditions using two approaches; the PLL-less PSC topology, and the active compensation techniques in the conventional vector control structure.
- Developing a smart supervisory power management algorithm for multiple DG units in the environment of the hybrid ac/dc grid.
- Facilitiating a successful integration of the direct online IMs to the ac-side of the hybrid systems in the isolated mode of operation using active compensation techniques.

1.4 Thesis Organization

The remainder of this thesis is organized as following. A literature survey is introduced in Chapter 2. Chapter 3 addresses the interaction dynamics between the grid-connected CSC and the PV generator. A thorough analysis is conducted using the small-signal dc-side impedance models of both entities. Active compensation techniques are then proposed to ensure a stable performance under different operating conditions. The PSC of the grid-connected CSC-based PV system is introduced in Chapter 4. Small-signal stability analysis is conducted to ensure the system stability. A systematic design approach for the CSC controllers is also shown in details. Unlike the PSC topology in Chapter 4, Chapter 5 maintains the vector control strategy for the

CSCs while preserving the system stability under the very weak grid conditions. The negative impacts of the PLL are mitigated by proposing supplementary active compensation techniques.

To facilitate the realization of the hybrid ac/dc system under different loading conditions, Chapter 6 investigates the integration of direct online IM loads to the isolated VSC-based ac subgrid. Small-signal impedance models of the VSC supplying units and the IM loads are developed to evaluate the system stability. Active compensation techniques are developed to allow a stable performance under different operating conditions. In Chapter 7, a dc subgrid is interfaced to the ac subgrid system using a bidirectional VSC to realize the hybrid ac/dc grid. A smart supervisory control algorithm is proposed to ensure an accurate power management under different loading conditions.

Finally, the summary of this thesis and the future work are detailed in Chapter 8.

Chapter 2

Literature Survey

2.1 Power Electronic Converters in Distributed Generation Systems

As most of renewable energy resources have an intermittent unregulated nature, they have to be interfaced by power electronic converters in order to ensure a maximum power point (MPP) operation and inject a controlled ac current to the utility-grid at a desired power factor [1]-[2].

In the grid integration, VSCs are widely adopted as an interfacing stage [1]-[2]. However, many attractive features give CSCs the potential to be a competitive interfacing device [3]-[5]. The recent advances in semiconductors and magnetic components help CSCs to gain a wide acceptance in many other applications such as wind farms [6], PV systems [7]-[10], static synchronous compensators [11], motor drives [12], high-voltage-dc (HVDC) [13]-[14], etc. As a brief comparison, the key characteristics of VSCs and CSCs are summarized as follow [3]-[5], [10].

1) The controlled dc input in the VSC is the dc-link voltage whereas the dc current is the controlled input in the CSC which is a desirable feature in the PV applications.
2) The dc-side element in the VSC is a capacitor whereas it is a choke in the CSC. The power losses in the dc choke is usually $2\%-4\%$ whereas it is around 0.5% in the dc-link capacitor.
3) The reliability of the dc choke is much higher than the electrolytic dc-link capacitor. The reliability of the dc-link capacitors significantly increases (e.g., up to $40{,}000$ hours) if the newly improved film capacitors are used. However, film capacitors are still challenged by a relatively high price and less capacitance per unit volume as compared with the electrolytic type.
4) The semiconductor switch in the VSC is usually the insulated-gate-bipolar-transistor (IGBT). An additional diode has to be added in series with each IGBT if it is used in CSCs to increase the reverse voltage withstanding capability, but this almost doubles the switching losses. However, the recently developed reverse-blocking IGBT and the integrated-gate commutated-thyristor (IGCT) switches that withstand high reverse

voltages are emerging; therefore there will be no need for the added series diode.

5) CSC offers additional short-circuit protection as compared to the VSC due to the directly controlled dc current. However, CSC can be prone to a breakdown under the open circuit operation or sudden loss of the dc current flow.
6) VSC is a buck inverter as the dc-link voltage should be at least twice the maximum of the ac phase voltage to avoid over-modulation. However, the output dc voltage of the PV arrays is typically low which might require either a step-up transformer at the ac-side or an intermediate boost dc/dc converter. On the contrary, the CSC is a boost inverter and, therefore, is more flexible to facilitate the PV-grid integration.

2.2 Photovoltaic Solar Systems as a DC Power Source for the Grid-Connected Converters

Thanks to the progressive improvements in the PV industry, the cost of the PV-generated electricity (per watt in US$) is expected to decrease to $0.51 in 2016 as compared to $1.06 in 2011 and $1.50 in 2009 [15]. Driven by these incentives, PV systems have gained a high growth rate among other renewable resources. New installations of 38.4 GW of PV plants have been added globally in 2013, as compared to 30 GW in 2012. The global installed capacity of PV generators has been increased to 138.9 GW in 2013 [16].

According to their generation capacities, PV systems can be classified into [17]: 1) Utility-scale ground-mounted with generation capacity from 1.0 MW. 2) Large-scale for commercial applications (such as schools, hospitals, etc.) with ranges from 10-1000 kW. 3) Small scale for residential and roof-top applications with PV units up to 10 kW. 4) Off-grid networks as in remote communities or telecommunication units with different ratings [18]. Off-grid PV systems are self-contained, isolated from the utility-grid, and currently constitute less than 10% of the total PV market, whereas the small scale PV systems are usually aggregated to reduce complexity in utility studies [17]. Therefore, it is more important to investigate the integration of the large- and utility- scale PV generators to the utility-grid due to their large power generation capacity and their potential impacts on the system stability.

The basic building block of the PV generator is the PV cell that typically produces 1 to 2 W of electrical power [19]. Multiple PV cells are connected in series to form a PV module. PV modules are then stacked in parallel and series combinations to form a PV array. The state-of-art of the PV structures is classified into the centralized, the string, the multi-string, and the ac-module [1]-[2], [20]. The centralized structure consists of a combination of parallel connected PV strings; each is formed by series connected PV modules, and all are interfaced by one centralized inverter. This structure is commonly used and is positively characterized by its low cost and high conversion efficiency as one interfacing inverter is only utilized. In the string structure, the PV system is interfaced to the utility-grid by one inverter per PV string. The primarily advantage is that the MPP tracking can be separately achieved for each string and therefore better efficiency is yielded. However, the cost is obviously higher due to the additional number of interfacing inverters. The string structure is expanded to the multi-string scheme by interfacing each string by a dc/dc converter to boost the dc-link voltage. A common inverter is then used to interface the PV system to the ac-side. The most recent PV structure is the ac-module which consists of multiple PV modules; each is interfaced by its own inverter. The future extension of this topology is flexible. The reliability is very high as there is no single-point of failure.

The power electronic interface for PV systems are classified into the following [1], [19], [20]. 1) A two-stage system that constitutes a dc/dc converter to achieve the MPP tracking, and a dc/ac inverter to inject the controlled ac current into the utility-grid. Clearly, this category includes the multi-string PV structure. 2) One-stage in which one dc/ac inverter is implemented to achieve the MPP tracking and control the injected ac current. This category includes the centralized PV structure. The one-stage structure reduces the power losses, cost, and system bulk and is a widely adopted configuration by major PV manufacturers [19], and hence this topology is considered in this thesis.

2.3 DC-Side Interactions in the Grid-Connected Converter-Based Photovoltaic Generators

The stability analysis and dynamic performance enhancement of the grid-connected PV systems are gaining high interest in the literature. Some issues regarding the destabilizing dc-side interaction dynamics between the grid-connected converter and the PV systems have been discussed in [7], [22]-[24]. The influence of the variable weather conditions, particularly the solar irradiation, on the generated PV power and the associated impacts on the dynamic performance of the utility-grid has been tackled in [8]-[9], [25].

The negative impact of the non-linearity of the PV array model on the dynamic performance of the interfacing VSC and CSC has been alleviated in [22] and [7], respectively. The generated PV power is measured and added to the reference value of the active current component, and hence the dynamics between the dc and ac side of the interfacing converter are decoupled. A comparison between the performance of both CSC- and VSC-based PV systems is presented in [7] by conducting some simulation scenarios. It is found that the inherent over-current protection in the CSC is much better than VSC-based systems due to the regulation of the input dc current in CSCs.

A design rule to minimize the value of the dc-link capacitor of the grid-connected one- and two-stage VSC-based PV systems has been proposed in [23] so that the low-reliability electrolytic capacitors can be replaced by the small capacitance high-reliability film types. It is shown that there is a right-hand pole appearing in the control dynamics of the PV systems when the PV generator is operating at voltages lower than the MPP. This pole is correlated to the cross-over frequency of the dc voltage controller, the dc-link capacitance, and the operating point of the PV generator. As the cross-over frequency (or approximately the bandwidth) of the dc voltage controller increases, the required capacitance per ampere to maintain a stable response decreases. An accurate selection of the dc-link capacitance is, therefore, mandatory so that the system stability is preserved. Similar conclusions have been drawn in [24] with further investigations on the dynamic properties of the PV generator to accurately emulate the PV behavior by a power electronic substitute.

In [25], a zero dynamic feedback linearization technique has been applied to design a nonlinear dc-link voltage controller for the grid-connected VSC-based PV system. The system nonlinearities are transferred into a partial linear subsystem and a nonlinear autonomous system. The proposed controller is capable of running the grid-connected PV system under variable solar irradiation levels. However, the system performance has not been tested when the conventional proportional-and-integral (PI) controllers are implemented to justify the complexity of implementing a nonlinear controller.

2.4 AC-Side Interactions in the Grid-Connected Converter-Based Photovoltaic Generators

An accurate model of a three-phase grid-connected one-stage VSC-based PV system with a high order inductive-capacitive-inductive (LCL) filter is developed in [26], in the synchronous rotating direct (d)-and-quadrature (q) reference frame. A sensitivity analysis has been conducted to investigate the influence of the system parameters on the dynamics performance of the VSC. However, the PV-side is simply modeled as a current source injecting a constant active power, assuming a maximum power point operation. A similar system is further investigated in [27] where a proposed two degree of freedom active damping technique is presented to mitigate the ac LCL filter resonance. The control structure is implemented in the synchronous rotating d-q reference frame. The active damping method does not require an additional measurement sensor as it utilizes the existing sensor of the grid-side ac current through a low-pass filter (LPF) and a compensation gain. Similar to [26], the influence of the PV generator model on the system response has not been accurately considered.

The ac-side stability has not been sufficiently considered for the grid-connected CSC-based PV systems. However, some active damping techniques for the ac filter resonance have been addressed for the CSC in general applications [28]-[30]. The control of a current-source rectifier (CSR) in the synchronous rotating reference frame is discussed in [28]. A conventional cascaded PI dc and ac current controllers are utilized. The terminal ac capacitor of the CSR with the equivalent utility-grid inductance can induce a resonant peak that causes undesirable oscillations in the supply current. The inductor-side ac current is measured and used as an input to an active compensation function. Following the same motivation, multiple active damping methods for the ac-side CL filter resonance in CSRs are investigated in [29] where proportional, integral, and derivative states of the ac inductor current and the capacitor voltage are employed. It is found that the derivative inductor current and the proportional capacitor voltage feedbacks can significantly damp the resonance by appropriately designing their gains. A similar active damping control method for the CL resonance in the CSR operating in low switching frequency is proposed in [30] with an active compensation signal fed from the ac capacitor voltage through a high-pass filter (HPF).

A multi-level grid-connected CSC-based PV system has been proposed in [8] by connecting

n-number of CSCs in parallel where each CSC unit has its own dc choke, PV system, and the MPP algorithm. The n-converters are terminated by one ac-side capacitor so that $2n + 1$ current levels are yielded at the ac-side. The dc choke current is controlled independently by a PI controller and the outputs are summed to generate the d-component of the ac current reference. One PI ac current controller is utilized for the entire multi-level CSC system. Similar to [7] and [22], the PV power is fed-forward to the dc current control loop to mitigate the influence of the PV-side nonlinearity. It is found that a low-order harmonic current (7^{th}) is injected to the utility-grid due to the unequal irradiation levels incident on the n PV generators. Therefore, the work in [8] has been extended to [9] by proposing a supplementary PI controller to eliminate the 7^{th}-harmonics in the injected ac current. The compensation method depends on extracting the 7^{th}-order harmonics of the d-q components of the ac currents and comparing them to a reference value through a PI controller. The yielded control signal is added to the generated modulation signal.

2.5 Integration of Power Converters to the Very Weak Grids

Following the progressive improvements in the semiconductors industry, high-voltage-high-power power electronic switches ($4.5\ \mathrm{kV}, 1.2\ \mathrm{kA}$) are recently emerging the market [31]. Moreover, High-power-density converters have been developed based on the promising Silicon Carbide (SiC) technology [32]. Motivated by these advances, the proliferation rate of high-power three-phase converters has been increasing in many grid-tied applications such as HVDC, multi-terminal-dc (MTDC), PV generators, and wind energy [19], [33]-[35]. Due to the nature of these applications, the power converter can be located remotely from the utility-grid (e.g., HVDC transmission and offshore wind systems). For economic and technical reasons, individual DG units can be installed at the terminals of rural feeders to support local loads [35]. In such cases, and based on the stiffness of the utility-grid, considerable interaction dynamics between the grid impedance and the power converter are yielded which can affect the overall system stability [36]-[48].

An ac system is recognized weak if it has high impedance as seen from the point-of-common-coupling (PCC) of the interconnected converter. A quantifying measure, known as the short-circuit ratio (SCR), is usually used to characterize the stiffness level of the utility-grid. The SCR is the ratio of the short-circuit capacity of the utility-grid to the rated dc power of the interconnected power converter [36]. A utility-grid is weak when $2 \leq \mathrm{SCR} \leq 3$ and very weak when $\mathrm{SCR} < 2$. The worst case scenario occurs when $\mathrm{SCR} = 1.0$ [37].

The interconnection of power converters to a weak utility-grid requires reactive power support. In the PV applications, the present practiced standards (e.g., IEEE 1547 and UL 1741) suggest that PCC voltage shall not be regulated by the PV interfacing converters [49]-[50]. These recommendations are strictly followed in the distributed rooftop PV panels and some utility-scale applications [7], [22]. However, some other work adopts the regulation of the PCC voltage by the utility-scale PV inverters [19], [51]-[56]. A reactive-power/PCC-voltage droop control method is proposed in [52] so that the PCC voltage is controlled without exceeding the ratings of the interfacing converter. Another work in [53] uses the Youla parameterization method to regulate the PCC voltage of the PV generator. An algorithm is proposed in [54] to inject a controlled active power from zero up to the MPP while the PCC voltage is continuously regulated. On the transmission level, it is shown that the reactive power support of the utility-scale PV inverters positively contributes to the damping of the PCC voltage and frequency oscillations following three-phase faults [55]-[56]. However, this positive impact is restricted to the relatively strong utility-grids as the vector-controlled converters have limited stability boundaries in weak-grid conditions as discussed in the following subsection.

2.5.1 Conventional Vector Control

In the literature, extensive research work has been conducted to address the connection of VSCs to weak utility-grid [36]-[44]. Under weak-grid conditions, vector-controlled VSCs suffer from instability and degraded performance due to the implementation of the synchronous reference frame (SRF) PLL [38]-[42]. To preserve the system stability, major limitations on the amount of injected active power to the weak grid should be considered. At $\mathrm{SCR} = 1.0$, no more than 0.4 per unit (p.u.) of active power could be injected from the conventional vector-controlled VSC [43]. In the most promising cases, a $0.6 - 0.7\ \mathrm{p.u.}$ of active power could be injected [37], [44]. It is reported that the high bandwidth PLL contributes to the increase of the negative real part of the inverter output impedance (particularly in the q-q channel), and hence the converter does not act as a passive system, which in turn challenges the system damping [38]. A similar behavior is reported in [39] where the incremental negative resistance is found to be independent of the PLL structure (e.g., SRF-PLL, Decoupled-Double-SRF-PLL). A detailed modeling and analysis of the low frequency dynamics of the PLL under different grid impedances, loads, and modes of operation is presented in [40]. A coordination scheme between the PLL and the dc voltage controllers of a VSC connected to a weak grid is introduced in [41] in order to enhance the system damping. In spite of the interesting insights in [38]-[41], the negative impact of PLL on the power converters connected to a weak grid has not been alleviated. The work in [42] suggests the reduction of the PLL gains to small values in order to avoid instabilities. However, these reductions negatively affect the damping and the dynamic response of the system.

In the grid-connected converters, the magnitude of the output impedance of a current-controlled converter should be maximized so that the grid impedance has minimal interactions with the converter dynamics [45]. Following this guideline, the work in [42]-[47] introduces impedance shaping techniques for single-phase inverters to actively increase their output impedance in the presence of a high grid inductance. However, the influence of the PLL dynamics on the developed analytical models has not been considered. More importantly, the minimum value of the considered SCR level in [47] is 10 which is only reasonable in low power applications and single-phase converters. In high power three-phase converters, a unity SCR level is usually considered as a worst case scenario [36]-[37]. In [48], an adaptive feed-forward and current regulation scheme have been implemented for single-phase converters. The scheme depends on the estimation of the grid impedance to ensure a satisfactory performance. In [37], an improved vector control topology based on a gain-scheduling of the outer loops is introduced. The proposed controller comprises eight parameters whereas an H_∞ fixed-structure control design methodology is followed for parameters tuning. Moreover, lookup tables should be utilized to achieve the gain-scheduling scheme to follow the variation of operating points. Referring to [37] and [48], a more simple, yet effective, vector-control-based technique is still demanded to facilitate the connection of power converters to the weak grid systems.

2.5.2 Power Synchronization Control

To overcome undesirable interaction dynamics between the grid impedance and the PLL in the vector-controlled VSCs, an alternative controller, referred to as PSC, has been proposed [36], [44]. In this technique, there is no need for the PLL and the inner current controller. An active power controller generates the synchronization angle necessary for the orientation of the rotating reference frame, whereas a voltage controller is utilized to determine the magnitude of the inverter terminal voltage. The PSC method yields a fast and stable performance at the very low SCR values.

Using the PSC, the grid-connected VSC located nearby a large synchronous machine does not have negative impacts on the sub-synchronous dynamics [57]. On the contrary, the vector controlled system is found to have a potential to degrade the system stability under similar conditions [58].

In spite of being a promising technique, the PSC still has the following drawbacks. 1) The quadrature component of the PCC voltage is no longer zero, and hence there is no definition for the active and reactive current components. 2) As there is no a direct enforcement on the injected current components, the PSC has to switch to the vector current control at fault instants to set current limits [44]. Moreover, the PSC has not been investigated for the grid-connected CSC-based PV systems.

2.6 System Level Integration of Multiple Distributed Generation Units in the Hybrid AC/DC Grid Environment

The ongoing deployment of the distributed renewable-based sources, including PV units, into the conventional distribution system to supply local loads creates active islands, which are referred to as microgrids or subgrids. Microgrids can operate either in the grid-connected or intentionally islanded mode and are classified into ac or dc types [59]. The distinct features of ac and dc microgrids are; 1) AC microgrids are more compatible with the existing ac distribution system. However, the synchronization of the frequency, the phase angle, and the PCC voltage should be considered prior to closing the interfacing static switch [60]. On the contrary, the connection of a dc microgrid to the ac utility-grid is simple. 2) DC microgrids meet the inherent dc nature of most nowadays loads (e.g., home appliances, lighting systems, data centers, and motor drives, etc. [59]). Moreover, most of renewable energy resources are dc, such as PV generators, fuel cells, and energy storage units. 3) Complicated electromechanical protection devices and coordination schemes challenge dc systems due to the absence of the zero-current-crossing behavior that provides an inherent self-extinguish feature of the ac fault current [61]. 4) AC systems are associated with transmission lines skin effects whereas dc transmission systems are more efficient [62]. As most of renewable energy resources are dc whereas the conventional distribution system is ac, the concept of the ac/dc hybrid active distribution systems is emerging in order to interface the dc renewables to the ac systems, combine the benefits of both generation types, reduce the system losses by avoiding multiple conversion stages, and increase the system reliability [62]-[85].

In the literature, the operation of the grid-connected or islanded ac and dc microgrids is well-established [86]. However, the interconnection between both subgrids to form a hybrid system requires a special attention. The research work on hybrid systems can be classified into dynamics and stability improvements [63]-[66] and the real-time power management using autonomous schemes [67]-[81] or supervisory controllers [82]-[85].

2.6.1 Autonomous Control of the Hybrid AC/DC System

An islanded hybrid system that constitutes a dc bus aggregating a wind turbine, batteries, and dc loads; and an ac bus that interfaces the dc system to a diesel generator and ac loads via a bidirectional VSC is proposed in [67]. The hybrid system contains electrical water heaters as controllable dc loads which are controlled via dc droop loops to suppress any fluctuations in the dc bus voltage. In [68], a hierarchical active power management strategy for a medium voltage islanded hybrid system that includes fuel cells as a main source and super capacitors as a complementary source has been proposed. The systems in [67]-[68] are tailored to satisfy a specific objective, and, therefore, the proposed controllers might not be generalized to a larger scale hybrid systems.

A more generalized islanded hybrid system structure is considered in [69]-[72] where two islanded droop-based ac and dc subgrids are interconnected by a VSC. An autonomous control method for the interconnecting VSC is proposed in [69]. The measurements of the normalized frequency and dc voltage at the terminals of the interfacing converter are used to estimate the local ac and dc subgrid loading. The same autonomous method has been utilized in [70] when an energy storage unit is considered. This work has been extended to [71] to consider the parallel operation of the interconnecting VSCs. Another autonomous method has been proposed in [72]-[73] by applying the difference between the normalized frequency and dc voltage across the interconnecting converter over a PI controller to determine the positive or negative power reference. The autonomous control method of the interfacing VSC in [72]-[73] might deviate slightly from the ideal conditions when being implemented in the parallel operated interfacing converters [71]. More importantly, the operation of the autonomous methods in [69]-[73] depends on the summation of the individual droop characteristics in both subgrids to obtain the combined power-frequency droop for the ac subgrid and the power-dc-voltage droop for the dc subgrid so that the measured frequency or dc voltage correctly reflects the actual local loading, and hence a bidirectional power flow via the interfacing VSC can be achieved accurately. However, the evaluation results only consider the case when both ac and dc subgrids are formed by a single droop-based power electronic converter and ignore the actual situation where multiple DG units are connected in parallel. The influence of the variation of the droop characteristics of the individual DG units on the accurate operation of the hybrid system has not been considered. A modified droop-based control strategy for the interconnecting VSC is proposed in [74]. The droop coefficients of the local ac sources are utilized to correlate the droops of the ac and dc subgrids.

Different grid-connected hybrid systems that are structurally tailored to fulfill certain objectives are proposed in [75]-[77]. In [75], a back-to-back converter that interfaces an ac microgrid to the utility-grid with an extended dc-link to constitute a dc subgrid is evaluated. Different power flow strategies are achieved to ensure an efficient operation. A power flow management for a grid-connected system that comprises a PV array, battery, and local loads connected to a utility-grid is proposed in [76]. A method to operate a grid-connected hybrid system formed by a PV array and fuel cell is proposed in [77]. The power management algorithm is proposed so that the PV source is operating at the MPP, and the fuel cell is maintained at its highest efficiency.

Autonomous controlled hybrid systems that are flexible to operate in the grid-connected or islanded modes are addressed in [78]-[82]. A microcontroller-based power management algorithm is presented in [78] for a residential low voltage microgrid system that combines a battery, a fuel cell, and a PV module. The power management has been proposed to estimate and control the state-of-charge of the battery to enhance the system reliability, particularly in the islanded mode of operation. The proposed system can also operate in the grid-connected mode.

The autonomous control strategy of a kW rated hybrid ac/dc system that consists of wind turbines and PV panels as renewable resources, and batteries and super-capacitors as storage units is proposed in [79]. In the grid-connected mode, the dc bus voltage is maintained by the grid-connected VSC whereas the storage units supply the difference between the renewable resources power and the local load demands. In the islanded mode of operation, the storage units maintain the dc-link voltage whereas the VSC maintains the ac voltage and frequency. A similar work has been proposed in [80] to achieve a smooth power exchange between ac and dc subgrids via an interfacing VSC in a hybrid system.

The integration of a low voltage dc subgrid consisting of PV panel, batteries, super-capacitors, and local dc loads into the conventional ac distribution system via a front-end VSC has been introduced in [81]. The autonomous control strategy of all interfacing converters are proposed such that the dc voltage is maintained stable and the individual DG units in the dc subgrid are optimally utilized.

A demonstration of a large-scale autonomously-controlled microgrid is evaluated in [82]. The system consists of 1.0 MW fuel cell, 1.2 MW PV, and two 1.2 MW diesel generators integrated with large-scale energy storage and power factor correction capacitors. The system can operate in both islanded and grid-connected modes.

2.6.2 Supervisory Control of the Hybrid AC/DC System

A centralized controller has been introduced in [83] to balance the loading condition between the ac and dc systems via multiple interconnecting VSCs. The centralized controller selects the required number of the interconnecting VSCs to operate, based on the amount of the transmitted power. However, the controller is tailored to the power-controlled DG units and might not be easily generalized to the droop-based case or mixed droop-based/power-controlled DG sources. Also, the power flow through the interconnecting converters is not minimized in some cases.

A PV system working in parallel with an energy storage unit is proposed in [84] using a local high-bandwidth smart grid communication in the real-time. The control algorithm processes the collected data from the utility-grid, individual DG units, and loads entities to generate the power reference command for the power electronic interfaces. The main goal is to continuously feed the load with maximum dependency on the full power produced from the PV system.

A double-layer hierarchical control strategy for several DG units, batteries, and loads forming an islanded dc microgrid has been proposed in [85]. In the primary level, an adaptive voltage-droop method to regulate the common dc bus voltage is implemented whereas a low-bandwidth communication interface is implemented in the second layer to achieve a supervisory control among microgrid entities. Although it is desirable to operate the PV at MPP, this is not always appropriate in isolated systems as it can lead to overcharging the batteries. Therefore, the supervisory controller aims to regulate the batteries charging and discharging in a coordinated manner to preserve their life-cycle without compromising the common voltage control.

In [86], a three-level hierarchical control strategy for the interfacing converters between ac and dc buses in a hybrid microgrid system is proposed. The interfacing converter is considered when operating in the rectification mode only. In the primary level, the decentralized dc droop, as well as current controllers, are employed. A secondary control level is included to eliminate the dc voltage deviation produced by the dc droop control using a low-bandwidth communication. The last level is the tertiary controller that is implemented to allow a seamless transfer between the dc standalone and the dc grid-connected modes. The influence of the communication delays on the overall system stability has been investigated using the small-signal stability analysis. In [87], a similar control strategy has been proposed but for the local ac and dc subgrids in the hybrid microgrid system. The power sharing between the DG units in the isolated mode of operation are enhanced using a low-bandwidth communication in [88]-[89].

2.6.3 Integration of Dynamic Loads to the AC-Side of the Hybrid AC/DC System

The power-angle stability of islanded ac microgrids has been extensively studied when wireless decentralized power-sharing schemes (e.g., droop controllers) are adopted [90]–[91]. However, passive loads have been considered in most of these studies without focusing on major dynamics loads in electrical systems such as the direct online IM. The total share of IM loads with respect to other electrical loads in distribution systems is around 60% whereas 80% of industrial loads are IMs [92]. Therefore, it is viable to investigate the effects of IMs on the stability of the low-inertia VSC-dominated microgrids.

The presence of IM loads in microgrids might induce; 1) source-load admittance mismatch between the IM load and microgrid converters, and 2) electromechanical rotor oscillations due to the lightly damped motor dynamics, particularly in large motors [93]-[94]. These special characteristics lead to two types of undesirable interaction dynamics in the islanded microgrids feeding direct-online IM loads; namely 1) medium-frequency interactions and 2) low-frequency interactions.

1) With respect to the *medium-frequency interactions*, in the small-signal sense, it can be shown that IM loads induce lightly damped dynamics that directly interact with the tightly-voltage-controlled VSCs in microgrids in the medium-frequency range (e.g., few tens of Hz to few hundreds of Hz). The lightly damped motor dynamics induce resonant peaks in the motor admittance and can directly violate the stable admittance ratio criterion between the load-side (IM) and equivalent source-side (VSC) [95].

   It is shown in this thesis that even with small IM loads; the medium-frequency interactions can be yielded. Such interactions destabilizes the islanded operation of microgrids due to the weak nature of the equivalent source admittance in isolated microgrids and the close regulation characteristics of VSCs, which are usually designed with high bandwidth characteristics for effective voltage regulation. On the contrary, when a microgrid system is connected to a strong utility-grid, the overall source impedance will be small and, therefore, the source-load impedance interactions will be minimal. These interactions occur directly between an IM and the voltage-controlled VSCs with minimum coupling from the power-sharing controller (e.g., droop control) due to the frequency-scale separation between the voltage control dynamics and the low-bandwidth power sharing loops. It should be noted that using the VSC control parameters to avoid possible interaction dynamics (e.g., voltage control bandwidth) yields very limited shaping capability and directly affects the closed-loop performance. Therefore, there is a strong need to develop a second-degree-of-freedom active controller that locally shapes the source admittance of the VSC at the instability-related frequency-range without affecting the overall system characteristics.

2) In large IM loads, the rotor-circuit time-constant is large and is comparable to the mechanical time-constant; therefore, the rotor-slip and flux-angle dynamics are highly coupled. This phenomenon leads to considerable low-frequency electromechanical oscillations (e.g., in the range of 0.2 Hz to few Hz). These oscillations directly affect the power-angle stability in the droop-controlled isolated microgrids with high power IM loads due to the inherent power-based feedback to regulate the microgrid frequency. However, such power-angle interactions are characterized by their low-frequency and can be separated from medium-frequency interactions. Power angle oscillations in droop-controlled microgrids can be mitigated by employing an active damping loop in the droop

controller [91]. Therefore, and regardless of the power-sharing strategy, mitigation of medium-frequency interactions is still essential.

The aforementioned difficulties, however, are not sufficiently addressed in the recent literature. Dynamic stability of the ac microgrids supplying a voltage-source rectifier (VSR) as an active load has been considered in [96] using a detailed small-signal modal analysis. An earlier work in [97] investigates the same problem using the Nyquist stability criterion. However, a generic and augmented model of the common active load has been considered. In [98], detailed small-signal impedance models of the VSC-based microgrid and the VSR load are introduced. Using the generalized Nyquist criterion, an active compensation method from the VSR (load) side has been proposed.

The effect of impedance mismatch between a single voltage-controlled VSC and the IM is presented in [95]. However, approximate diagonal impedance models are used to transform the multi-input-multi-output (MIMO) interaction dynamics problem into a single-input-single-output (SISO) problem, where the conventional Nyquist admittance ratio criterion can be used. In [99], the impact of composite load (IM and static loads) on the microgrid angle stability is investigated, using the bifurcation theory, and under a high penetration level of IMs.

Chapter 3

Analysis and Active Suppression of AC- and DC-Side Instabilities in the Grid-Connected Current-Source Converter-Based Photovoltaic Systems

CSCs can be a viable option to interface large PV systems to the utility grid. However, interaction dynamics in both the ac- and dc-sides might be yielded and affect the converter stability. 1) On the ac side, interactions of the grid impedance with the CL ac-side filter might cause uncertain resonant frequency modes that should be damped without affecting the converter efficiency. 2) On the dc-side, under uncertain characteristics of the PV source impedance (e.g., number of PV modules connected and/or uncertainty in source circuit parameters), the Nyquist stability criterion might be violated due to equivalent source/load impedance mismatch. In this chapter, the ac-side CL filter dynamics are damped by an improved active compensator in the control structure of the CSC. More importantly, the dc-side interactions dynamics are effectively stabilized by proposing active reshaping techniques for the dc-side impedance of the CSC so that the Nyquist stability criterion is maintained, and positive damping is added. Time-domain model is implemented under Matlab/Simulink environment to validate the analytical results.

3.1 The Grid-Connected Current-Source Converter-Based Photovoltaic System

3.1.1 The Current-Source Converter

The system under study is shown in Figure 3.1(a). The system parameters are all given in Appendices A3.1-A3.2. The CSC is a six-pulse converter employing IGBT switches in series with diodes. The dc-side of the CSC is interfaced by a choke (L_{dc}) with internal resistance (R_{dc}) to maintain the dc current (I_{dc}) regulated. An ac capacitor (C_s) is directly connected to the CSC terminals to filter out the switching harmonics in the ac current i_w. An inductor (L_s) with an internal resistance (R_s) is used to increase the attenuation capabilities of the ac-side filter so that the filtered ac current (i_s) is injected to the utility-grid. The CSC is connected to the utility-grid with a PCC voltage v_g whereas v_s is the terminal ac voltage of the CSC.

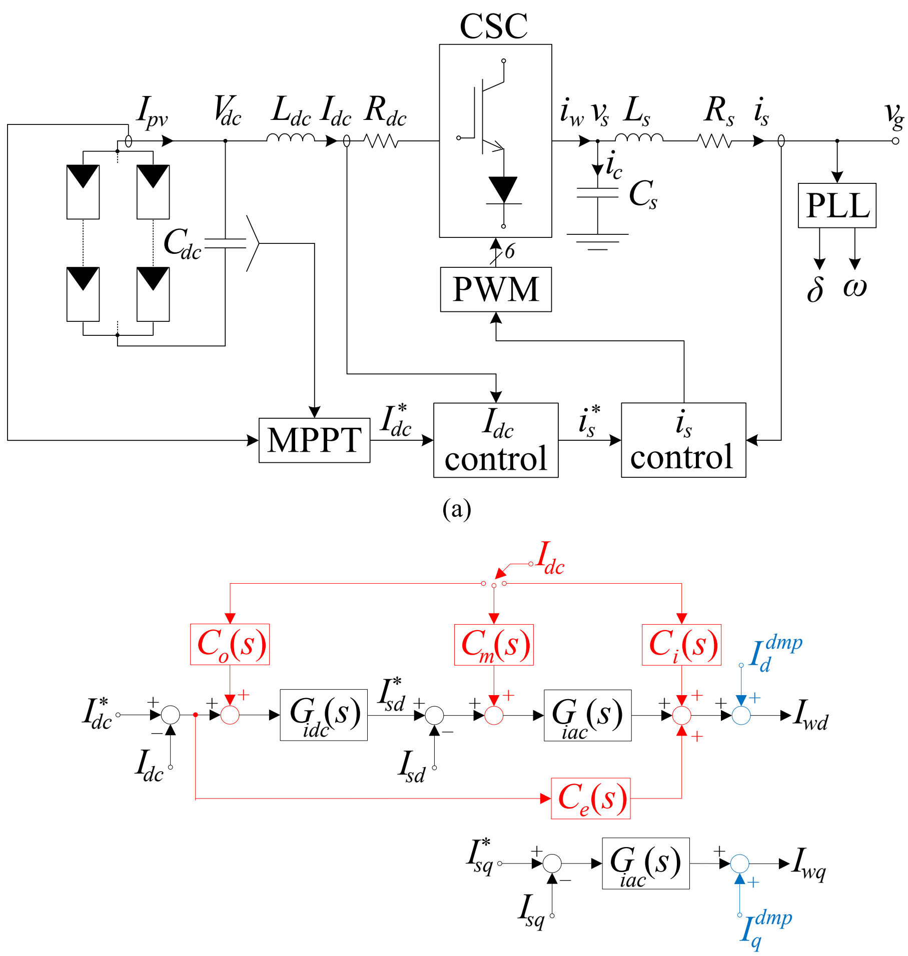

(b)

Figure 3.1 Grid-connected CSC-based PV system. (a) Power circuit. (b) Conventional vector control – $C_o(s)$, $C_m(s)$, $C_i(s)$, and $C_e(s)$ loops represent the proposed active compensators, one compensator at a time whereas I_d^{dmp} and I_q^{dmp} loops represent the proposed active damping for the CL filter resonance.

Based on Figure 3.1(a), the power circuit model of the grid connected CSC in the synchronous d-q reference frame that rotates by an angular frequency (ω) is given as following, where (m_d, m_q), (V_{sd}, V_{sq}), (V_{gd}, V_{gq}) and (I_{sd}, I_{sq}) are the d-q components of the generated modulation signals, v_s, v_g, and i_s, respectively; s is the Laplace operator.

$$V_{sd} - V_{gd} = I_{sd}(R_s + sL_s) - \omega L_s I_{sq} \tag{3.1}$$

$$V_{sq} - V_{gq} = I_{sq}(R_s + sL_s) + \omega L_s I_{sd} \tag{3.2}$$

$$m_d I_{dc} = sC_s V_{sd} + I_{sd} - \omega C_s V_{sq} \tag{3.3}$$

$$m_q I_{dc} = sC_s V_{sq} + I_{sq} + \omega C_s V_{sd} \tag{3.4}$$

$$V_{dc} = I_{dc}(R_{dc} + sL_{dc}) + \frac{3}{2}m_d V_{sd} + \frac{3}{2}m_q V_{sq} \tag{3.5}$$

3.1.2 The Photovoltaic Generator

The basic building block of the PV generator is the PV cell that typically produces $1.0 - 2.0$ W of electrical power [7], [19], [22]. Figure 3.2(a) shows the circuit representation of a PV module in which multiple PV cells are connected in series to increase the module terminal voltage (V_m) to $20 - 30$ V. The module current (I_m) is similar to the PV cell current. The solar irradiance (G) excites the electrons in the PV cells to generate the photovoltaic current (I_{ph}) which is dependent on the solar irradiance level, the PV module temperature (T), and the short-circuit current (I_{sc}) of the PV module,

$$I_{ph} = \frac{G}{G_r}[I_{sc} + \alpha_i(T - T_r)] \tag{3.6}$$

where G_r is the reference irradiance level in $\mathrm{W/m^2}$; T_r is the reference temperature in Kelvin, and α_i is the temperature coefficient in A/Kelvin.

As shown in (3.7), the relation between the diode current (I_D) and voltage (V_D) is governed by the non-linear Shockley diode model,

$$I_D = I_o\left[exp\left\{\frac{V_D}{n_s V_t}\right\} - 1\right] \tag{3.7a}$$

$$I_o = I_{or}\left(\frac{T}{T_r}\right)^3 exp\left\{\frac{TE_g}{V_t}\left(\frac{1}{T_r} - \frac{1}{T}\right)\right\} \tag{3.7b}$$

$$V_t = \frac{KAT}{q} \tag{3.7c}$$

where n_s is the number of PV cells in the module; V_t is the thermal voltage; I_o and I_{or} are the reverse saturation current at the operating and reference temperature, respectively; E_g is the band-gap energy of the PV cell; q is the unit charge; A is the ideality factor of the diode, and K is the Boltzmann's constant.

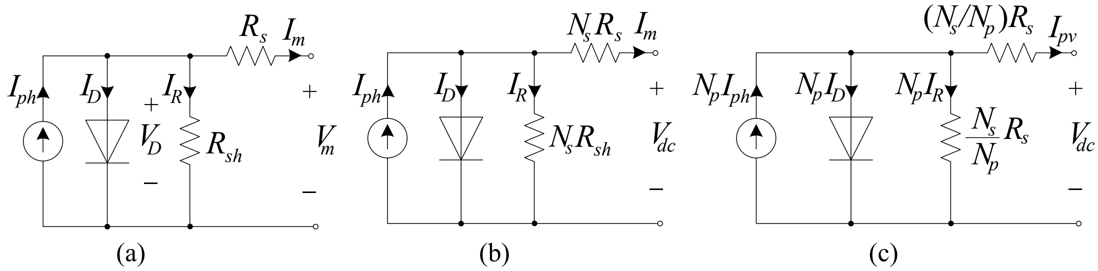

Figure 3.2 Equivalent circuit representation of the PV generator. (a) PV module. (b) PV string. (c) PV array.

As shown in Figure 3.2(a), a shunt resistance (R_{sh}) models the effect of the leakage current due to the fabrication process. It is assumed that R_{sh} is a fixed and an independent quantity. A parasitic series resistance (R_s) is also considered to model the power losses in the PV module.

$$I_R = V_D/R_{sh} \tag{3.8}$$

Several PV modules, similar to Figure 3.2(a), are stacked together and connected in series to form a PV string so that the terminal voltage builds up to V_{dc} whereas the dc current is still the same. The equivalent model of a PV string is shown in Figure 3.2(b) where N_s is the number of series connected modules in the PV string. The PV array, shown in Figure 3.2(c), is finally formed by the parallel connections of multiple PV strings, denoted by N_p, so that the required level of the dc current is satisfied as shown in (3.9). As V_D is not directly measured, it is represented in terms of V_{dc} and I_{dc} in (3.10). The PV system is assumed to operate at the MPP. Therefore, the delivered power to the utility-grid is assumed constant ($P_{pv} = V_{dc}I_{pv}$) [26].

$$I_{pv} = N_pI_{ph} - N_pI_D - N_pI_R \tag{3.9}$$

$$V_D = \frac{V_{dc}+I_{dc}\left(\frac{N_s}{N_p}\right)R_s}{N_s} \tag{3.10}$$

The dynamics of the dc-side of the PV generator is governed by (3.11).

$$I_{pv} = sC_{dc}V_{dc} + I_{dc} \tag{3.11}$$

3.1.3 The Conventional Vector Control of the Grid-Connected Current-Source Converter-Based Photovoltaic System

Figure 3.1(b) shows the control structure of the CSC in the synchronous rotating d-q reference frame. The measured dc current (I_{dc}) is compared to the reference value (I_{dc}^*) to process the error by a PI dc current controller ($G_{idc}(s)$), which determines the d-axis component of the reference value of the injected ac current (I_{sd}^*). The q-axis component (I_{sq}^*) is set to zero. The PI ac current controller ($G_{iac}(s)$) in both d-q channels regulates the corresponding measured values to follow their references. The control loops of the grid connected CSC are modeled as following.

$$I_{sd}^* = (I_{dc}^* - I_{dc})G_{idc}(s) \tag{3.12}$$

$$m_d I_{dc} = (I_{sd}^* - I_{sd})G_{iac}(s) + I_d^{dmp} \tag{3.13}$$

$$m_q I_{dc} = \left(I_{sq}^* - I_{sq}\right)G_{iac}(s) + I_q^{dmp} \tag{3.14}$$

3.2 AC-Side Instabilities of the Grid-Connected Current-Source Converter-Based Photovoltaic System

The proposed ac-side active compensator to mitigate the ac CL filter resonance is presented. Assume that there is a series resistor (R_d) with the capacitor (C_s) in Figure 3.1(a), (3.3) is modified to:

$$m_d I_{dc} = \frac{sC_s}{1+sC_sR_d}V_{sd} + I_{sd} - \omega C_s V_{sq} \tag{3.15}$$

Similarly, (3.4) is modified. The modified dynamics in (3.15) can be rewritten in the following form.

$$m_d I_{dc} + \frac{sC_sR_d}{1+sC_sR_d}sC_sV_{sd} = sC_sV_{sd} + I_{sd} - \omega C_s V_{sq} \tag{3.16}$$

From (3.16), the passive damping behavior can be actively emulated by adding the term

$(\frac{sC_sR_d}{1+sC_sR_d}sC_sV_{sd})$ to the originally generated m_dI_{dc} from the control loop in (3.13). Comparing (3.13) to (3.16) gives,

$$I_d^{dmp} = \underbrace{\frac{sC_sR_d}{1+sC_sR_d}}_{H(S)}\underbrace{sC_sV_{sd}}_{I_{c,d}}R_a \tag{3.17}$$

where $H(s)$ is a HPF with a cut-off frequency equals $1/C_sR_d$. In a similar way, I_q^{dmp} is obtained. The gain R_a is used to enhance the high frequency attenuation as will be shown.

The closed- and open-loop transfer functions of the ac current controller are obtained in (3.18)- (3.19), respectively. Figure 3.3(a) shows the frequency response of I_{sd}/I_{sd}^* in (3.18). The uncompensated response has a resonant peak at the resonance frequency of the CL filter. The response with the active damped method is shown when $R_d = 10$ and $R_a = 1$ and is typically as the passive damping technique with 10 Ω series resistance. The resonance peak is successfully mitigated; however, the attenuation level of the CL filter is reduced beyond the resonance frequency (420 Hz – 7th harmonics). The high frequency attenuation is enhanced by multiplying the compensation function ($H(s)$) by the additional gain (R_a). The frequency response of the open-loop transfer function with/without the proposed active damping is shown in Figure 3.3(b). The uncompensated system is unstable with a phase margin of $-6°$ whereas it is stable with a phase margin of 25° when the proposed active compensator is activated.

$$I_{sd} = \underbrace{\frac{G_{iac}(s)}{C_s s\big(1-R_aH(s)\big)(R_s+sL_s)+G_{iac}(s)+1}}_{\text{current control transfer function}} I_{sd}^* - \frac{sC_s(1-R_aH(s))}{C_s s\big(1-R_aH(s)\big)(R_s+sL_s)+G_{iac}(s)+1}V_{gd} \tag{3.18}$$

$$G_{ol}^{ac}(s) = \frac{G_{ac}(s)}{C_s s(1-R_aH(s))(R_s+sL_s)+1} \tag{3.19}$$

3.3 DC-Side Instabilities of the Grid-Connected Current-Source Converter-Based Photovoltaic System

3.3.1 Small-Signal Impedance-Based Modeling of the Grid-Connected Current-Source Converter

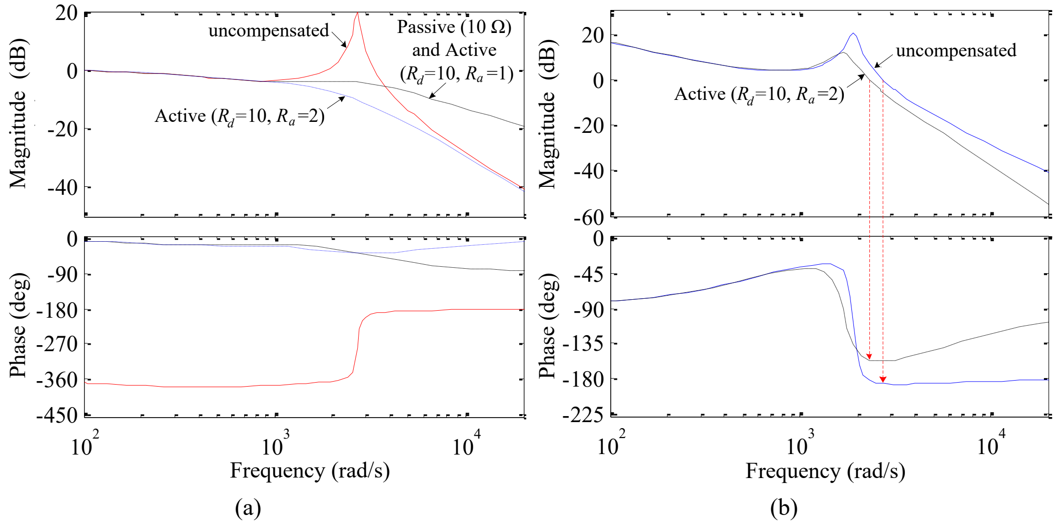

Figure 3.3 Frequency response of the ac LC filter of CSC. (a) Closed loop (I_{sd}/I_{sd}^{*}). (b) Open loop.

Applying the small-signal linearization on the system model and conducting some mathematical manipulations, the small-signal dc-side impedance of the grid-connected CSC that relates ΔV_{dc} to ΔI_{dc} is obtained as follows.

$$\Delta Z_{csc}(s) = \frac{\Delta V_{dc}}{\Delta I_{dc}} = K_{dc}(s) + \left(K_d(s) + K_q(s)K_{dq}(s)\right)K_{ddc}(s) \qquad (3.20)$$

The parameters of (3.20) are defined in Appendix A3.3.

3.3.2 Small-Signal Impedance-Based Modeling of the Photovoltaic Generator

The small-signal impedance model of the PV generator is obtained under the assumption of constant weather conditions, i.e., the operating temperature equals the reference temperature ($T = T_r$) and the irradiation level (G) is constant. Applying small-signal perturbations on the PV model in (3.6), ΔI_{ph} is obtained in terms of ΔV_{dc} and ΔI_{pv}. The PV model in (3.6) is then multiplied by V_{dc} and a small-signal linearization is reapplied with $\Delta P_{pv} = 0$ (MPP) so that the small-signal source impedance of the PV system ($\Delta Z_{pv}(s) = \Delta V_{dc}/\Delta I_{pv}$) is finally obtained. The influence of both R_s and R_{sh} on the PV generator model is neglected in this chapter.

$$\Delta Z_{pv} = -\frac{\mathring{V}_{dc}/N_p}{\left(\mathring{I}_{ph}+\mathring{I}_{or}\right)-\mathring{I}_{or}exp\left(\frac{\mathring{V}_D}{\mathring{V}_t n_s}\right)} \tag{3.21}$$

The dc-link capacitor dynamics in (3.8) are used to obtain the overall source impedance of the PV system ($\Delta Z_{pv,tot}(s) = \Delta V_{dc}/\Delta I_{dc}$) as seen from the dc terminals of the CSC, which is as follows.

$$\Delta Z_{pv,tot}(s) = \frac{\Delta Z_{pv}}{1-sC_{dc}\Delta Z_{pv}} \tag{3.22}$$

3.3.3 Input-Output DC-Side Impedance Mismatch

An interconnected system that constitutes an equivalent source ($\Delta Z_{source}(s)$) and load ($\Delta Z_{load}(s)$) impedances, around the point of interconnection, i.e., the dc-link between the PV and the grid-connected converter, is stable if the ratio $\Delta Z_{source}(s)/\Delta Z_{load}(s)$ does not encircle the $(-1, 0)$ point on the Nyquist contours. Note that the ratio $\Delta Z_{source}(s)/\Delta Z_{load}(s)$ is only valid with voltage-sourced converters whereas it should be reversed with current-sourced converter, i.e., $\Delta Z_{load}(s)/\Delta Z_{source}(s)$ [45]. By utilizing this criterion, and based on the obtained small-signal impedance models of the CSC and the PV system in (3.21) and (3.22), the system stability is investigated. An unstable case is induced by reducing the integral gain of the CSC and n_p and the system response is shown in Figure 3.4. There are two intersections in the magnitudes of the two impedances at points A and B where the magnitude of the Nyquist ratio is unity and hence it is required to achieve a stable phase margin [45]. At point A, the phase difference ($\angle \Delta Z_{pv,tot} - \angle \Delta Z_{CSC}$) is $30°$ which satisfies the stability conditions. On the other side, the response at point B is unstable with a phase margin of $-41°$.

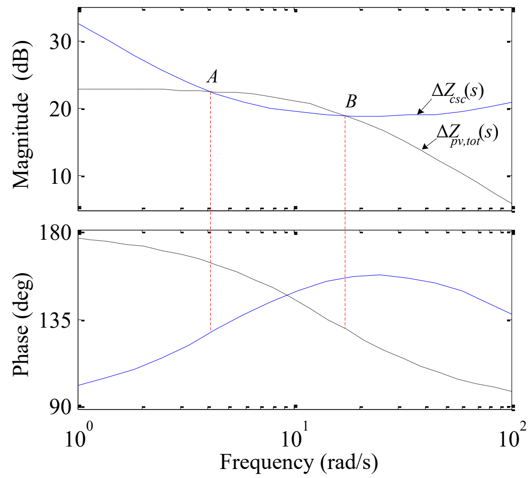

Figure 3.4 Input-output dc impedance interactions of the grid-connected CSC-based PV system – phase margin of A and B equals $30°$ and $-41°$, respectively.

3.3.4 Mitigation of the DC-Side Instabilities of the Grid-Connected Current-Source Converter-Based Photovoltaic System

To enhance the dynamic performance of the system in Figure 3.4, either the dc-side impedance of the PV system or the CSC should be reshaped to avoid the magnitude intersection or to achieve a sufficient phase margin at the frequency of intersection. One of the basic solutions in power electronic converter applications is to use passive damping techniques [100]. However, these methods are not preferred due to the associated power losses. In this chapter, active stabilizers from the CSC side are proposed to maintain the Nyquist stability criterion and enhance the dynamic performance of the CSC under wide variations of the PV parameters.

3.3.4.1 DC-Current-Based Compensators

As shown in Figure 3.1(b), the dc-choke current is applied through a compensation function ($C_o(s)$, $C_m(s)$, or $C_i(s)$) and is re-injected to three points in the d-axis control structure of the CSC. The compensation function can be in the form of a band-pass filter (BPF) or HPF as shown in (3.23) where k_n, ξ_n and ω_n are the compensator gain, damping ratio and operating frequency of the compensator, respectively. The subscript n represents the point of injection; outer (o), intermediate (m) and inner point (i).

$$C_{n,BP}(s) = k_n \frac{2\xi_n \omega_n s}{s^2+2\xi_n \omega_n s+\omega_n^2},$$

$$C_{n,HP}(s) = k_n \frac{s}{s+\omega_n} \tag{3.23}$$

The proposed compensation function allows the impedance reshaping at critical frequencies regions where the impedance intersections occur while preserving the characteristics of the CSC impedance elsewhere. The small-signal compensated dc-side impedance of the CSC (ΔZ_{csc}^{n}) is similar to that shown in (3.20) but with $K_{ddc}(s)$ is replaced by $K_{ddc}^{n}(s)$ as shown in Appendix A3.4. Note that one compensator is only activated at a time with the BPF or the HPF characteristics.

As a design example, the unstable case in Figure 3.4 is reconsidered with the BPF-based outer loop compensator ($C_{o,BP}(s)$). Figure 3.5(a) shows the modified frequency response with the proposed compensator.

The selected operating frequency (ω_o) of the BPF is $50\,\mathrm{rad/s}$. The damping ratio (ξ_o) is unity whereas the compensator gain (k_o) is varied from 10 to 30. The system stability is significantly improved by avoiding the magnitude intersections between the PV and CSC dc-side impedances. The corresponding Nyquist plots are shown in Figure 3.5(b). The stability margin is improved as compared to the uncompensated response. Similar damped response can be yielded by utilizing other injection points or a HPF-based compensator function.

3.3.4.2 DC-Error-Based Compensator

Figure 3.1(b) shows the proposed dc-error-based compensator ($C_e(s)$). The compensator function is selected as follows.

$$C_e(s) = -\frac{1}{sC_{dc}} Y_c \tag{3.24}$$

The dc current error ($I_{dc}^{*} - I_{dc}$) is used as the input to this compensator in order to extract any yielded oscillations at the dc-side. The signal is then applied to an integrator and is divided by the value of the dc capacitor (C_{dc}) to obtain the equivalent voltage drop. This voltage is applied to a gain (Y_c) to obtain the equivalent signal that is superimposed on the dc current and causing oscillations. The compensation signal is finally subtracted from the generated control signal in the d-axis ($m_d I_{dc}$). The modified small-signal dc-side impedance of the CSC with this compensator ($\Delta Z_{csc}^{e}(s)$) is similar to the uncompensated one in (3.20) but with $K_{ddc}(s)$ is replaced by $K_{ddc}^{e}(s)$ as shown in Appendix A3.5. The frequency response of the compensated system is similar to that yielded in Figure 3.5.

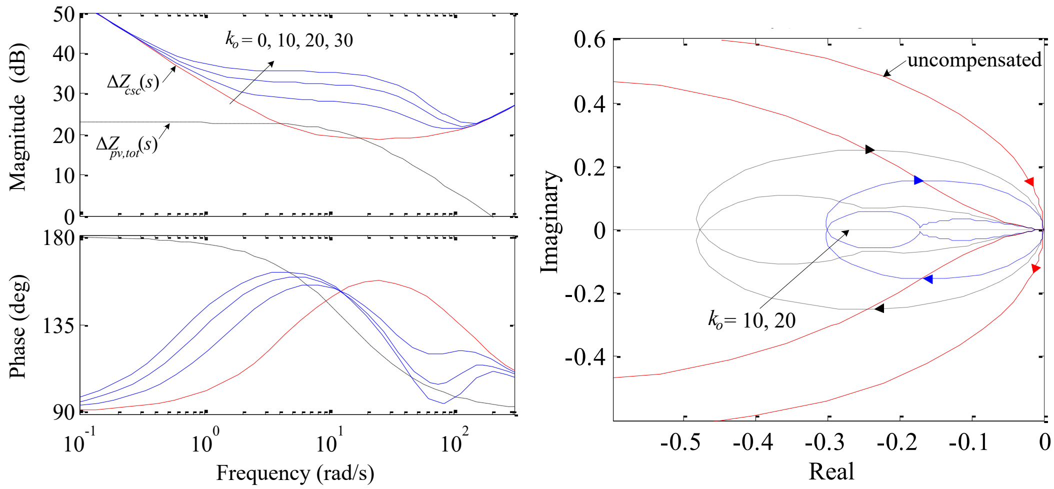

Figure 3.5 Active stabilization of the dc-side instabilities using the proposed dc current-based compensator – outer loop, BPF.

3.3.4.3 Sensitivity Analysis

The proposed active compensators might affect the performance of the injected ac current. This can be evaluated by investigating the sensitivity function ($\Delta I_{sd}/\Delta I_{dc}$) to study the influence of the input ΔI_{dc} on the output ΔI_{sd} in the presence of the proposed compensators. The sensitivity function of the uncompensated system is $K_{ddc}(s)$ in (3.20). For the actively compensated systems, they are all given in Appendices A3.4-A3.5 ($K_{ddc}^{n}(s)$, $K_{ddc}^{e}(s)$).

Figure 3.6 shows the sensitivity functions with the proposed compensators as compared to the uncompensated case. The actively compensated functions consider the HPF- and the BPF-based compensators to achieve a similar damping capability. As shown, the BPF-based sensitivity functions have better response as compared to the HPF-based ones. This is due to the localized effect of the BPF around its operating frequency. On the contrary, the HPF compensators operate from its cut-off frequency and beyond, which deforms the compensated dc-side impedance of the CSC and hence affect the sensitivity functions of the injected ac current on a wider frequency band.

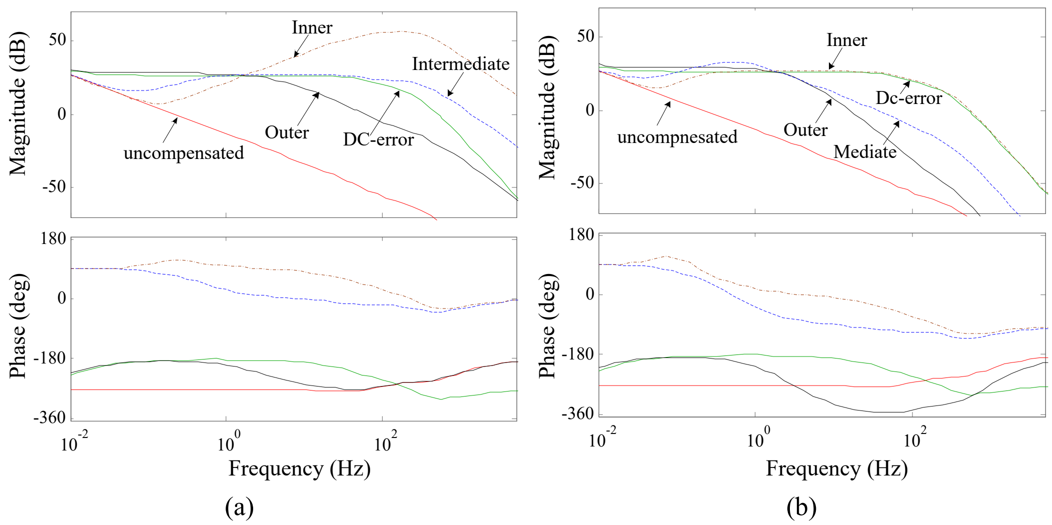

Figure 3.6 Sensitivity functions ($\Delta I_{sd}/\Delta I_{dc}$) of the CSC-based PV system. (a) HPF. (b) BPF.

3.4 Evaluation Results – AC-Side Instabilities

A large-signal time-domain simulation model of the grid-connected CSC-based PV system similar to that shown in Figure 3.1 is built under Matlab/Simulink® environment to investigate the influence of the proposed compensators. All model entities are built using SimPowerSystem® toolbox. The CSC is simulated using average-model-based blocks. The simulation type is discrete with a sample time of 50 μs. The system parameters are given in Appendices A3.1-A3.2.

Figure 3.7 shows the one phase response of the injected ac current to the utility-grid under the uncompensated, passively, and actively compensated ac resonance of the CL filter. As shown, the uncompensated system is superimposed with high-frequency harmonics that decay in 0.2 s. The same system is tested after adding a series resistor (10Ω) in series with the capacitor of the ac CL filter, and the system response is shown in Figure 3.7(b). The proposed active compensation of the CL filter resonance [in (3.17)] is implemented, and the ac current response is shown in Figure 3.7(c) with two values of R_a. The system with $R_a = 5$ gives a well-damped performance similar to that yielded with the passive damping but with no active power losses.

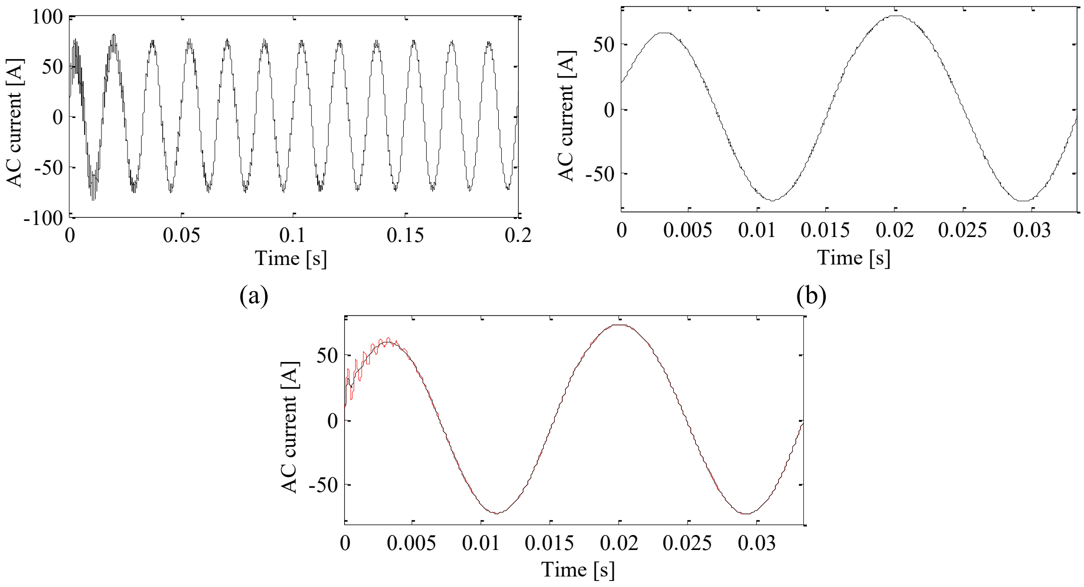

Figure 3.7 Influence of the CL filter resonance on the injected ac current in the grid-connected CSC. (a) Uncompensated. (b) Passively compensated. (c) Actively compensated with highly damped ($R_a = 5\ \Omega$) and less damped performance ($R_a = 1\Omega$).

3.5 Evaluation Results – DC-Side Instabilities

The first evaluation test is conducted when the insolation level is assumed constant. The uncompensated response is shown in Figure 3.8(a). As shown, the dc current has significant oscillations up to 0.6 s. These oscillations are reflected to the injected ac current. On the same figure, the improved performance due to the increased number of parallel modules by 20% is shown. In spite of the 0.27 p.u. higher overshoot of the dc current at startup, the oscillations are damped after a shorter time at $t = 0.35$ s.

3.5.1 Passively Compensated Response

The insolation level of the PV system is assumed to have step variations as a severe testing condition. The step variation of the solar irradiance level has been widely adopted in the literature to evaluate the stability of the PV systems [7]-[9], [22], and [25]. Accordingly, the MPP algorithm will change the dc current reference to cope with the modified energy balance. As shown in Figure 3.8(a) with $R_{dc} = 1$ p.u, the dc current follows the reference command but with considerable oscillations at the step instants. The uncompensated dc current peaks are 1.22,

-0.84 and 0.45 p.u. at $t = 0$, 1.0 and 1.5 s, respectively. The oscillations yielded in the dc current response are reflected to the injected ac current as shown in Figure 3.8(b).

The influence of the passive damping is shown in the same figure by increasing R_{dc} to 3 p.u. The dc current oscillations are relatively damped as compared to the uncompensated case. The passively-compensated dc current peaks are 1.03, -0.67 and 0.34 p.u. at $t = 0$, 1.0 and 1.5 s, respectively. The effect of adding a passive element is clearly shown in Figure 3.8(b). At the period $t = 0.5$ to 1.0 s, the steady-state value of the injected ac current is reduced due to the dissipated power in the added dc-side series resistor.

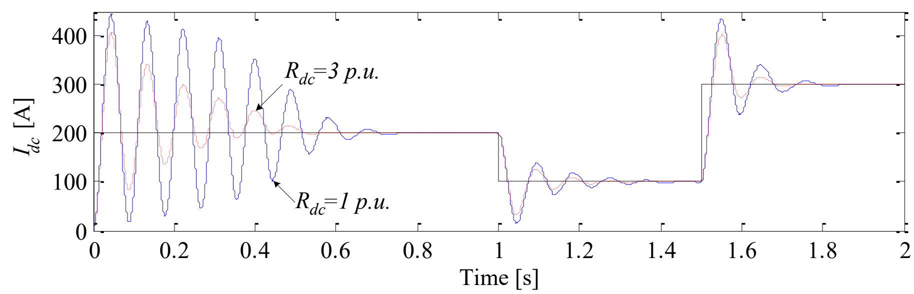

(a)

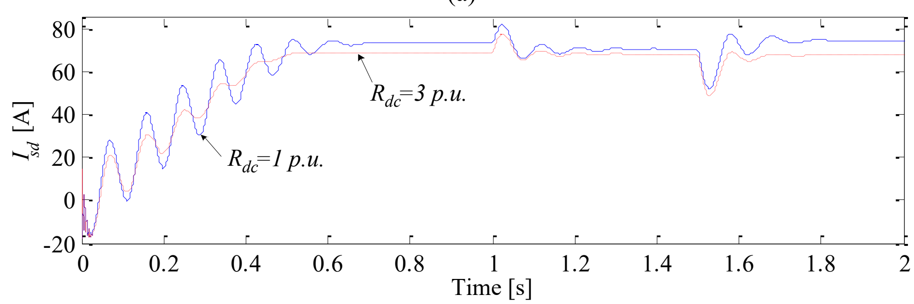

(b)

Figure 3.8 Uncompensated ($R_{dc} = 1\, p.u.$) and passively damped ($R_{dc} = 3\, p.u.$) response in the grid-connected CSC-based PV system. (a) DC current. (b) d-axis component of injected ac current.

3.5.2 Actively Compensated Response

Figure 3.9 shows the actively-compensated response using the proposed dc-error-based compensator. As compared to the uncompensated response in Figure 3.8, the dc-error-based compensation provides a significant damping to the system. The dc current peaks are 1.22, 0.84 and 1.1 $\mathrm{p.u.}$ at $t = 0$, 1.0 and 1.5 s, respectively. The high damped response is conveyed throughout the system as shown in Figure 3.9(b). However, there is a side effect of the compensated response on the injected ac currents at the disturbance instants. As shown in Figure 3.9(b) the ac current peaks are 0.47 and $-0.99\,\mathrm{p.u.}$ at $t = 1.0$ and 1.5 s, respectively. As compared to the uncompensated response in Figure 3.8(b), the current peaks are 0.11 and $-0.26\,\mathrm{p.u.}$ at $t = 1.0$ and 1.5 s, respectively. This side effect is attributed to the sensitivity analysis in Figure 3.6. The coupling between dc and ac currents increases due to the proposed dc-error-based compensator.

Figure 3.10 shows the actively compensated response using the outer loop BPF-based compensator. In Figure 3.10(a), the startup peak of the dc-choke current is $0.2\,\mathrm{p.u.}$ The dc current is highly damped with no overshoots at $t = 1.0$ and 1.5 s. Based on the sensitivity analysis in Figure 3.6, the influence of outer loop BP-based compensator on the injected ac current is less than that yielded with the dc-error-based compensator. This is clear from the response of the ac current in Figure 3.10(b) as compared to Figure 3.9(b). The influence of the intermediate and inner loop BP-based compensators on the system stability is shown in Figure 3.11.

The dc current response following different variations in the solar irradiance level is shown in Figure 3.12. In spite of the slower rate of change of the solar irradiance level, the uncompensated dc current response reflects a lightly damped performance. The outer loop compensator is implemented in the control structure and, clearly, the resultant performance is highly damped. The oscillations of the uncompensated system in Figure 3.12 imply power losses in the PV generator. On the contrary, the proposed compensator contributes to the damping of the PV system by following the MPP set points in a well-damped performance, which in turns enhances the dynamic efficiency of the PV generator.

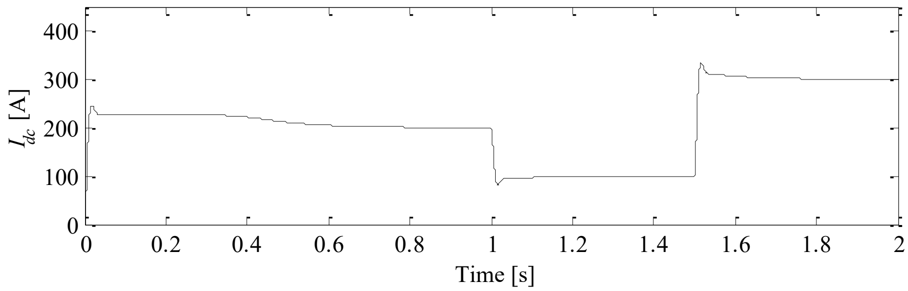

(a)

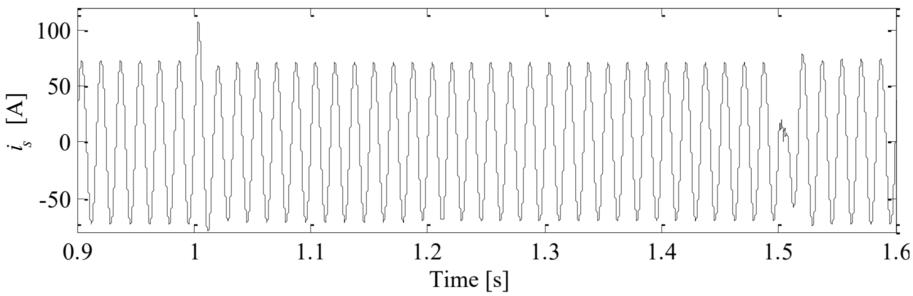

(b)

Figure 3.9 DC-error-based active compensated response of the CSC-PV system. (a) DC current. (b) Injected ac current.

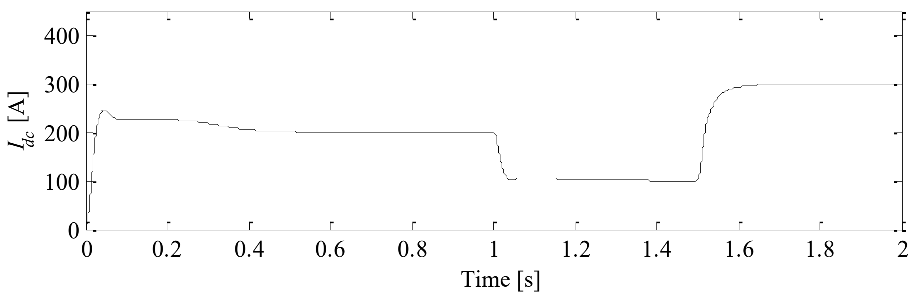

(a)

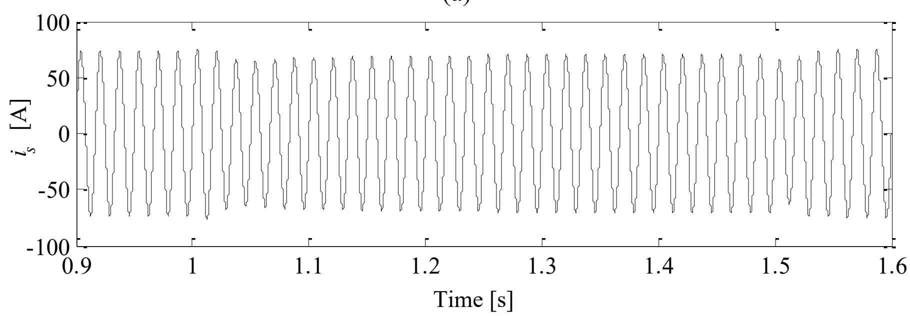

(b)

Figure 3.10 Outer loop-based active compensated response of the CSC-PV system. (a) DC current. (b) Injected ac current.

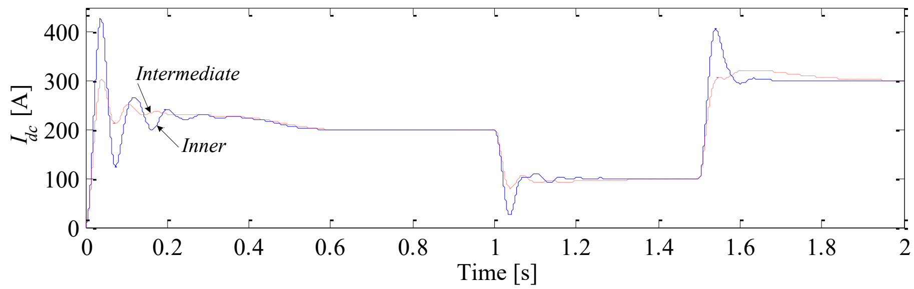

Figure 3.11 Intermediate and inner loop-based active compensated response of the CSC-based PV system.

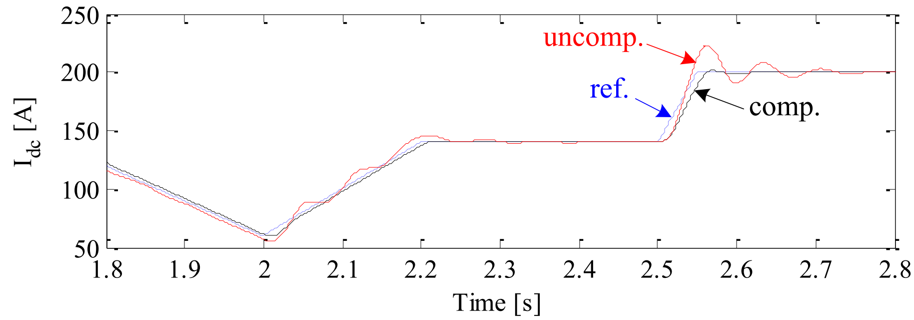

Figure 3.12 System response following slow variations in the incident solar irradiance level of the CSC-based PV system.

3.6 Conclusions

The ac- and dc-side instabilities in the grid-connected CSC-based PV systems has been investigated in this chapter. It is found that instabilities of the CSC interface can be yielded due to the following. 1) Interactions with the ac-side due to the induced ac CL filter resonance. Therefore, an active damping technique that emulates a series resistance with the ac capacitor is proposed to mitigate the resonant peak of the CL filter. 2) Interactions with the dc-side, i.e., the PV generator, due to the input/output small-signal impedances mismatch that violates the Nyquist stability criterion. Linear, simple and efficient active compensation techniques have been proposed to reshape the input impedance of the CSC so that Nyquist criterion is maintained. The proposed compensators enable robust integration of the CSC into utility-grid under a wide range of ac- and dc-side uncertainties. Time-domain simulation results successfully validate the analytical results.

Chapter 4

The Power Synchronization Control for the Grid-Connected Current-Source Converter-Based Photovoltaic System

This chapter presents the PSC scheme for the single-stage grid-connected CSC-based PV system. A detailed small-signal model for the complete CSC-based PV system with the PSC strategy is developed to investigate the system stability, characterize the converter interactions with the utility-grid, and design the controller parameters. The PSC of the CSC-based PV system reflects a stable performance under different operating conditions and following sudden variations in the insolation level. Due to the inherent synchronizing feature of the PSC, the PLL is eliminated and hence, the integration to very weak-grid systems is inherently achieved. Although there is no direct control on the injected ac current to the utility-grid, the physical structure of the CSC offers a self-current-limiting protection through the modulation of the regulated dc-choke current. Detailed nonlinear time-domain simulations results validate the theoretical analysis and show the effectiveness of the PSC for the CSC-based PV systems.

4.1 System Under Study

Figure 4.1 shows the system structure of the grid-connected CSC-based PV generator. The complete system parameters are given in Appendix A4.1. Note that high power converters can be easily realized especially with the development of the high-power-density IGBT modules [31], which are rated at 4.5 kV and 1.2 kA. The recent advances have motivated the researchers to adopt high-power IGBT-based CSCs in HVDC applications [13]-[14]. For instance, an augmented six-switch CSC-based model representing a typical CSC rated at 500 MW and operating at 2 kHz switching frequency is considered in [13]. A similar converter topology is adopted in [14] with a CSC system rated at 100 MW and 1 kHz switching frequency.

The CSC is a two-level converter consisting of six cells; each comprises an IGBT in series with a diode to increase the reverse voltage capability. The converter structure is similar to that introduced in Chapter 3 [Figure 3.1 (a)] and hence no more details are elaborated here.

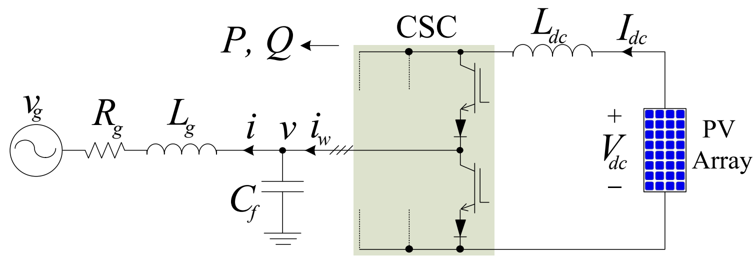

Figure 4.1 A grid-connected CSC-based PV system.

The ac-side of the CSC is modeled in (4.1)-(4.2) in the rotating reference frame that rotates by the angular speed ω. Neglecting the power losses through the CSC, the dc-side dynamics of the PV system is modeled as shown in (4.3).

$$\bar{\imath}_w = \left(sC_f + j\omega C_f\right)\bar{v} + \bar{\imath} \tag{4.1}$$

$$\bar{v} - \bar{v}_g = \left(R_g + sL_g + j\omega L_g\right)\bar{\imath} \tag{4.2}$$

$$\frac{1}{2}L_{dc}\frac{dI_{dc}^2}{dt} = V_{dc}I_{dc} - P \tag{4.3}$$

where the complex vector $\bar{u} = \mathcal{U}_d + j\mathcal{U}_q$ such that $\mathcal{U}_d$ and $\mathcal{U}_q$ are the direct (d-) and quadrature (q-) component in the rotating reference frame; s is the Laplace operator, and j is the imaginary unit number.

The modeling of the PV generator is presented in details in Chapter 3. In this chapter, a Mitsubishi PV array of a model “PV-UD190MF5” has been considered [101]. All PV parameters are given in Appendix A4.1.

4.2 Power Synchronization Control Structure

The structure of the power synchronization control is shown in Figure 4.2. The control is developed in two levels; an active power controller and a PCC voltage controller [44].

4.2.1 Active Power Control

The power synchronization loop is shown in Figure 4.2(a), where the active power (P) is regulated to follow the reference value (P^*) and synchronize the CSC with the utility-grid using the orientation angle (δ). Note that the nominal grid frequency ($\omega_\circ t$) is added to the generated δ to provide the final synchronization angle (ωt). The PLL is not needed in the control structure of the PSC. As shown in (4.4a), the active power control is realized by an integral gain (k_δ). The superscript "c" refers to the converter reference frame.

$$\delta = (P^* - P)\frac{k_\delta}{s} \tag{4.4a}$$

$$P = \frac{3}{2}\left(V_d^c I_d^c + V_q^c I_q^c\right). \tag{4.4b}$$

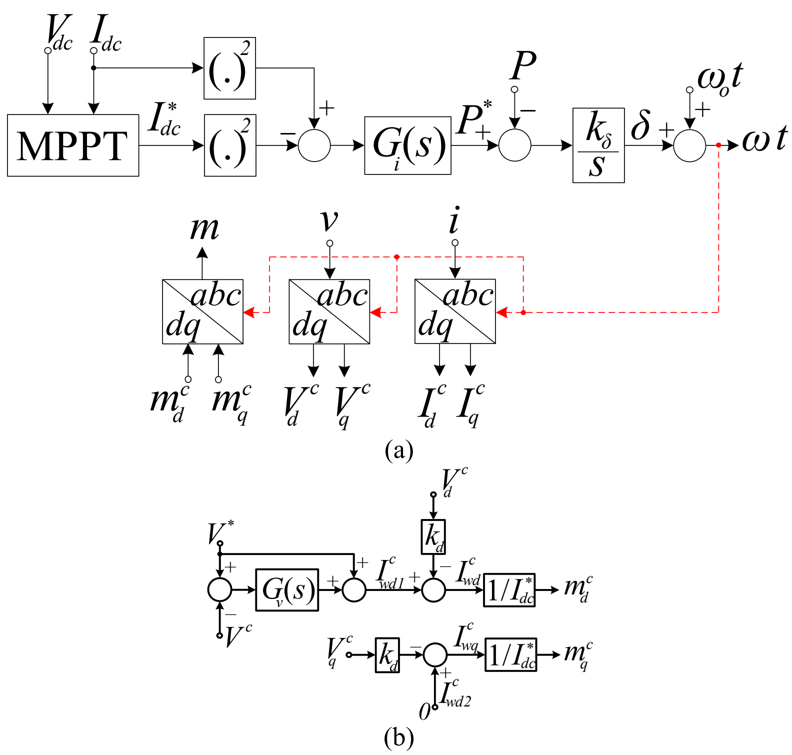

Figure 4.2 Power synchronization control of the grid-connected CSC-based PV system. (a) Active power control and synchronization. (b) PCC voltage control.

Referring to (4.3), the rate of change of the energy in the dc-choke is governed by the balance between the generated PV power ($V_{dc}I_{dc}$) and the injected active power to the utility-gird (P), assuming a lossless CSC. The input-output power balance is maintained by regulating the squared value of the dc-choke current (I_{dc}^2). Therefore, and as shown in Figure 4.2(a), the reference value of the injected active power (P^*) is determined by the outer dc-choke current control. The squared value of the dc-choke current (I_{dc}^2) is regulated by a PI current controller with a transfer function $G_i(s) = k_{ip} + k_{ii}/s$ in order to follow the reference value (I_{dc}^{*2}). The MPP algorithm generates I_{dc}^* so that the solar power harvesting is maximized at different weather conditions [102].

$$P^* = -(I_{dc}^{*2} - I_{dc}^2)G_i(s) \tag{4.5}$$

4.2.2 AC Voltage Regulation

As shown in Figure 4.2(b), the magnitude of the PCC voltage (V) is regulated to follow the reference value (V^*) using a PI voltage controller, $G_v(s) = k_{vp} + k_{vi}/s$. The modulation signals in the d- and q- axis, i.e., m_d and m_q, are generated and then transformed to the three-phase reference frame using the orientation angle (δ). The switching pattern is generated and applied to I_{dc} to produce the modulated three-phase output current (i_w). Eventually, a sinusoidal output current (i) and voltage (v) are obtained. Note that the regulation of the PCC voltage in the CSC is indirectly achieved by the control of i_w and the back-and-forth reactive power exchange with the utility-grid through the capacitive filter (C_f). Following Figure 4.2(b), the PCC voltage control loops are modeled in (4.6),

$$\vec{\iota}_w^c = (V^* - V^c)G_v(s) + V^* - k_d\vec{v}^c \tag{4.6}$$

where $V^c = \sqrt{V_d^{c2} + V_q^{c2}}$.

An outer reactive power control loop can be implemented to modify the value of V^* so that the measured reactive power (Q) follows the reference value (Q^*) using a PI controller. However, the regulation of the PCC voltage is only considered in this chapter. More details on the reactive power support can be found in [44] and [57].

As shown in Figure 4.2(b), an active damping technique is implemented to damp the resonance peak resulted from the combination of C_f and the equivalent grid inductance (L_g) [103]. The capacitor-voltage signals (V_d^c and V_q^c) are multiplied by a constant gain (k_d) and subtracted from the current references to generate the damped currents (I_{wd}^c and I_{wq}^c). The implemented gains (k_d) represent a damping resistor in series with C_f. Using (4.1)-(4.2), the following transfer function is obtained.

$$\vec{\iota} = \frac{1/(L_g C_f)}{s^2 + (k_d/C_f)s + (1/(L_g C_f))}\vec{\iota}_{w1} \tag{4.7}$$

The resistance R_g is neglected in (4.7) for simplicity whereas each s is replaced by $s - j\omega$ to obtain the space-vector representation of the currents $\vec{\iota}$ and $\vec{\iota}_{w1}$. As shown, (4.7) is a standard second-order system with a natural frequency $1/\sqrt{L_g C_f}$ and a damping ratio $0.5 k_d \sqrt{L_g / C_f}$. Clearly, the implementation of the active damping loop (k_d) increases the system damping.

4.2.3 Frame Transformation

Similar to the operation of the PLL, the generated δ from the PSC is used in the transformation from the three-phase grid frame to the converter $d - q$ reference frame, and vice versa [39]. Referring to Figure 4.2(a), the measured quantities (i.e, i and v) should be transformed to the converter reference frame, whereas the controller output signals (i.e., $\bar{\iota}_w^c$ or $\bar{m}^c$) should be retransformed to the grid reference frame in order to accurately model the influence of the synchronization loop on the system dynamics. These transformations are as follows:

$$
\begin{aligned}
\bar{v}^c &= e^{-j\delta}\bar{v}, \\
\bar{\iota}^c &= e^{-j\delta}\bar{\iota}, \\
\bar{\iota}_w &= e^{j\delta}\bar{\iota}_w^c.
\end{aligned}
\tag{4.8}
$$

4.3 Small-Signal Modeling of the Current-Source Converter-Based Photovoltaic System

In this section, the small-signal linearization modeling of the CSC-based PV system in Figures 4.1 and 4.2 is presented. The matrices of the following models are defined in Appendix A4.2. In the following, A, B, C, are the state, input, and output matrices and are multiplied by the corresponding vectors, and Δ represents a small perturbation of the variable.

4.3.1 Closed-Loop Transfer Functions of the Power Synchronization Controllers

Applying the small-signal linearization on the power circuit model in (4.1) and (4.3), the controllers in (4.4) and (4.6), and using the frame transformations in (4.8), the following state-space model is yielded,

$$[\Delta \dot{X_{in}}] = [A_{in}][\Delta X_{in}] + \left[B_{inp}\right][\Delta P^{*}] + [B_{inv}][\Delta V^{*}] + [B_{indc}][\Delta V_{dc}] + [B_{ini}][\Delta I_d \quad \Delta I_q]^T \tag{4.9}$$

where $\Delta X_{in} = [\Delta V_d \quad \Delta V_q \quad \Delta I_{dc}^2 \quad \Delta\varphi_v \quad \Delta\delta]^T$ and $\Delta\varphi_v$ represents the state of the integral gain (k_{vi}).

The small-signal model of the utility-grid in (4.2) is used to eliminate the input vector $[\Delta I_d \quad \Delta I_q]^T$ in (4.9) such that the following state-space model is yielded, where $\Delta X_{cl} = [\Delta X_{in} \quad \Delta I_d \quad \Delta I_d]^T$.

$$\begin{gathered}[\Delta \dot{X_{cl}}] = [A_{cl}][\Delta X_{cl}] + \left[B_{clp}\right][\Delta P^{*}] + [B_{clv}][\Delta V^{*}], \\ \Delta P = \left[C_{clp}\right][\Delta X_{cl}], \Delta V = [C_{clv}][\Delta X_{cl}].\end{gathered} \tag{4.10}$$

The final closed-loop transfer functions of the power and voltage controllers are then obtained as shown in (4.11).

$$\Delta P = \left[C_{clp}(sI - A_{cl})^{-1} B_{clp}\right]\Delta P^{*} \tag{4.11a}$$

$$\Delta V = [C_{clv}(sI - A_{cl})^{-1} B_{clv}]\Delta V^{*} \tag{4.11b}$$

Using the dc-side model in (4.3) and (4.5), the dynamics of the dc current controller can be described by the following closed-loop transfer function.

$$\Delta I_{dc}^2 = \frac{(2k_{ip}/L_{dc})s + (k_{ii}/L_{dc})}{s^2 + (2k_{ip}/L_{dc})s + (2k_{ii}/L_{dc})}\Delta I_{dc}^{*2} \tag{4.12}$$

4.3.2 Small-Signal Impedance Modeling

The models of the dc current controller in (4.5) and the PV generator are used to substitute the inputs ΔP^{*} and ΔV_{dc} in (4.9). The following state-space model is obtained, where $\Delta X_z = [\Delta X_{in} \quad \Delta\varphi_i]^T$, and $\Delta\varphi_i$ represents the state of the integral gain of the current controller (k_{ii}),

$$[\Delta \dot{X_z}] = [A_z][\Delta X_z] + [B_z][\Delta I_d \quad \Delta I_q]^T,$$
$$[\Delta V_d \quad \Delta V_q]^T = [C_z][\Delta X_z]. \tag{4.13}$$

From (4.13), the 2×2 output impedance matrix of the CSC- PV ($\Delta Z_{csc}(s)$), as seen from the PCC, is as follows where I is the identity matrix.

$$[\Delta V_d \quad \Delta V_q]^T = [C_z(sI - A_z)^{-1}B_{ini}][\Delta I_d \quad \Delta I_q]^T \tag{4.14}$$

4.3.3 Small-Signal State-Space Model of the Entire System

The dc current controller model in (4.5) is used in (4.10) to substitute the input ΔP^*. As the reactive power control is not considered in this paper, ΔV^* is set to zero. The final state-space model that represents the entire dynamics of the grid-connected CSC-based PV system is given in (4.15) where $\Delta X_{tot} = [\Delta X_{cl} \quad \Delta \varphi_i]^T$.

$$[\Delta \dot{X_{tot}}] = [A_{tot}][\Delta X_{tot}] \tag{4.15}$$

4.4 Controllers Design

This section presents the analysis of the CSC-based PV system using the developed models in (4.9)-(4.15). In this section, the inner active compensation loop is considered with $k_d = 1.0$.

4.4.1 The Power Synchronization Control Loop

The frequency response of the closed-loop transfer function of the active power controller in (4.11a) is shown in Figure 4.3(a). When $k_\delta = 1.0$, 2.0, and 3.0 p.u., the corresponding closed-loop bandwidth is 174, 280, and 347 rad/s, respectively. Similar to the PLL, the bandwidth of the active power controller of the PSC is typically less than the half of the power frequency [57]. Therefore, k_δ is set to 1.0 p.u.

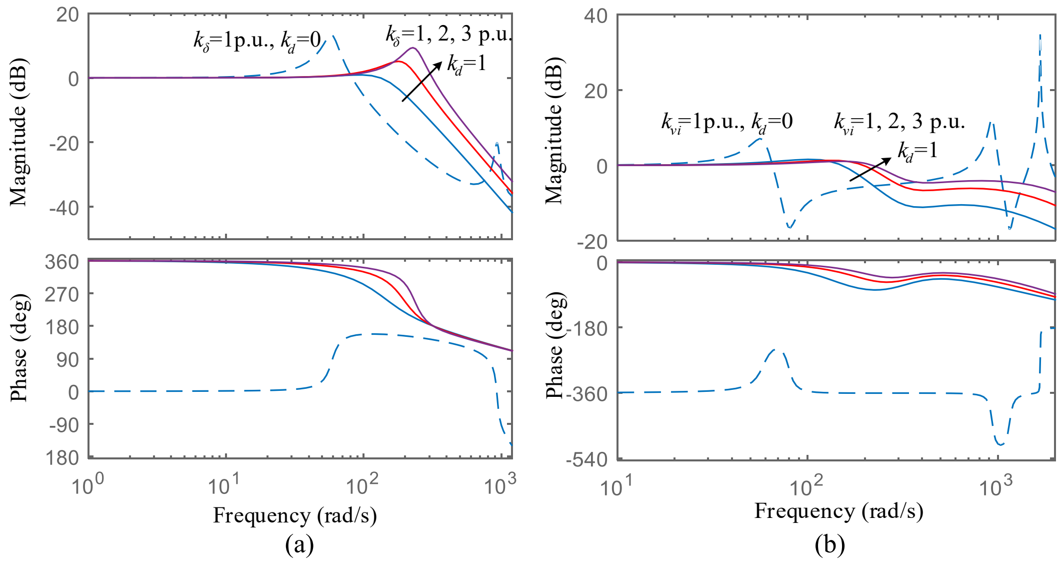

Figure 4.3 Frequency response of the closed-loop transfer functions of the power synchronizing controllers. (a) Active power controller when k_δ increases from 1 to 3 p.u. (b) Voltage control when k_{vi} increases from 1 to 3 p.u. and $k_{vp} \approx 0$.

To investigate the influence of the inner compensation loop on the system performance, the gain k_d has been set to zero when $k_\delta = 1.0$ p.u. As shown in Figure 4.3(a), the CL filter resonance appears in the relatively high-frequency region (around 1000 rad/s) but with a considerable attenuation of -20 dB. However, the negative impact of the CL filter resonance appears on the low-frequency region where the bandwidth of the power controller is remarkably affected. Moreover, a considerable resonance peak with an amplification of 10 dB appears around 60 rad/s. Therefore, the inner compensation loop of the PSC is crucial to maintain the system stability.

4.4.2 The AC Voltage Control Loop

In this chapter, the proportional gain of the PCC voltage controller is negligible ($k_{vp} \approx 0$) [57], [104]. The influence of the integral gain (k_{vi}) on the closed-loop transfer function in (4.11b) is shown in Figure 4.3(b). The bandwidth of the voltage controller is 190, 250, and 300 rad/s when $k_{vi} = 1$, 2, and 3 p.u., respectively. It is shown that as k_{vi} increases, the high-frequency attenuation decreases. Therefore, $k_{vi} = 1$ p.u. is selected. The influence of the inner active compensation loop on the system damping is also shown in Figure 4.3(b). Limited control bandwidth and high-frequency resonance are yielded when the compensation loop is not activated, i.e., when $k_d = 0$. Similar to the power control loop, the inner compensator is necessary.

4.4.3 The DC-Current Control Loop

The closed-loop transfer function of the dc current controller [in (4.12)] can be represented by the standard second-order system. The natural frequency of the dc current controller is $\sqrt{2k_{ii}/L_{dc}}$ whereas the damping ratio is $k_{ip}/\sqrt{2k_{ii}L_{dc}}$. The bandwidth of the dc current controller is designed at 20% of the active power controller whereas a unity damping ratio is considered.

4.5 Small-Signal Analysis

4.5.1 Small-Signal Impedance Characteristics

Using (4.14), the output ac impedance characteristics of the CSC-based PV system with the PSC are investigated. Figure 4.4 shows the frequency response of the ac impedance at different solar insolation levels and SCR values. The SCR is the ratio of the short-circuit capacity of the utility-grid to the rated dc power of the interconnected power converter [36]. It is noted that the CSC topology is characterized by the large magnitude of the output impedance in the low-frequency region that, in general, conforms to the generalized Nyquist stability criterion [45]. At SCR = 5.0, the lightly loaded conditions, i.e., at $G = 0.5\,\mathrm{kW/m^2}$, is associated with the highest magnitude, which implies a higher stability margin [45]. At the high loading conditions, i.e., at $G = 1.0\,\mathrm{kW/m^2}$, both $Z_{dq}(s)$ and $Z_{qq}(s)$ in Figures 4.4(b)-4.5(d), respectively, have an incremental negative resistance characteristics in the low-frequency range. On the contrary, the impedances $Z_{dd}(s)$ and $Z_{qd}(s)$ reflect a real incremental positive resistance in the low-frequency range.

The lightly loaded condition ($G = 0.5\,\mathrm{kW/m^2}$) is investigated at the very weak utility-grid condition at SCR = 1.0. As compared with the case with SCR = 5.0 (solid-black), the impedance of the CSC at SCR = 1.0 (dashed) has a much lower magnitude, which implies a lower stability margin.

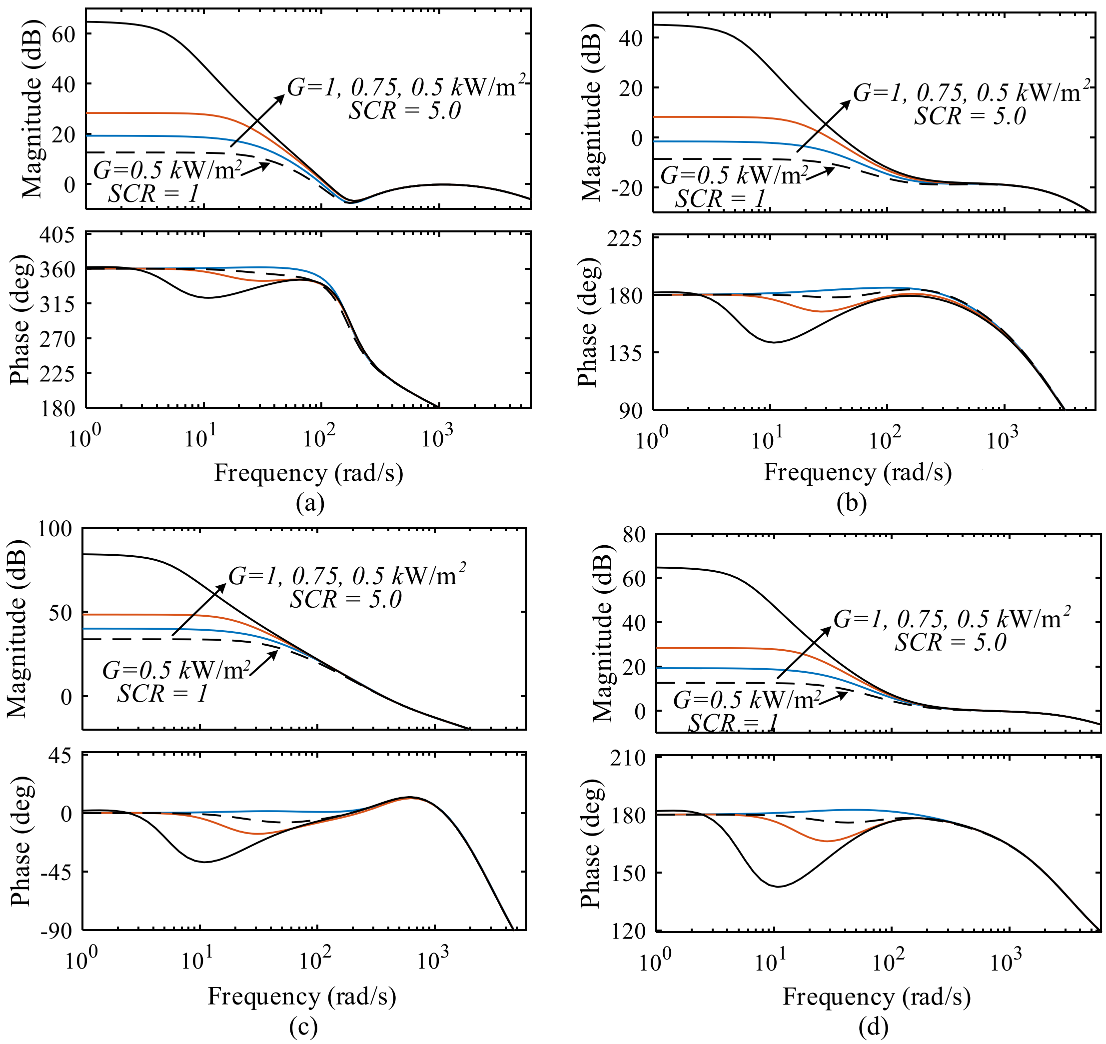

Figure 4.4 Output ac impedance characteristics of the CSC-PV system with the PSC under different solar insolation level and SCR values – (a) $Z_{dd}(s)$. (b) $Z_{dq}(s)$. (c) $Z_{qd}(s)$. (c) $Z_{qq}(s)$.

Despite the lower stability margin, and unlike the vector-controlled converters, it is shown in the following sections that the overall system stability is well-maintained under different operating conditions.

4.5.2 Small-Signal Stability Analysis

Using (4.15), Figure 4.5 shows the most dominant modes when the PV generator injects 1.0 p.u. power to the utility-grid at different SCR levels. The most dominant eigenvalues are $-76.1 \pm j354$, $-138.1 \pm j318.2$, $-202.5 \pm j264.8$, and $-267 \pm j177$ at SCR $= 1$, 2, 3, and 4, respectively. It is clear that the worst-case condition occurs at SCR = 1. However, in all operating conditions, the system stability is well-maintained. Unlike the vector-controlled converters, the PSC has minimal interactions with the utility-grid impedance at very low SCR levels.

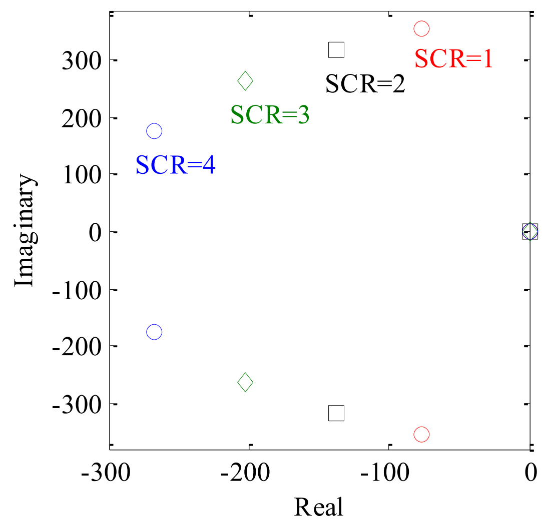

Figure 4.5 Eigenvalue analysis of the CSC-PV system under different SCR levels at $P = 1.0\,\mathrm{p.u.}$

4.6 Evaluation Results

A detailed nonlinear time-domain simulation model for the CSC-based PV system is built under Matlab/Simulink® environment to evaluate the preceding theoretical analysis and validate the performance and the effectiveness of the PSC. The complete model entities are built using the SimPowerSystem® toolbox. The CSC is simulated using the average-model-based blocks. The simulation type is discrete with a sample time of 50 µs.

4.6.1 System Performance at a Relatively Strong Grid

Figure 4.6 shows the system performance when the CSC-based PV system is connected to a utility-grid with SCR = 5.0. To challenge the PSC, step variations in the solar insolation level (G) is applied from 0.5 to 0.75 $\mathrm{kW/m^2}$at $t = 2$ s, and from 0.75 to 1.0 kW/m^2 at $t = 4$ s. A well-damped dc current performance is shown in Figure 4.6(a) whereas the corresponding injected active power response is shown in Figure 4.6(b). The rated active power is injected at $t = 4$ s. The ac current response is shown in Figure 4.6(c). The magnitude of the PCC voltage is maintained at 1.0 p.u. following the step variations in the injected active power as shown in Figure 4.6(d). At the step loading instants, negligible over- and undershoots in the PCC voltage are yielded. The results in Figure 4.6 validate the effectiveness of the PSC in the CSC--interfaced PV generators.

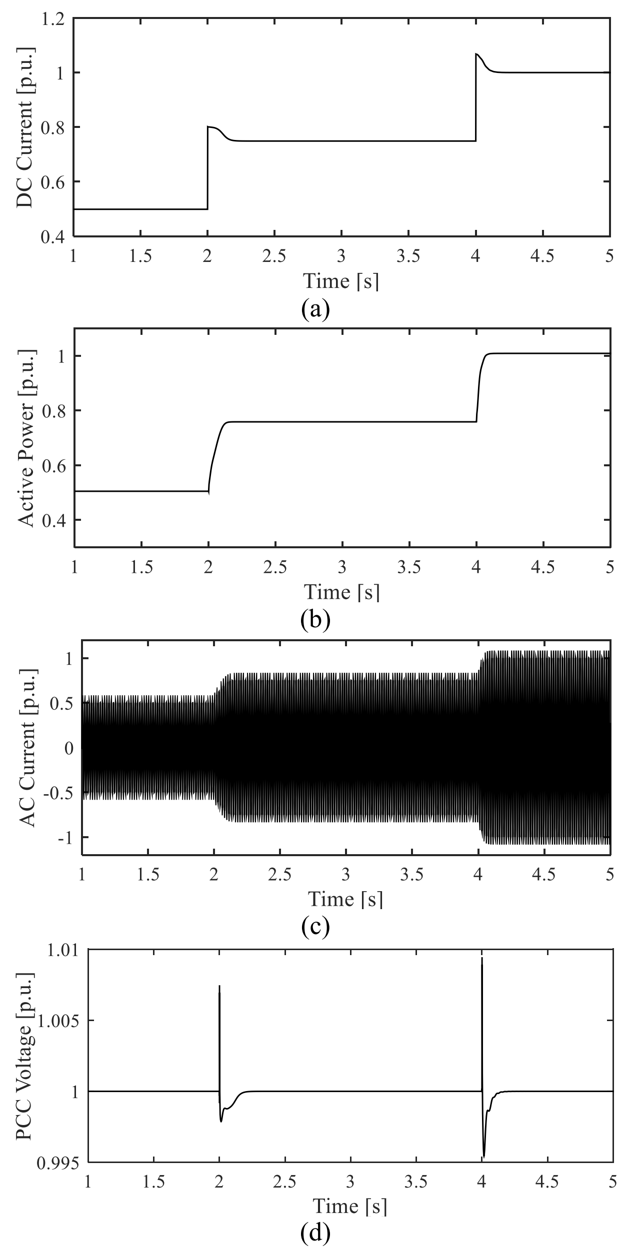

Figure 4.6 CSC performance at SCR = 5.0 and following different solar insolation levels.

4.6.2 System Performance at a Very Weak Grid

The interconnection of the CSC-based PV system to a very weak utility-grid is investigated in this subsection. Figure 4.7 shows the system performance following a step variation in the solar insolation level from 0.75 to 1.0 $\mathrm{kW/m^2}$at $t = 3$ s and $\mathrm{SCR} = 1.0$. Under this challenging condition, the dc current keeps tracking its reference value as shown in Figure 4.7(a). The corresponding active power injection is shown in Figure 4.7(b) where the system stability is maintained. The active power injection at SCR=1 in Figure 4.7(b) has a slight overshoot as compared with the corresponding damped response in Figure 4.6(b) (SCR=5.0). This meets the analytical results in Figure 4.5.

4.6.3 System Performance under Faults Conditions

To investigate the ride-through capability of the CSC with the PSC, different types of faults are applied at the PCC, e.g., single-line-to-ground (SLG) and three-phase-to-ground (3PG). The fault is applied at the PCC of the CSC at $t = 1.0$ s and is cleared after three cycles. In this test, a switching model of the CSC has been built and utilized. The PWM generation method reported in [105] is used. The system performance is shown in Figure 4.8.

Figure 4.8(a) shows the dc and ac current performances following a SLG fault. An undershoot of 0.86 p.u. and an overshoot of 1.185 p.u. are yielded in the dc and ac currents, respectively. Despite the absence of the direct control of the injected ac current, the system performance with the SLG fault is well-damped. The system performance goes worse with the 3PG faults as shown in Figure 4.8(b). An undershoot of 0.53 p.u and overshoot of 3.6 are yielded in the dc and ac current response, respectively.

The results in Figure 4.8 reveal that the 3PG fault has a detrimental influence on the CSC whereas the SLG has a minimal impact. Taking into account that SLG faults are more common in the power system, the performance of the PSC-controlled CSC under this type of fault is remarkably superior.

4.6.4 Comparison to the Power Synchronization Control of the Voltage-Source Converters

As a comparison, the PSC of the grid-connected VSC is investigated in this subsection [44]. For a fair comparison, the PV generator is considered as the input dc source to the VSC whereas similar utility-grid conditions are considered at the ac-side.

A step change in the insolation level from 0.75 to 1.0 $\mathrm{kW/m^2}$at $t = 3$ s is applied at the PV generator side when the SCR level is 1.0. The corresponding performance is shown in Figure 4.9. As compared to Figure 4.7, the system performance is stable at both solar irradiance levels. A similar amount of the reactive power [Figure 4.9(c)] is injected to maintain the magnitude of the PCC voltage at 1.0 p.u. as shown in Figure 4.9(d).

The major difference between the PSC of both converter structures is the fault protection capabilities. Similar fault conditions to the case in Figure 4.8 are applied to the VSC. The system performance following the SLG and 3PG faults are shown in Figure 4.10. As compared to Figure 4.8(a), the performance of the PSC-controlled VSC following the SLG is less damped. At the fault instant, the dc-link voltage has an undershoot of 0.58 p.u. Moreover, the damping of the system oscillations after the fault clearance is delayed to more than 40 cycles. The performance of the VSC following the 3PG fault is shown in Figure 4.10(b). The dc-link voltage drops to zero at the fault instant, suddenly increases to 2 p.u., and decays following an oscillatory response. The injected ac current is unstable with severe harmonic content. As compared to Figure 4.8, the performance of the CSC with the PSC is more stable than the VSC under the fault conditions. This is attributed to the self-protection nature of CSCs due to the regulation of the input dc current.

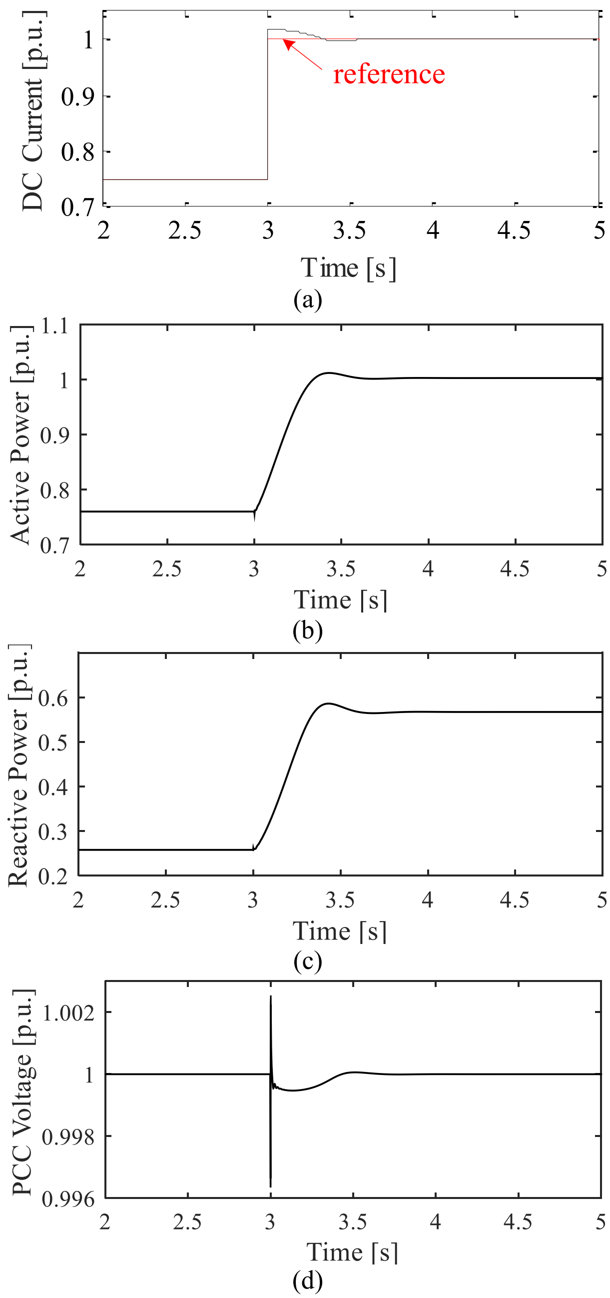

Figure 4.7 CSC performance following a step variation in the solar irradiance from 0.75 to 1.0 kW/m^2 at $t = 3$ s – $SCR = 1.0$.

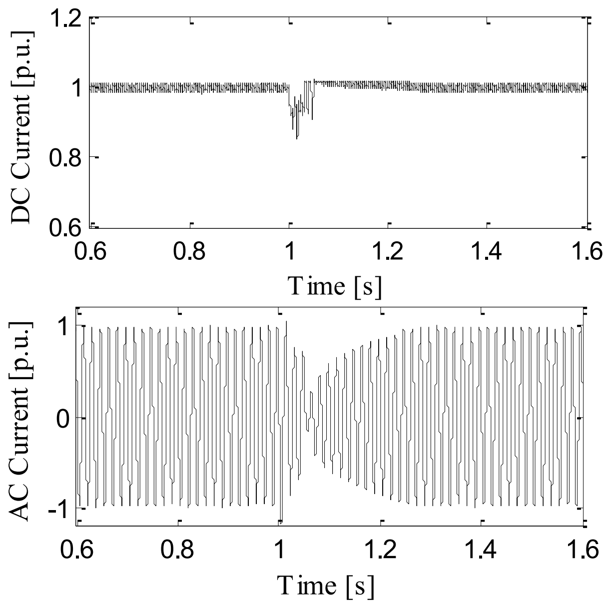

(a)

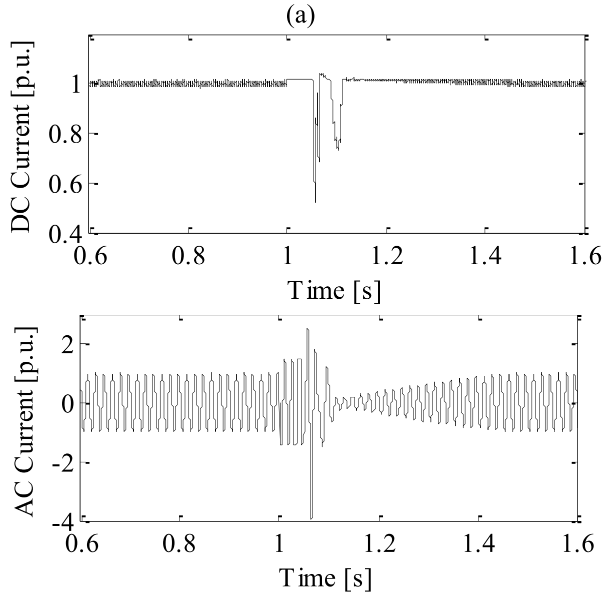

(b)

Figure 4.8 Performance of the PSC of the CSC-based PV system under faults conditions. (a) SLG Fault. (b) 3PG fault.

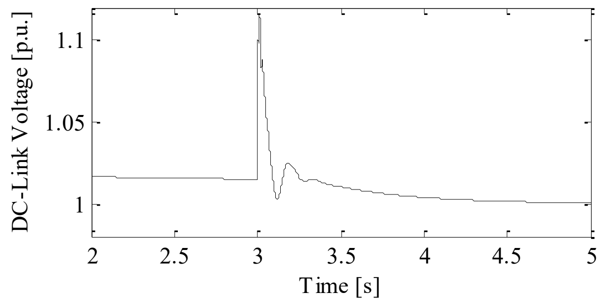

(a)

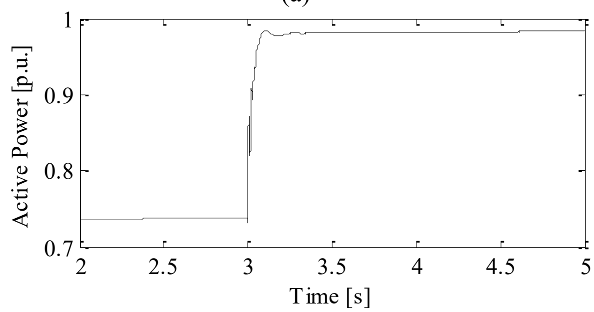

(b)

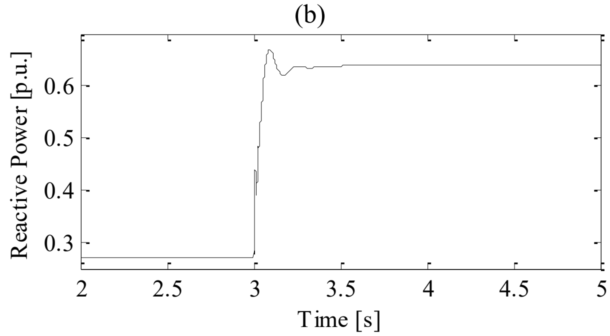

(c)

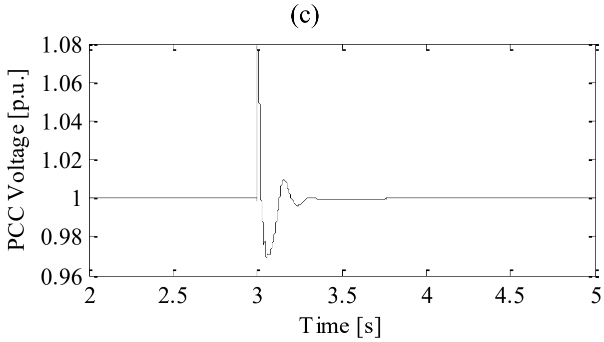

(d)

Figure 4.9 VSC performance following a step variation in the solar irradiance from 0.75 to 1.0 $\mathrm{kW/m^2}$at $\mathrm{t} = 3$ s – $\mathrm{SCR} = 1.0$.

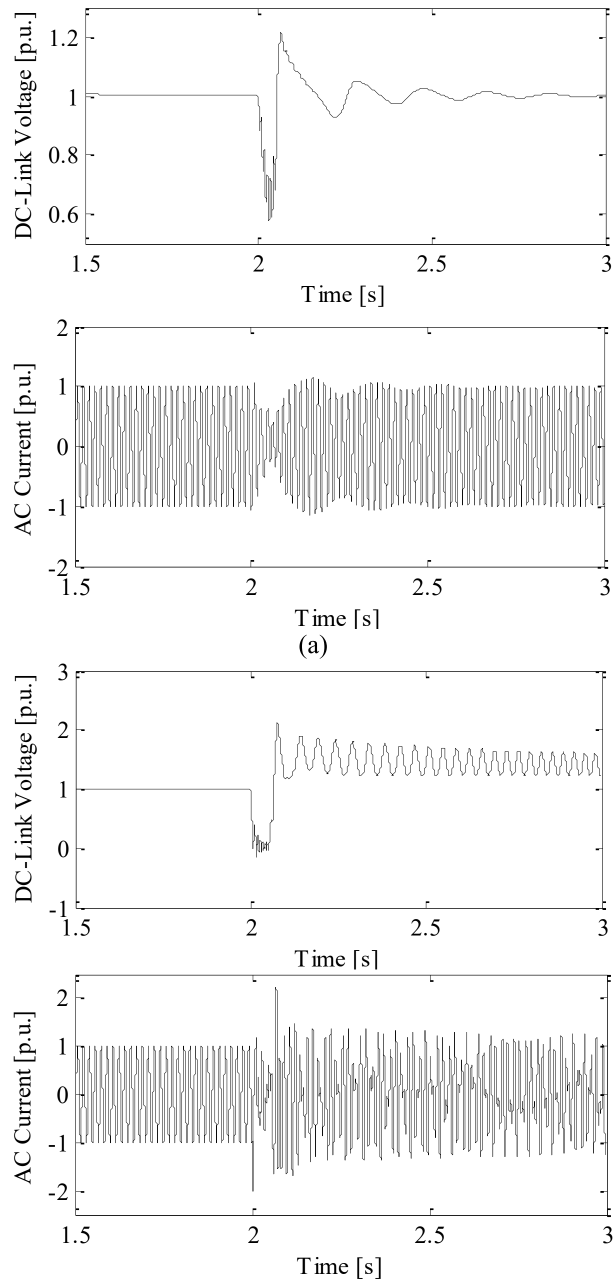

Figure 4.10 Performance of the PSC of the VSC-based PV system under faults conditions. (a) SLG Fault. (b) 3PG fault.

4.7 Conclusions

The PSC of the grid-connected CSC-based PV generation system has been investigated in this chapter. The active power controller is used to control the injected power and synchronize the converter with the utility-grid. Therefore, the PLL is no longer needed with this control scheme. The PSC of the CSC has the following features. 1) A stable performance under very weak utility-grid conditions. 2) A self-current limiting protection, and hence the secondary vector control loop to regulate the injected ac current to the utility-grid at fault conditions is not required (unlike the PSC of the VSCs). 3) A stable performance following sudden variations in the characteristics of the PV generator. Time-domain simulations under Matlab/Simulink environment have been presented to show the effectiveness of the PSC of the CSC-based PV generator.

Chapter 5

An Improved Vector Control Strategy for Current-Source Converters Connected to Very Weak Grids

This chapter investigates the interconnection of CSCs to a very weak utility-grid using the conventional vector control in the rotating reference frame. It is shown that the system stability is degraded under weak-grid conditions due to the implementation of the PLL. Supplementary controllers are proposed and integrated to the outermost control loops of the CSC to alleviate the associated negative impacts of the PLL. The proposed compensators do not alter the dynamic characteristics of the conventional vector control, i.e., the PLL, the current, and the voltage control. More importantly, it could be possible for the CSC to inject 1.0 p.u. of active power at a unity SCR. The small-signal stability analysis and controllers design procedures are presented in details. The design of the proposed compensators is independent of the conventional vector control, and hence no extensive coordination and parameters tuning are needed. Time-domain simulations results are presented to validate the effectiveness of the proposed techniques.

6.1 Modeling and Control of the Grid-Connected Current-Source Converter

A grid-connected CSC is shown in Figure 5.1. More details on the structure of the CSC are presented in Chapter 3. The grid-impedance comprises a large inductive part (L_g) in series with the equivalent resistance of the line (R_g). The values of R_g and L_g are obtained according to (5.1),

$$L_g = \frac{v_g^2}{VA_{sc}} \frac{1}{\omega},$$
$$R_g = \frac{\omega L_g}{XR} \tag{5.1}$$

where VA_{sc} is the short-circuit capacity of the utility-grid [in VA], XR is the inductance-resistance ratio of the transmission line, whereas ω is the angular frequency of the utility-grid.

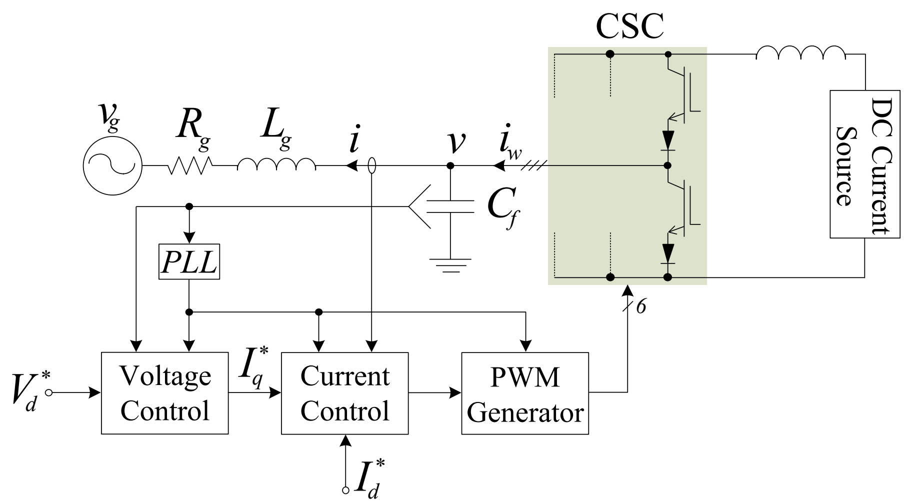

Figure 5.1 A grid-connected current source converter.

5.1.1 Power Circuit Model

The power circuit model of the filter and grid-impedance in the rotating reference frame that rotates by the angular speed ω is as follows,

$$\bar{\iota}_w = \left(sC_f + j\omega C_f\right)\bar{v} + \bar{\iota} \tag{5.2}$$

$$\bar{v} - \bar{v}_g = \left(R_g + sL_g + j\omega L_g\right)\bar{\iota} \tag{5.3}$$

where the complex vector $\bar{x} = X_d + jX_q$ such that X_d and X_q are the direct (d-) and quadrature (q-) component in the rotating reference frame, s is Laplace operator, and j is the imaginary unit number.

5.1.2 PLL Dynamics

As shown in Figure 5.1, the vector control is characterized by the PLL to synchronize the CSC to the utility-grid. The detailed structure of the PLL is shown in Figure 5.2(a). The PCC voltage is decomposed into the equivalent d- and q- components in the rotating reference frame. The grid frequency is then estimated by setting the normalized q-component of the PCC voltage to zero using a PI controller ($G_\delta(s) = K_{p\delta} + K_{i\delta}/s$). The synchronization angle (δ) is obtained by an integrator, and is used in the transformation from the three-phase grid frame to the converter d-q reference frame, and vice versa [38]. Under transient conditions, the angle δ oscillates to resynchronize the converter with the utility-grid and eventually becomes zero at steady-state conditions.

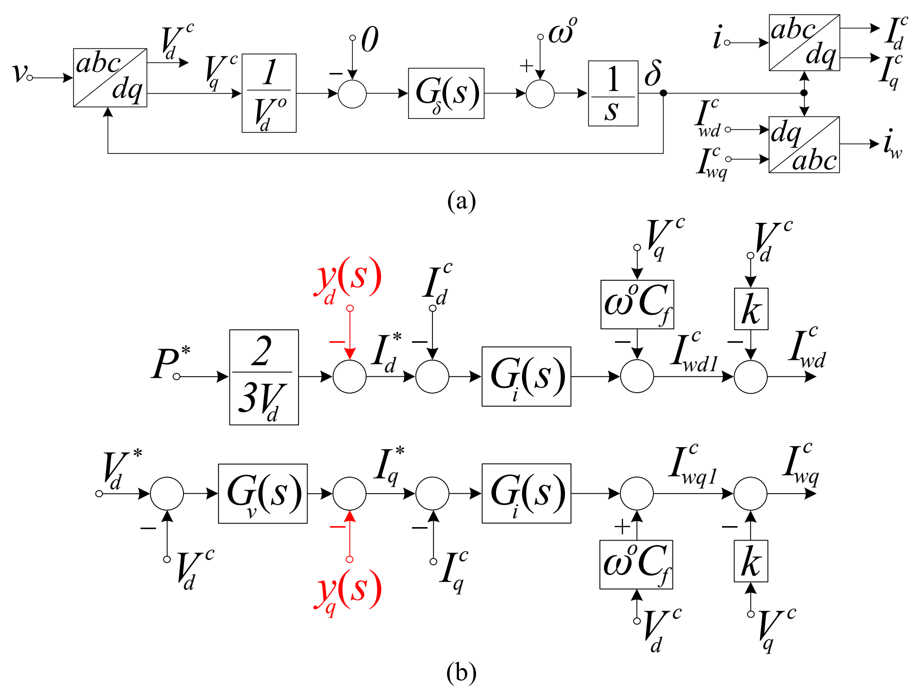

Figure 5.2 Vector control of the grid-connected CSC. (a) SRF-PLL. (b) Voltage and current control.

Referring to Figure 5.2(b), the measured quantities (i.e, i and v) should be transformed to the converter reference-frame whereas the controller output signals (i.e., i_w) should be retransformed to the grid reference frame in order to accurately model the influence of the PLL on the system dynamics [38]-[39]. The frame transformation is mathematically modeled in (5.4), assuming that the angle difference between the two frames is very small such that $\cos\delta \approx 1$ and $\sin\delta \approx 0$,

$$\begin{aligned} \bar{v}^c &= (1 - j\delta)\bar{v}, \\ \bar{\iota}^c &= (1 - j\delta)\bar{\iota}, \\ \bar{\iota}_w &= (1 + j\delta)\bar{\iota}_w^c. \end{aligned} \tag{5.4}$$

where the superscript "c" denotes the converter frame.

5.1.3 Vector Control Structure

The detailed vector control loops of the grid-connected CSC are shown in Figure 5.2(b). The control strategy is developed in two levels; an inner current control, and an outer voltage control. The proposed $y_d(s)$ and $y_q(s)$ loops are to facilitate the interconnection of the CSC to the very weak utility-grid.

5.1.3.1 Inner Current Control

The tracking of the d-q current references (i.e., I_d^* and I_q^*) is achieved via a PI current controller ($G_i(s) = K_{pi} + K_{ii}/s$). Decoupling loops (i.e., $\omega^\circ C_f V_d^c$ and $\omega^\circ C_f V_q^c$) are implement to mitigate the effect of the coupling terms in (5.2). Using (5.2)-(5.3) and Figure 5.2(b), and neglecting the frame transformation in (5.4), the current control dynamics can be obtained as follows.

$$\bar{\imath} = \frac{G_i(s)}{1+G_i(s)}\bar{\imath}^* - \frac{sC_f+k}{1+G_i(s)}\bar{v} \tag{5.5a}$$

$$\bar{\imath} = \frac{G_i(s)}{e^{-sT_d}+G_i(s)}\bar{\imath}^* - \frac{sC_f e^{-sT_d}+k-j\omega C_f\left(1-e^{-sT_d}\right)}{e^{-sT_d}+G_i(s)}\bar{v} \tag{5.5b}$$

The first term in (5.5) reflects the closed-loop current control dynamics. By setting $K_{pi} \approx 0$, the current control bandwidth becomes K_{ii} in $\mathrm{rad/s}$. Based on the rated power of the converter, the range of the current-control time constant (τ_i) is $0.5 - 5$ ms where $K_{ii} = \tau_i^{-1}$ [7]. In is this chapter, $\tau_i = 2.5$ ms.

Similar to Chapter 4, an active damping technique using the gain k is implemented to damp the resonance peak resulted from the combination of C_f and the equivalent grid inductance (L_g). More details on active damping techniques for LC filters are reported in [106].

The controller computational delay and the PWM switching are modeled as a dead time T_d, where $\bar{\imath}_w = \bar{\imath}_w^* e^{-sT_d}$ [38]. The dynamics of the current controller in (5.5a) are investigated when the dead time is considered in the model, and then (5.5a) is modified to (5.5b). Figure 5.3(a) shows the influence of the dead time on the closed-loop transfer function of the current controller in (5.5). The performance of the current controller with and without the dead time is almost identical. The bandwidth of the current controller decreases from 400 rad/s to 360 rad/s when a two-sample delay is considered. The admittance of the current controller, i.e., $\bar{\imath}/\bar{v}$, is not affected by the two-sample delay as shown in Figure 5.3(b). It is clear that the dead time slightly affects the inner current control loop. Therefore, the outer loops remain unaffected as the bandwidth of the inner loop is not significantly reduced to accommodate the delay.

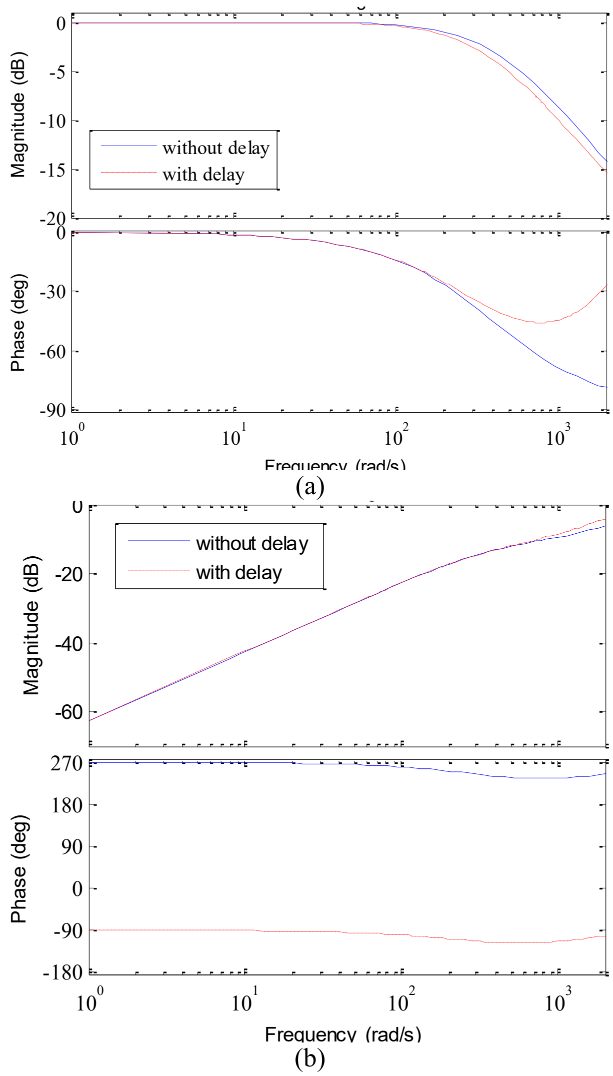

Figure 5.3 Impact of the dead time on the performance of the current controller. (a) $\bar{\imath}/\bar{\imath}^{*}$. (b) $\bar{\imath}/\bar{v}$ – two sample delay.

5.1.3.2 Outer Voltage Control

One of the advantages of implementing the PLL in the vector control of CSC is the decoupled active and reactive power control [107]. As $V_q = 0$, the active power (P) injection is solely dependent on the active current component (I_d) whereas the reactive power injection (Q) is determined by the reactive current component (I_q). This is accurately valid when V_d is regulated which is achieved by using a PI voltage controller ($G_v(s) = K_{pv} + K_{iv}/s$). The reference value of the reactive current component (I_q^*) is therefore obtained as shown in Figure 5.2(b) [108]. As V_d is regulated, the active current reference is simply obtained from $P^* = 1.5V_d I_d^*$.

The voltage controller bandwidth is designed with $10-20\%$ of the bandwidth of the inner current controller. Therefore, the output of the voltage controller is $I_q^* \approx I_q$. Using the d-axis model of (5.3) and neglecting (5.4), the closed-loop transfer- function of the voltage controller is yielded in (5.6). Similar to the current controller design, by setting $K_{pv} \approx 0$, the voltage control bandwidth becomes $\omega L_g K_{iv}$.

$$\frac{V_d}{V_d^*} = \frac{\omega L_g G_v(s)}{1+\omega L_g G_v(s)} \tag{5.6}$$

6.2 Small-Signal Modeling and Analysis

The detailed small-signal modeling of the grid-connected CSC is presented in this section. The complete system parameters are shown in Appendix A5.1 whereas the matrices of the following state-space models are defined in Appendix A5.2. In the following, A, B, C, are the state, input, and output matrices and are multiplied by the corresponding vectors; and Δ represents a small perturbation of the variable.

Using (5.2), (5.4), and the control loops in Figure 5.2, the small-signal state-space model of the grid-connected CSC is as follows,

$$\begin{aligned} \left[\Delta \dot{x}_{conv\_un}\right] &= \left[A_{conv\_un}\right]\left[\Delta x_{conv\_un}\right] + \left[B_{conv\_un}\right]\left[\Delta I_{dq}\right] + \left[B_{conv1\_un}\right]\left[\Delta y_{dq}\right], \\ \left[\Delta V_{dq}\right] &= \left[C_{conv\_un}\right]\left[\Delta x_{conv\_un}\right]. \end{aligned} \tag{5.7}$$

where $\left[\Delta x_{conv\_un}\right] = [\Delta V_d \quad \Delta V_q \quad \Delta\varphi_{id} \quad \Delta\varphi_{iq} \quad \Delta\varphi_v \quad \Delta\delta \quad \Delta\varphi_\delta]^T$, $\left[\Delta I_{dq}\right] = [\Delta I_d \quad \Delta I_q]^T$, $\left[\Delta y_{dq}\right] = [\Delta y_d \quad \Delta y_q]^T$, and $\left[\Delta V_{dq}\right] = [\Delta V_d \quad \Delta V_q]^T$.

The states ($\Delta\varphi_{id}$, $\Delta\varphi_{iq}$), ($\Delta\varphi_v$), and ($\Delta\delta$, $\Delta\varphi_\delta$), represents the integral terms of the current, the voltage, and the PLL control loops, Δy_{dq} is the input vector from the proposed compensation loops and is set to zero here. From (5.7), the 2×2 output impedance matrix of the uncompensated CSC ($\Delta Z_{c_{un}}(s)$) as seen from the PCC is as follows.

$$[\Delta V_{dq}] = \left[C_{conv\_un}(sI - A_{conv\_un})^{-1} B_{conv\_un}\right][\Delta I_{dq}] \tag{5.8}$$

The input vector ΔI_{dq} in (5.7) is obtained from the small-signal representation of (5.3), and hence the final state-space model of the uncompensated system is as follows,

$$[\Delta x_{tot\_un}] = [A_{tot\_un}][\Delta x_{tot\_un}] \tag{5.9}$$

where $[\Delta x_{tot\_un}] = [\Delta x_{conv\_un} \quad \Delta I_{dq}]$.

As shown in Table 5.1, the system stability is preserved up to $P = 0.7\,\mathrm{p.u.}$ In the stable operating range, the system stability margin increases as the amount of active power injection increases. For instance, the damping ratio increases from 0.049 to 1.0 at $P = 0.2$ and $0.7\,\mathrm{p.u.}$, respectively. Note that the most dominant eigenvalues at $P = 0.6$ and $0.7\,\mathrm{p.u.}$ are influenced by the PLL controller ($\Delta\varphi_\delta$) and the frame transformation angle ($\Delta\delta$). At $P = 0.8\,\mathrm{p.u.}$, the dominant mode is migrated to the right-hand side of the s-plane and hence the system stability is violated. As shown in Table 5.1, the instabilities are induced by the orientation angle ($\Delta\delta$) of the PLL.

The unstable performance of the CSC at the very weak utility-grid condition is attributed to the power transfer mechanism between the sending bus at the CSC terminals (v) and the receiving end at the back emf of the utility-grid (v_g) [44], where $P = \frac{VV_g}{\omega L_g} sin\delta$, assuming high XR ratio. At this weak condition, ωL_g is maximized, and hence the angle δ has to increase to transmit the same amount of active power (P). Therefore, the operating points move to the non-linear region on the $P - \delta$ curve such that δ approaches $\pi/2$ rad/s at the rated power operation under a unity SCR level. More importantly, and due to the implementation of the PLL, the grid and converter dynamics become highly coupled under weak grid conditions. For these reasons, instabilities are yielded in weak-grid-connected power converters.

Table 5.1 Dominant Eigenvalues of the Uncompensated System

P [p.u.]	Dominant Modes	Influencing State(s)
0.2	$\lambda_{1,2} = -12 \pm j240.8$	$\Delta\varphi_{iq}$
	$\lambda_3 = -19.9$	$\Delta\varphi_\delta$
0.4	$\lambda_1 = -19.7$	$\Delta\varphi_\delta$
	$\lambda_{2,3} = -41.2 \pm j211.4$	$\Delta\varphi_{iq}$
0.6	$\lambda_1 = -19.5$	$\Delta\varphi_\delta$
	$\lambda_{2,3} = -56 \pm j155$	$\Delta\delta$
0.7	$\lambda_1 = -19.4$	$\Delta\varphi_\delta$
	$\lambda_{2,3} = -28.4 \pm j102.5$	$\Delta\delta$
0.8	$+0.81 \pm j82.2$	$\Delta\delta$
1.0	$+39.6 \pm j35.6$	$\Delta\varphi_v$,$\Delta\delta$

Figure 5.4 shows the frequency response of $\Delta Z_{c_{un}}(s)$ of the CSC [in (5.7)]. Based on the Nyquist stability criterion, the magnitude of the output impedance of the CSC should be as high as possible in order to preserve the system stability [45]-[47]. As shown in Figure 5.4, the light loading of the CSC is associated with the highest magnitude of the converter impedance which implies a stable performance [Table 5.1]. However, at $P = 1.0$ p.u., the magnitude of the small-signal impedance decreases which in turns maximizes the influence of the large grid-inductance on the system stability. Note that $\Delta Z_{c_{dq_{un}}}(s)$ does not follow this trend due to the associated coupling terms. Figure 5.4 also shows the frequency response of $\Delta Z_{c_{un}}(s)$ at a unity active power injection when the PLL dynamics are ignored (dashed-red). As compared to the case when the PLL is considered (blue), both responses have a similar behavior beyond 100 rad/s but significantly deviate at low frequencies. It is shown that the "no-PLL" case reflects a high magnitude of the CSC impedance. This implies that the PLL dynamics are the main source of instabilities as it reduces the magnitude of the converter impedance at low frequencies.

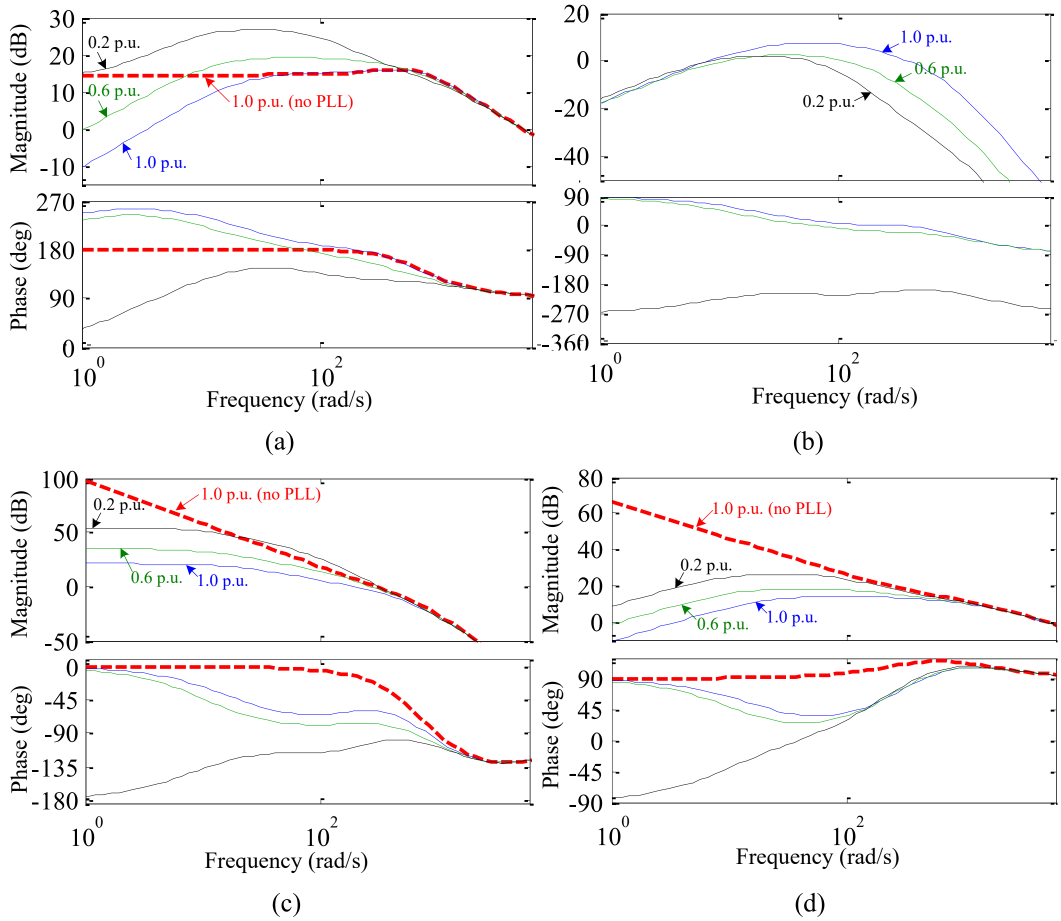

Figure 5.4 Frequency response of $\Delta Z_{c_{un}}(s)$ at different power levels. (a) $\Delta Z_{c_{dd_{un}}}(s)$. (b) $\Delta Z_{c_{dq_{un}}}(s)$. (c) $\Delta Z_{c_{qd_{un}}}(s)$. (d) $\Delta Z_{c_{qq_{un}}}(s)$.

6.3 Proposed Active Compensation Techniques

The PLL loop has been eliminated as introduced in Chapter 4 in order to alleviate the interactions between the PLL and the utility-grid impedance. The vector control in the stationary Alpha (α)-Beta (β) frame that does not depend on the PLL can be also implemented. However, the control in the $\alpha - \beta$ has it is own challenges; 1) From the control systems point of view, it is desirable and easier to track and reject dc (or slowly varying) signals as compared to sinusoidal signals. Therefore, the vector control of power converters in the d-q frame is more common. 2) Power system dynamics are usually modeled and characterized in the standard d-q frame. Therefore, studies involving power converter interactions with power grids are preferably conducted in the d-q frame. Interfacing the converter dynamics with its controller implemented in the $\alpha - \beta$ frame to the power system dynamics in the d-q frame is not straight-forward. 3) The implementation of resonant controllers and filters, needed for a control system implemented in the $\alpha - \beta$ frame, requires much greater care in the algorithm design. In this chapter, an active compensation technique is proposed in the PLL-based vector control to introduce additional degrees-of-freedom to stabilize the system dynamics.

As shown in Figure 5.2(b), the compensation signals ($y_d(s)$ and $y_q(s)$) are added to the d- and q-channel of the vector control. The proposed compensation signals are as follows.

$$y_d(s) = k_d \frac{2\xi_d \omega_d s}{s^2 + 2\xi_d \omega_d s + \omega_d^2} \omega. \tag{5.10a}$$

$$y_q(s) = y_{qq}(s) + y_{ff}(s),$$
$$y_{qq}(s) = k_q \frac{\omega_q}{s+\omega_q} V_q^c,$$
$$y_f(s) = -k_f \frac{\omega_f}{s+\omega_f} V_d^c \tag{5.10b}$$

The compensator signals are desinged based on the fact that the PLL is the dominant detrimental element in the vector-controlled converters in weak grid systems [37]-[40]. Therefore, the output of the PLL, i.e., ω, is used as the input signal to the compensation function in (5.10a), whereas the control variable of the PLL, i.e., V_q^c, is utilized in (5.10b) to obtain the compensation signal $y_{qq}(s)$. The frequency ω is then applied over a band-pass filter to obtain $y_d(s)$, where ξ_d is the damping ratio and ω_d is the cut-off frequency. The voltage signal V_q^c is applied to an LPF with a cut-off frequency ω_q and a gain k_q. Note that the output of $y_d(s)$ and $y_{qq}(s)$ is zero in steady-state conditions and hence the proposed compensators do not affect the tracking of the control variables.

In addition to $y_{qq}(s)$, the PCC voltage (V_d^c) is applied to an LPF with a cut-off frequency ω_f and a gain k_f to obtain $y_f(s)$. It is shown that $y_f(s)$ introduces further damping and enhanced disturbance rejection at the instants of sudden loading. However, $y_d(s)$ and $y_{qq}(s)$ are sufficient to maintain the system stability at the very weak grid conditions.

5.3.1 Small-Signal Modeling of the Compensated System

Four states are added to the uncompensated model in (5.9); three from the proposed compensator and one from the feed-forward loop. The state-space model representation of the proposed compensator is as follows,

$$[\Delta \dot{x_c}] = [A_c][\Delta x_c] + [B_c][\Delta V_{dq}^c] + [B_{cw}]\Delta\omega,$$
$$[\Delta y_{dq}] = [C_c][\Delta x_c]. \tag{5.11}$$

where $\Delta x_c = [\Delta\gamma_{d1} \quad \Delta\gamma_{d2} \quad \Delta\gamma_{q1} \quad \Delta\gamma_{q2}]^T$ and $\Delta V_{dq}^c = [\Delta V_d^c \quad \Delta V_q^c]^T$.

The model in (5.11) is solved with (5.7) and the grid model in (5.4), and the final state-space model of the compensated system is shown in (5.12) where $[\Delta x_{tot\_comp}] = [\Delta x_{conv\_comp} \quad \Delta I_{dq}]$.

$$[\Delta \dot{x}_{tot\_comp}] = [A_{tot\_comp}][\Delta x_{tot\_comp}] \tag{5.12}$$

5.3.2 Stability Analysis and Compensators Design

The design of the proposed compensators in (5.10) is achieved over three steps: 1) design of $y_{qq}(s)$. 2) design of $y_d(s)$ considering $y_{qq}(s)$. 3) design of $y_f(s)$ considering $y_{qq}(s)$ and $y_d(s)$. In all steps, the worst case scenario, i.e., SCR $= 1$, is firstly considered.

5.3.2.1 Design of $y_{qq}(s)$

Starting with (5.10b), the compensator $y_{qq}(s)$ is considered in the small-signal model in (5.12) when $P = 1.0$ p.u. Figure 5.5(a) shows the corresponding influence on the system damping as k_q increases from 0 to 3, under different cut-off frequencies. It is clear that low ω_q implies higher system damping. Therefore, k_q and ω_q are designed at 1.5 and 30 rad/s, respectively. At $P = 1$ p.u. and SCR $= 1.0$, the most dominant eigenvalue is relocated to $-7.1 \pm j195.2$ which is influenced (damped) by the state of the proposed compensator ($\Delta\gamma_{q2}$). The influence of the designed parameters on the system damping under different operating conditions is investigated in Figure 5.5(b). In spite of the maintained system stability under the entire loading levels, the damped performance at $P = 1.0$ p.u. is negatively affected when the loading conditions decreases to $P = 0.6$ and 0.8 p.u. Referring to Table 5.1, the uncompensated most dominant conjugate-complex mode at $P = 0.6$ p.u. is $-56 \pm j155$, whereas the damping of this mode decreases to $-3 \pm j238$ in Figure 5.5(b). This trade-off is mitigated by adding $y_d(s)$ to the system model.

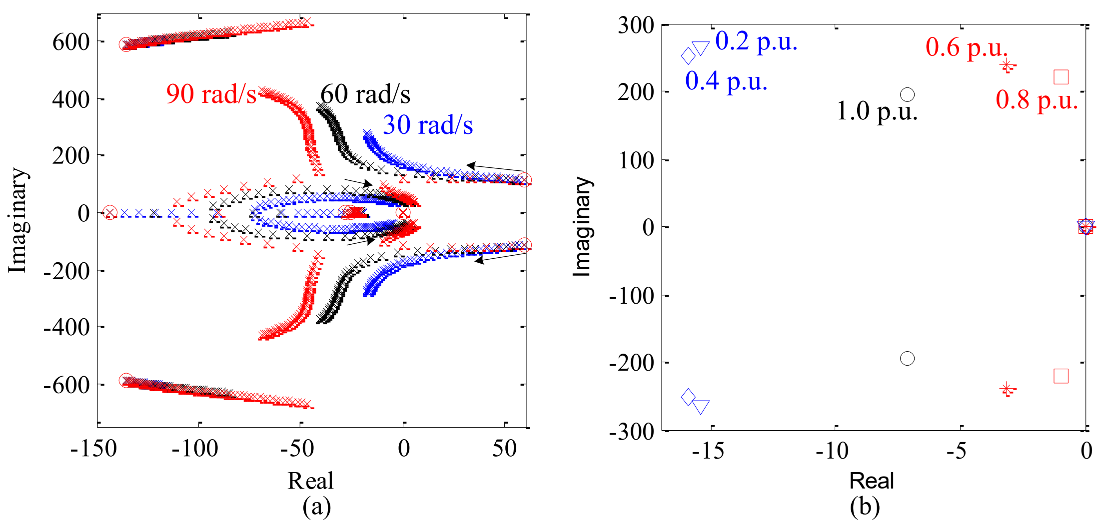

Figure 5.5 Influence of $y_{qq}(s)$ on the system dynamics at SCR = 1.0. (a) k_q increases from 0 to 3 under different cut-off frequencies – $P = 1.0$ p.u. (b) $k_q = 1.5$ and $\omega_q = 30$ rad/s at different loading conditions.

5.3.2.2 Design of $y_d(s)$

The state-space model is investigated when both $y_d(s)$ and $y_{qq}(s)$ are considered. Figure 5.6(a) shows the locus of the most dominant modes at $P = 0.6$ p.u. As compared to Figure 5.5(b), the compensation signal in (5.10a) successfully relocates the most dominant modes to more damped locations. Following Figure 5.6(a), the selected compensator gain (k_d) and the cut-off frequency (ω_d) are 20 and 600 rad/s, respectively, whereas $\xi_d = 1.0$. The effect of $y_d(s)$ and $y_{qq}(s)$ on the system dynamics under different loading conditions is shown in Figure 5.6(b). As compared to Table 5.1, the proposed compensators successfully maintain a stable performance under all loading conditions. The CSC is capable to inject the full rated active power at SCR = 1.0.

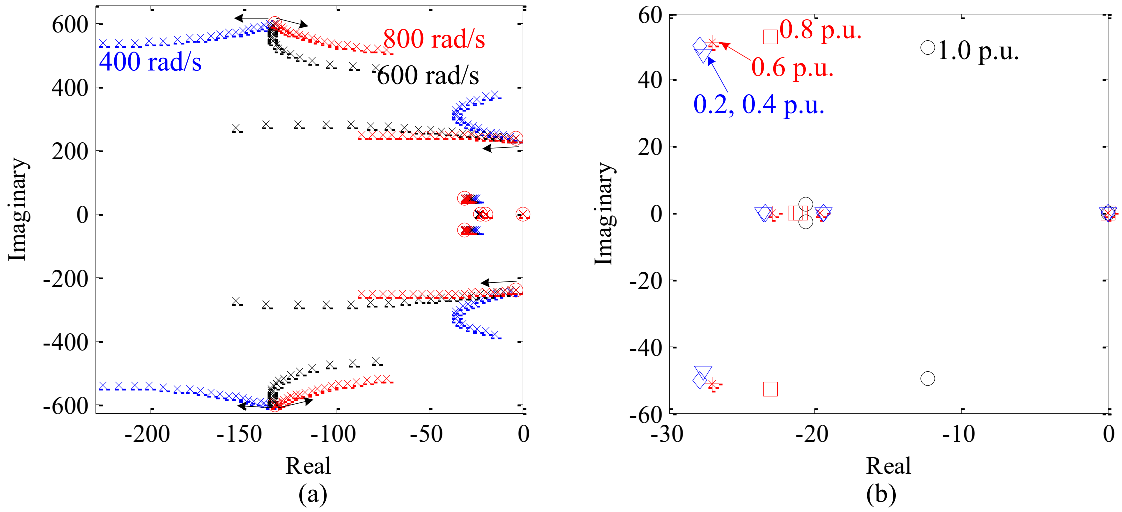

Figure 5.6 Influence of $y_{qq}(s)$ and $y_d(s)$ on the system dynamics at SCR = 1.0 – $k_q = 1.5$ and $\omega_q = 30$ rad/s. (a) P = 0.6 p.u, k_d increases from 0 to 20, $\xi_d = 1.0$, and $\omega_d = 400,\ 600,\ 800$ rad/s. (b) Different active power levels, $k_d = 20$, $\xi_d = 1.0$, and $\omega_d = 600$ rad/s.

5.3.2.3 Design of $y_f(s)$

In spite of the introduced system damping by the proposed $y_d(s)$ and $y_{qq}(s)$ compensators, the presence of $y_f(s)$ is found to provide more damping capabilities and enhanced disturbance rejection at the instants of loading variations. Figure 5.7(a) shows the locus of the most dominant modes of the CSC at SCR=1.0 and active power injection of 1.0 p.u. Both compensators, i.e., $y_d(s)$ and $y_{qq}(s)$, are considered while the gain of $y_f(s)$ increases from 0 to 0.3 at different cut-off frequencies (ω_f). More damped performance is yielded with $k_f = 0.3$ and $\omega_f = 30$ rad/s. Figure 5.7(b) shows the locus of the dominant modes when the proposed compensators in (5.10) are all implemented at different levels of active power injection. As compared to Figure 5.6(b), more damped performance is apparently observed.

6.4 Evaluation Results

A large-signal time-domain simulation model for the grid-connected CSC is built under Matlab/Simulink® environment to evaluate the preceding theoretical analysis and validate the influence of the proposed compensators. A very weak utility-grid is considered at SCR = 1.0. The complete model entities are built using SimPowerSystem® toolbox. The CSC is simulated using average-model-based blocks. The simulation type is discrete with a sample time of 50µs.

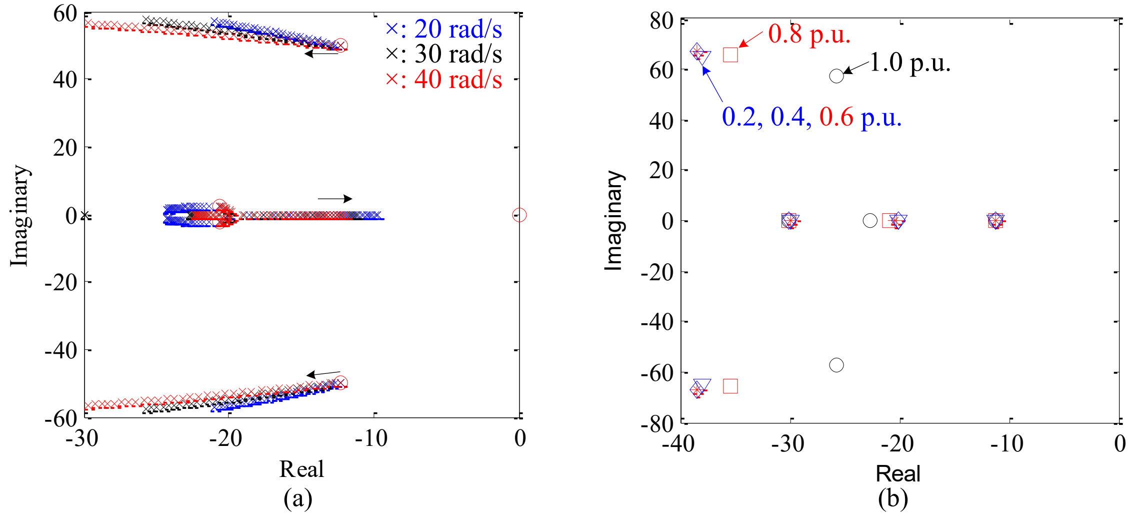

Figure 5.7 Influence of $y_{qq}(s)$, $y_d(s)$, and $y_f(s)$ on the system dynamics at SCR = 1.0 – $k_q = 1.5$ and $\omega_q = 30$ rad/s, $k_d = 20$, $\omega_d = 600$ rad/s, $\xi_d = 1.0$. (a) P = 1.0 p.u, k_f increases from 0 to 0.3 and $\omega_f = 20$, 30, 40 rad/s. (b) Different active power levels, $k_f = 0.3$ and $\omega_f = 30$ rad/s.

5.4.1 Uncompensated System – Small-Signal Model Validation

The uncompensated system response is investigated in this subsection. The control topology in Figure 5.2 is implemented in the Simulink model but ignoring the proposed compensators. Figure 5.8 shows the response of the active power injection to the utility-grid. Figures 5.8(a)-5.7(c) reflect a lightly damped performance at low-medium active power loading. The system stability is preserved until the active power injection level increases to $0.8\,\mathrm{p.u.}$ as shown in Figure 5.8(d). Note that a small step in the active power command from 0.79 to $0.8\,\mathrm{p.u.}$ is sufficient to induce the system instabilities.

The accuracy of the small-signal state-space models in (5.9) are evaluated in Figure 5.8. For an eigenvalue $\lambda = -\sigma \pm j\omega$, the frequency of oscillation is ω [in $\mathrm{rad/s}$] whereas the envelope of the oscillatory response decays following the exponential function Aexp(−σt), where A is the amplitude of the oscillation and t is the time in seconds [51]. Referring to Table 5.1, the frequency of oscillation of the dominant conjugate-complex modes at $P = 0.2$, 0.4, 0.6, and $0.8\,\mathrm{p.u.}$ is 240.8, 211.4, 155, and $82.2\,\mathrm{rad/s}$, respectively. The corresponding frequency of oscillation of the large-signal time-domain results is shown in Figure 5.8, which closely meets the analytical results. Moreover, the corresponding exponential function, i.e., $\mathrm{A}\exp(-\sigma t)$, is plotted on Figure 5.8 where σ is taken from the analytical model in Table 5.1 whereas A is measured from the time-domain simulation results. The analytically plotted red-dashed envelopes in Figure 5.8 closely match the behaviour of the time-domain signals. Figure 5.8 successfully validates the accuracy of the developed small-signal models.

5.4.2 Compensated System

The proposed compensators in (5.10) are implemented in the time-domain model and investigated in this subsection.

5.4.2.1 Influence of $\boldsymbol{y_{qq}(s)}$

Figure 5.9(a) shows the response of the injected active power at SCR $= 1$ when the compensator $y_{qq}(s)$ is implemented. As compared to Figure 5.8(d), the system stability is maintained at the full rated power injection to a very weak utility-grid. In spite of the stable performance at $P = 1.0\ \mathrm{p.u.}$, the system damping is significantly degraded at medium loading levels as shown in Figure 5.9(b) where $P = 0.6\ \mathrm{p.u}$. The results in Figure 5.9 meet the eigenvalues analysis in Figure 5.5(b).

5.4.2.2 Influence of $\boldsymbol{y_{qq}(s)}$ and $\boldsymbol{y_d(s)}$

The proposed compensator in (5.10a) is added to $y_{qq}(s)$ in order to enhance the system damping. As compared to Figure 5.9(a), the damping of the high frequency oscillations of the injected full active power is enhanced as shown in Figure 5.10(a). These results verify the eigenvalue analysis in Figures 5.5(b)-5.5(b) where the dominant mode changes from $-7.1 \pm j195$ when $y_{qq}(s)$ is implemented to $-12.3 \pm j49.7$ when $y_d(s)$ is added [$P = 1.0\ \mathrm{p.u}$]. The associated trade-off with the implementation of $y_{qq}(s)$ at medium power injection is mitigated by adding $y_d(s)$ as clearly shown in Figure 5.10(b). The analytical results reveal similar influence as previously investigated in Figures 5.5(b)-5.6(b).

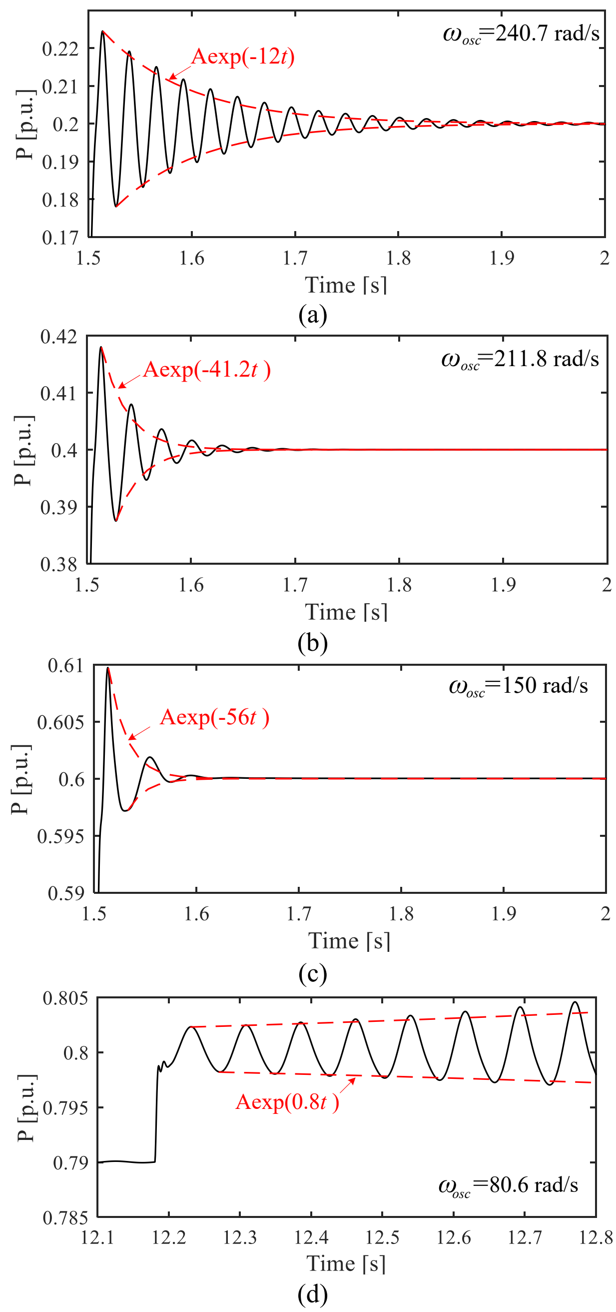

Figure 5.8 Uncompensated CSC response at different levels of active power loading – small-signal model verification. (a) $P = 0.2\ \mathrm{p.u.}$ (b) $P = 0.4\ \mathrm{p.u.}$ (6) $P = 0.6\ \mathrm{p.u.}$ (8) $P = 0.8\ \mathrm{p.u.}$

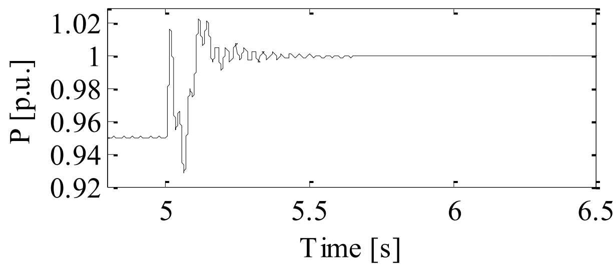

(a)

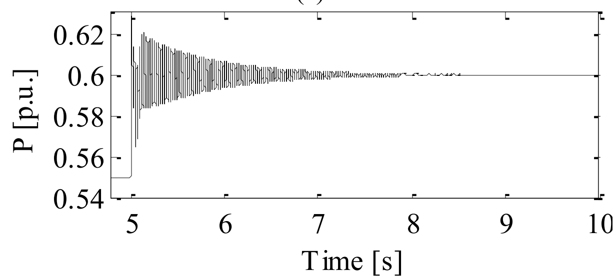

(b)

Figure 5.9 Influence of $y_{qq}(s)$ on the damping of the grid-connected CSC – SCR $= 1.0$. (a) $P = 1.0\ \mathrm{p.u.}$ (b) $P = 0.6\mathrm{p.u.}$

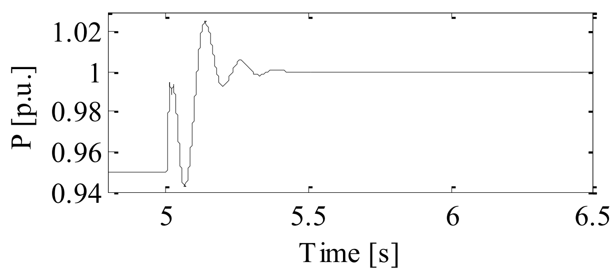

(a)

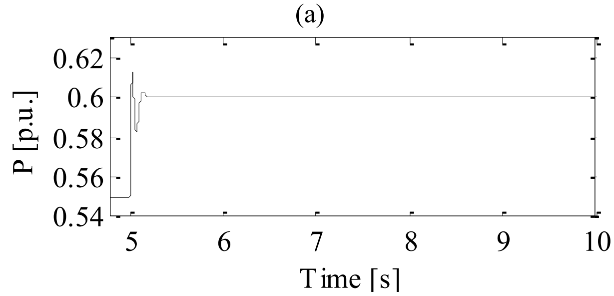

(b)

Figure 5.10 Influence of $y_{qq}(s)$ and $y_d(s)$ on the damping of the grid-connected CSC – SCR $= 1.0$. (a) $P = 1.0\ \mathrm{p.u.}$ (b) $P = 0.6\mathrm{p.u.}$

5.4.2.3 Highly Damped Performance

The proposed compensators in (5.10) are all implemented in the time-domain model, and the system performance is investigated in this subsection. Figure 5.11(a) shows the injected active power to the utility-grid. The active power commands are 0.4, 0.6, 0.8, and 1.0 at $t = 1.0$, 2.0, 3.0, 4.0 s, respectively. The high damped performance that is concluded from Figure 5.7(b) is clearly reflected to the time-domain results. The magnitude of the PCC voltage is shown in Figure 5.11(b) where a unity $\mathrm{p.u.}$ value is maintained under different loading conditions by injecting the corresponding reactive power to the grid. The injected current (i) to the utility-grid is shown in Figure 5.11(c). As mentioned earlier, the compensation signals have a zero steady-state value and hence they do not alter the accuracy of the controlled parameters which is clear from Figure 5.11(d).

A switching model of the grid-connected CSC system is built under Matlab/Simulink for further investigations. The PWM technique in [105] has been implemented to obtain the switching patterns for IGBTs. Following the simulation scenario in Figure 5.11, Figure 5.12 shows the loading instant from 0.8 to 1.0 $\mathrm{p.u.}$ at $t = 4$ s [phase a only]. Similar results to those obtained in Figure 5.11(c) are yielded.

The compensated CSC is further challenged at $P = 1.0\ \mathrm{p.u.}$ and $\mathrm{SCR} = 1.0$ by varying the parameters of the utility-grid voltage (v_g). Figure 5.13 shows the influence of shifting the phase angle of v_g by 30° between $\mathrm{t} = 1.4$ and $1.8\ \mathrm{s}$. The active power injection suffers from an overshoot of 1.4 p.u. and undershoot of 0.281 p.u. at $t = 1.4$ and 1.8 s, respectively. However, the system stability is preserved. The similar conditions have been applied to the uncompensated system at $\mathrm{P} = 0.7\ \mathrm{p.u.}$ where the system stability is clearly violated. This implies the robustness of the proposed compensators against grid-voltage parameter variations.

5.4.2.4 Sensitivity Results

The influence of the proposed compensators on the dynamics of the CSC is investigated in this subsection. The frequency of the utility-grid voltage (v_g) is perturbed by 1 Hz at $t = 1.4$ s and the output of the PLL is shown in Figure 5.14(a). At $P = 0.7\ \mathrm{p.u.}$, the compensated and uncompensated responses are similar. The response of the compensated system at $P = 1.0\ \mathrm{p.u.}$

is also shown where similar characteristics are observed.

The response of I_d is shown in Figure 5.14(b) when the active power command increases from 0.6 to $0.7\ \mathrm{p.u.}$ at $t = 1$ s. As compared to the uncompensated case, the influence of the proposed compensators on the current tracking is positive where the current overshoot and oscillations are reduced due to the increased damping. The impact of both compensators on the tracking response of the voltage controller is not significant as clearly shown in Figure 5.14(c) when a 0.05 p.u. step change in the PCC voltage is applied at $t = 1.4$ s.

6.5 Conclusions

To faciliate the use of the vector control strategy in a very weak grid-connected CSC, active compensation techniques have been proposed to alleviate the negative impacts of the PLL under weak grid conditions. Unlike the uncompensated converter where the system undergoes instabilities beyond $P = 0.8\ \mathrm{p.u.}$, the rated active power injection has been achieved with the proposed techniques. Small-signal state-space model of the entire system is developed in order to investigate the system dynamics under weak grid conditions, and to design the compensators parameters. The proposed compensators have the following features. 1) They are simple and can be easily designed using linear analysis tools. 2) They do not influence the steady-state operation of the CSC. 3) They have no effect on the dynamics of the PLL, the current, and the voltage controllers; therefore, the proposed compensators can be augmented with the standard vector controller without major changes in the controller structure and/or parameters. 4) They are robust under different operating conditions. Time-domain simulations have been provided to validate the developed analytical models and reflect the effectiveness of the proposed techniques.

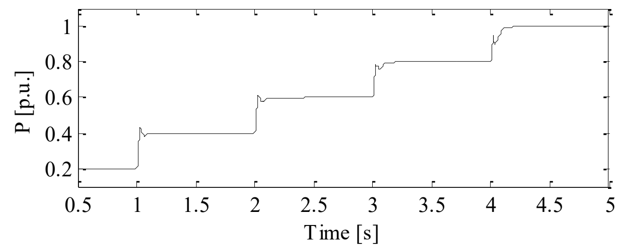

(a)

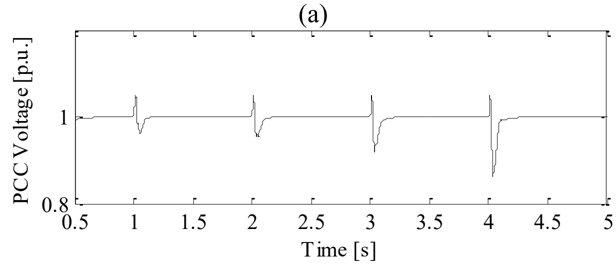

(b)

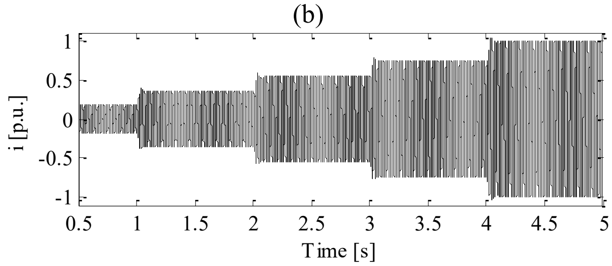

(c)

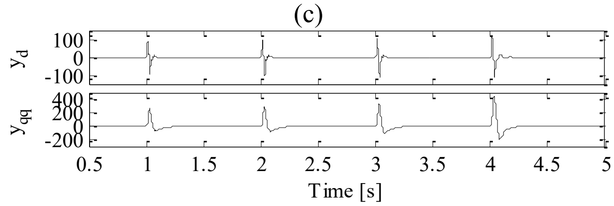

(d)

Figure 5.11 Average model of the CSC at SCR = 1.0. (a) Active power. (b) PCC voltage. (c) Injected current to the grid. (d) Compensation signals.

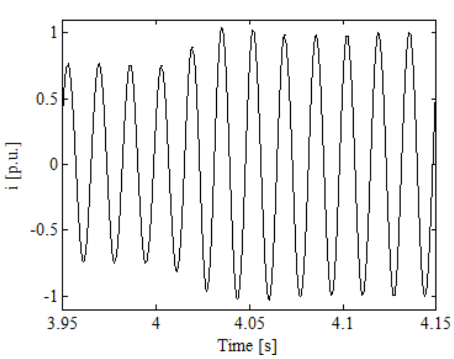

(a)

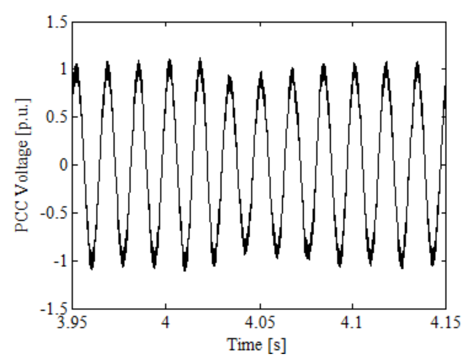

(b)

Figure 5.12 Switching model of the CSC at SCR = 1.0. (a) Injected current. (b) PCC voltage.

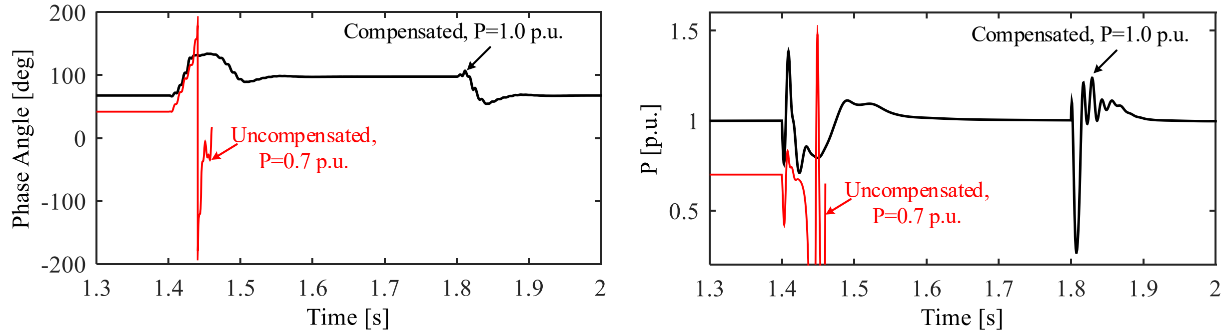

Figure 5.13 Influence of applying a 30° phase shift of the grid-voltage (v_g) from $t = 1.4$ to $\mathrm{t} = 1.8\ s$ – SCR $= 1.0$.

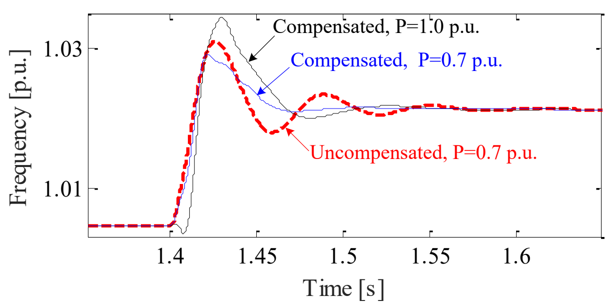

(a)

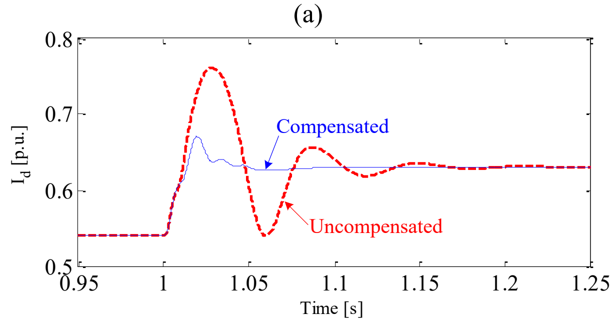

(b)

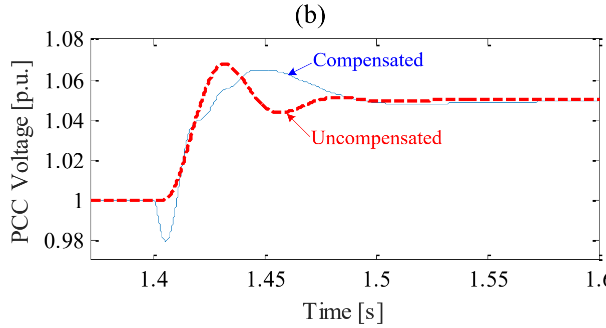

(c)

Figure 5.14 Influence of the proposed compensators on the CSC controllers – $SCR = 1$. (a) PLL response following 1 Hz step in v_g at $t = 1.4$ s. (b) Current response (d-channel) following a step in P from 0.6 to 0.7 p.u. at $t = 1$s. (c) Voltage response following a step in V_d^* from 1.0 to 1.05 p.u. at $t = 1.4$ s.

Chapter 6

Performance Evaluation and Stabilization of Isolated AC Microgrids Supplying Direct Online Induction Motor Loads

This chapter presents detailed small-signal admittance models, analysis and stabilization of a VSC-based microgrid with direct online IM load. Using the generalized Nyquist stability criterion, it is shown that the interactions between the lightly damped dynamics of IMs and isolated VSC-based microgrid have a significant destabilizing effect. Active compensation techniques are proposed to maintain the system stability. Time-domain simulations and experimental results are presented to validate the theoretical analysis.

12.1 Small-Signal Admittance Model of Voltage Source Converters in the Islanded AC Microgrids

Figure 6.1 shows a microgrid system, which is adapted from the IEEE Standard 399 [107]. The microgrid system is composed of three DG units interface by VSCs, a common IM load and a passive load. Figure 6.2(a) shows the power and control structure of a single interfacing VSC. As shown, three control loops are utilized; the power sharing, voltage, and current controllers [89]. The current and voltage dynamics of the power circuits are modeled by (6.1)–(6.4) in the d-q reference frame that rotates synchronously with the angular frequency ω.

$$V_d - V_{od} = \left(R_f + sL_f\right)I_d - \omega L_f I_q \tag{6.1}$$

$$V_q - V_{oq} = \left(R_f + sL_f\right)I_q + \omega L_f I_d \tag{6.2}$$

$$I_d - I_{od} = sC_f V_{od} - \omega C_f V_{oq} \tag{6.3}$$

$$I_q - I_{oq} = sC_f V_{oq} + \omega C_f V_{od} \tag{6.4}$$

where R_f, L_f and C_f are the per-phase resistance, inductance and capacitance of the converter ac LC filter, respectively; $\left(I_d, I_q\right)$, $\left(I_{od}, I_{oq}\right)$, $\left(V_d, V_q\right)$ and $\left(V_{od}, V_{oq}\right)$ are the d-q components of the injected ac current from the VSC (i), the ac load current (i_o), the VSC ac terminal voltage (v) and the ac load voltage (v_o), respectively; s is the Laplace operator.

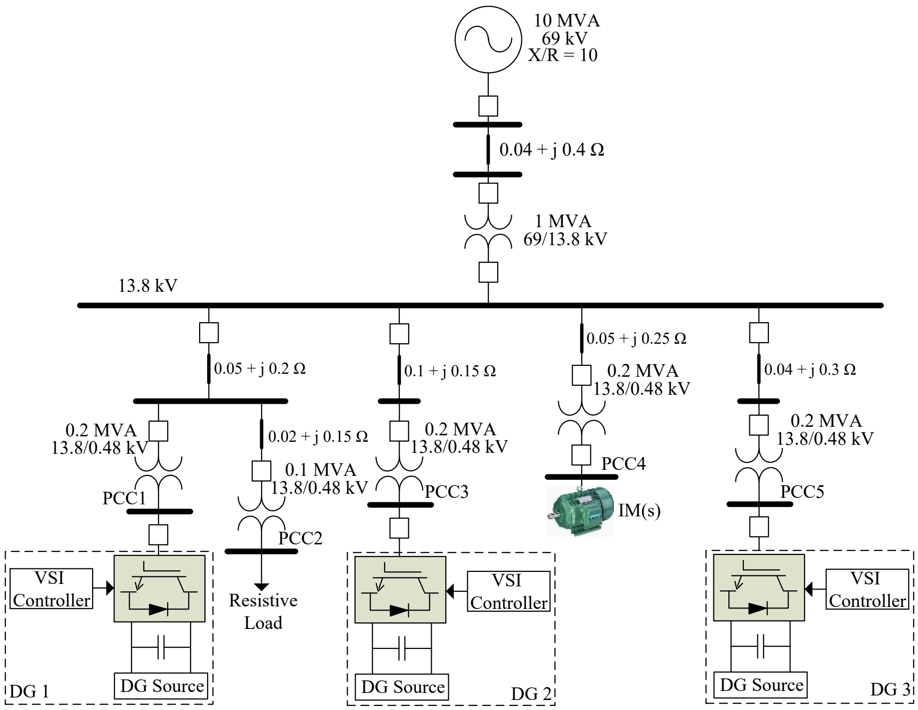

Figure 6.1 The system under study.

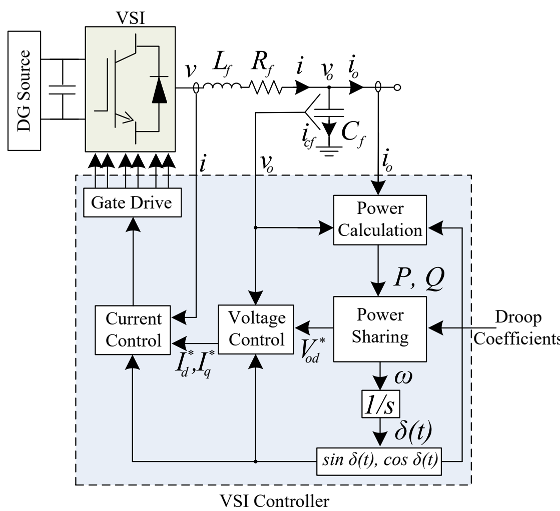

(a)

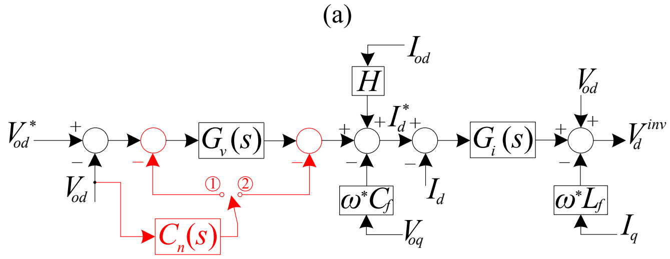

(b)

Figure 6.2 VSCs in the DG systems (a) System structure. (b) Conventional control scheme with the proposed compensators – d-channel only (q-channel is complementary); power sharing loop is not shown.

The dynamics of the current and voltage controllers are as follow [89],

$$V_d^{inv} = (I_d^* - I_d)G_i(s) - \omega^* L_f I_q + V_{od} \tag{6.5}$$

$$V_q^{inv} = \left(I_q^* - I_q\right)G_i(s) + \omega^* L_f I_d + V_{oq} \tag{6.6}$$

$$I_d^* = (V_{od}^* - V_{od})G_v(s) + HI_{od} - \omega^* C_f V_{oq} \tag{6.7}$$

$$I_q^* = \left(V_{oq}^* - V_{oq}\right)G_v(s) + HI_{oq} + \omega^* C_f V_{od} \tag{6.8}$$

where H is a feed-forward gain; $G_v(s)$ and $G_i(s)$ are the PI voltage and current controllers, respectively; V_d^{inv} and V_q^{inv} are the d-q control output applied to pulse-width-modulation (PWM) generator of the VSC, respectively. The superscript "*" represent the reference value of the variable.

The instantaneous active (p) and reactive (q) power delivered to the ac common bus are given by the following.

$$p = 1.5\left(V_{od}I_{od} + V_{oq}I_{oq}\right) \tag{6.9}$$

$$q = 1.5\left(V_{od}I_{oq} - V_{oq}I_{od}\right) \tag{6.10}$$

The average active (P) and reactive (Q) powers that correspond to the fundamental components are obtained by an LPF with a cut-off frequency ω_c to achieve high power quality injection.

$$P = p\frac{\omega_c}{s+\omega_c} = pG_p(s) \tag{6.11}$$

$$Q = q\frac{\omega_c}{s+\omega_c} = qG_q(s) \tag{6.12}$$

To provide a sufficient damping of the low-frequency modes in a microgrid, the following improved droop functions are adopted [89],

$$\omega = \omega^* - mP - m_d\frac{dP}{dt} \tag{6.13}$$

$$V_{od}^{*} = V^{*} - nQ - n_d \frac{dQ}{dt} \tag{6.14}$$

where m and n are the static droop gains of the active and reactive powers, respectively; m_d and n_d are the improved dynamic droop coefficients.

In the microgrid system in Figure 6.1, the rotating reference frame of one VSC is considered as the common frame with respect to the remaining converters. As shown in Figure 6.3, the common d-q reference frame rotates with an angular frequency ω whereas $(d_j - q_j)$ is the arbitrary direct-and-quadrature reference frame for the remaining j^{th} converters and is rotating by ω_j. The angle between the arbitrary and the common reference frames is δ_j.

$$\delta_j = \frac{1}{s}\left(\omega_j - \omega\right) \tag{6.15}$$

6.1.1 Exact Small-Signal Admittance Model of the Voltage-Source Converter

By applying small-signal linearization on (6.1), (6.5) and (6.2), (6.6) and solve together, the resultant two equations are arranged in a matrix form as follows:

$$\begin{bmatrix} \Delta I_d^{*} \\ \Delta I_q^{*} \end{bmatrix} = [C1]\begin{bmatrix} \Delta I_d \\ \Delta I_q \end{bmatrix} + [C2]\begin{bmatrix} \Delta\omega \\ \Delta V_{od}^{*} \end{bmatrix}, \tag{6.16}$$

where Δ represent the small-signal perturbed variable. Similarly, (6.17)- (6.18) are obtained.

$$\begin{bmatrix} \Delta I_d^{*} \\ \Delta I_q^{*} \end{bmatrix} = [V1]\begin{bmatrix} \Delta V_{od} \\ \Delta V_{oq} \end{bmatrix} + [V2]\begin{bmatrix} \Delta I_{od} \\ \Delta I_{oq} \end{bmatrix} + [V3]\begin{bmatrix} \Delta\omega \\ \Delta V_{od}^{*} \end{bmatrix} \tag{6.17}$$

$$\begin{bmatrix} \Delta I_d \\ \Delta I_q \end{bmatrix} = [T1]\begin{bmatrix} \Delta I_{od} \\ \Delta I_{oq} \end{bmatrix} + [T2]\begin{bmatrix} \Delta V_{od} \\ \Delta V_{oq} \end{bmatrix} + [T3]\begin{bmatrix} \Delta\omega \\ \Delta V_{od}^{*} \end{bmatrix} \tag{6.18}$$

Apply small perturbation on the power sharing dynamics in (6.9)–(6.14),

$$\begin{bmatrix} \Delta\omega \\ \Delta V_{od}^{*} \end{bmatrix} = [P1]\begin{bmatrix} \Delta V_{od} \\ \Delta V_{oq} \end{bmatrix} + [P2]\begin{bmatrix} \Delta I_{od} \\ \Delta I_{oq} \end{bmatrix} \tag{6.19}$$

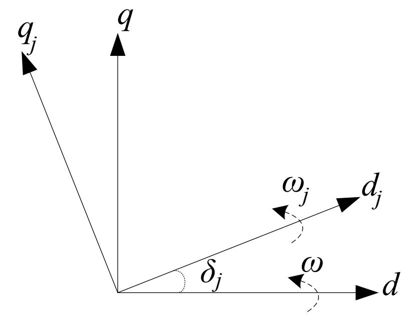

Figure 6.3 Common and arbitrary reference frame transformation.

With some mathematical manipulations, the following equation is obtained,

$$\begin{bmatrix}\Delta I_{od}\\ \Delta I_{oq}\end{bmatrix} = [I_s]^{-1}[V_s]\begin{bmatrix}\Delta V_{od}\\ \Delta V_{oq}\end{bmatrix} = \underbrace{\begin{bmatrix}Y_{sdd}(s) & Y_{sdq}(s)\\ Y_{sqd}(s) & Y_{sqq}(s)\end{bmatrix}}_{[Y_{source}]}\begin{bmatrix}\Delta V_{od}\\ \Delta V_{oq}\end{bmatrix} \tag{6.20}$$

where $[Y_{source}]$ is the output admittance of the VSC in the islanded microgrid mode of operation. The parameters of the preceding equations are all defined in Appendix A6.1.

The source admittance obtained in (6.20) is in the common rotating reference frame. In a similar manner and based on Figure 6.3, the source admittance of the VSC in the arbitrary reference frame for the remaining j^{th} converters is obtained as follows,

$$\begin{bmatrix}\Delta I_{odj}\\ \Delta I_{oqj}\end{bmatrix} = [Y_{source}]\begin{bmatrix}\Delta V_{odj}\\ \Delta V_{oqj}\end{bmatrix}. \tag{6.21}$$

where

$$\begin{bmatrix}\Delta V_{odj}\\ \Delta V_{oqj}\end{bmatrix} = [T_\delta]\begin{bmatrix}\Delta V_{od}\\ \Delta V_{oq}\end{bmatrix} + [T_v][\Delta\delta_j] \tag{6.22}$$

$$\begin{bmatrix}\Delta I_{od}\\ \Delta I_{oq}\end{bmatrix} = [T_\delta]^{-1}\begin{bmatrix}\Delta I_{odj}\\ \Delta I_{oqj}\end{bmatrix} + [T_i][\Delta\delta_j]\,. \tag{6.23}$$

The coefficients of (6.22) and (6.23) are defined in Appendix A6.2. The arbitrary-to-common reference frame source admittance of the VSC is obtained as following.

$$\begin{bmatrix}\Delta I_{od}\\ \Delta I_{oq}\end{bmatrix} = [T_\delta]^{-1}[Y_{source}][T_\delta]\begin{bmatrix}\Delta V_{od}\\ \Delta V_{oq}\end{bmatrix} + ([T_\delta]^{-1}[Y_{source}]_{2\times2}[T_v] + [T_i])[\Delta\delta_j]\,. \tag{6.24}$$

6.1.2 Approximate Small-Signal Admittance Model of the Voltage-Source Converter

A simplified source admittance of the VSC in the isolated mode can be obtained but with the following assumptions:

1- Ignoring the effect of the outer power-sharing loop by setting droop coefficients ($m,\ n,\ m_d, n_d$) to zero. This assumption is accepted due to the sufficient frequency-scale separation between the very slow power- sharing loop and the inner cascaded voltage and current control loops. It is shown in this chapter that the exact and approximate methods are almost equivalent within the medium frequency range.

2- Ignoring the ac capacitor current (i_{cf}) as compared with the injected ac current to the load (i_o) and hence ignoring the coupling terms ($\omega^* C_f V_{oq},\ \omega^* C_f V_{od}$) in (6.7) and (6.8).

By applying these simplifications and following similar procedures, the approximated source admittance of the VSC ($[Y_{source}^{\sim}]$) can be obtained in the form of (6.20) but with zero anti-diagonal elements $\big(Y_{sdq}(s) = Y_{sqd}(s) = 0\big)$ and equal diagonal elements $\Big(Y_{sdd}(s) = Y_{sqq}(s) = Y_s(s)\Big)$. The approximated source admittance is defined in the Appendix A6.3.

$$[Y_{source}^{\sim}] = [I_s^{\sim}]^{-1}[V_s^{\sim}] = \begin{bmatrix}Y_s(s) & 0\\ 0 & Y_s(s)\end{bmatrix} \tag{6.25}$$

12.2 Small-Signal Admittance Model of the Direct Online Induction Motor In the Arbitrary Reference Frame

A symmetrical squirrel cage IM is modeled in arbitrary reference frame as follows [92]:

$$V_{sd} = (R_s + sL_s)I_{sd} - \omega L_s I_{sq} + sL_m I_{rd} - \omega L_m I_{rq} \tag{6.26}$$

$$V_{sq} = \omega L_s I_{sd} + (R_s + sL_s)I_{sq} + \omega L_m I_{rd} + sL_m I_{rq} \tag{6.27}$$

$$0 = sL_m I_{sd} - (\omega - \omega_r)L_m I_{sq} + (R_r + sL_r)I_{rd} - (\omega - \omega_r)L_r I_{rq} \tag{6.28}$$

$$0 = (\omega - \omega_r)L_m I_{sd} + sL_m I_{sq} + (\omega - \omega_r)L_r I_{rd} + (R_r + sL_r)I_{rq} \tag{6.29}$$

$$T_e = \frac{3}{4} P L_m \left(I_{sq} I_{rd} - I_{sd} I_{rq}\right) \tag{6.30}$$

$$\omega_r = \frac{1}{Js}(T_e - T_L)\ . \tag{6.31}$$

The model in (6.26) – (6.31) describes an idealized two-pole IM in the arbitrary reference frame where $\left(V_{sd}, V_{sq}\right)$, $\left(I_{sd}, I_{sq}\right)$, $\left(I_{rd}, I_{rq}\right)$ are the d-q components of the stator ac terminal voltage (v_s), the stator ac current (i_s) and the rotor ac current (i_r), respectively; R_s, R_r are the stator and rotor (referred to stator) resistance, respectively; L_s, L_r, L_m are the stator, rotor and magnetizing inductance, respectively; ω_r, ω are the rotor and arbitrary angular velocity, respectively; P is the number of pole pairs; J is the inertia constant; T_e and T_L are the electromagnetic and load torque, respectively.

Applying small-signal linearization on (6.26) and (6.27),

$$\begin{bmatrix} \Delta V_{sd} \\ \Delta V_{sq} \end{bmatrix} = [S1] \begin{bmatrix} \Delta I_{sd} \\ \Delta I_{sq} \end{bmatrix} + [S2] \begin{bmatrix} \Delta I_{rd} \\ \Delta I_{rq} \end{bmatrix} + [S3][\Delta\omega] \tag{6.32}$$

Similarly, and following some mathematical manipulations,

$$[R1] \begin{bmatrix} \Delta I_{rd} \\ \Delta I_{rq} \end{bmatrix} = [R2] \begin{bmatrix} \Delta I_{sd} \\ \Delta I_{sq} \end{bmatrix} + [R3][\Delta\omega] + [R4][\Delta\omega_r] \tag{5.33}$$

$$[\Delta\omega_r] = [M1] \begin{bmatrix} \Delta I_{sd} \\ \Delta I_{sq} \end{bmatrix} + [M2] \begin{bmatrix} \Delta I_{rd} \\ \Delta I_{rq} \end{bmatrix} + [M3][\Delta T_L] \tag{5.34}$$

$$\begin{aligned} \begin{bmatrix} \Delta V_{sd} \\ \Delta V_{sq} \end{bmatrix} = &\left\{ \begin{matrix} [S1] + [S2]([R1] - [R4][M2])^{-1} \\ \times ([R2] + [R4][M1]) \end{matrix} \right\} \begin{bmatrix} \Delta I_{sd} \\ \Delta I_{sq} \end{bmatrix} \\ &+ \{[S2]([R1] - [R4][M2])^{-1}[R3] + [S3]\}[\Delta\omega] \\ &+ [S2]([R1] - [R4][M2])^{-1}[R4][M3][\Delta T_L] \end{aligned} \tag{6.35}$$

The first term in (6.35) in the input impedance of the IM and is expressed as shwon in (6.36). The parameters of (6.35) are defined in Appendix A6.4.

$$[Y_{load}]_{2\times 2} = \begin{bmatrix} Y_{ldd}(s) & Y_{ldq}(s) \\ Y_{lqd}(s) & Y_{lqq}(s) \end{bmatrix} \tag{6.36}$$

12.3 Analysis of the Small-Signal Source and Load Admittance

6.3.1 Voltage-Source Converter

Using (6.20), the four-channel source admittance of the VSC is plotted as shown in Figure 6.4. It is noted that $Y_{sdd}(s)$ is equal to $Y_{sqq}(s)$. The droop coefficients reshape the real part of the source admittance in the very low-frequency range for the diagonal elements as shown in Figure 6.4(b). In general, the power sharing loop is designed with an LPF with low cut-off frequency (in the range of few Hz); therefore, the influence of the droop coefficients appears within this low-frequency range [89].

6.3.2 Direct Online Induction Motor

The frequency response of the IM admittance in (6.36) is shown in Figure 6.5 for two IMs rated at 50 and 200 hP. The four channel input admittance of the IM has two magnitude peaks; one around 30 Hz and the other around 60 Hz at rated speed [solid curves]. The 30 Hz peak corresponds to the rotor dynamics as it is sensitive to the rotor speed whereas the 60 Hz peak corresponds to stator dynamics (supply frequency). Comparing the high- and low-power IMs in Figure 6.5, the magnitude of the input admittance is reduced by 10 dB in the 50 hP IM as compared to the 200 hP. Based on the Nyquist stability criterion, as the load admittance decreases, the stability margin increases [43]. Therefore, the 50 hP IM has a higher stability margin than the 200 hP motor.

A small-signal state-space model of the IM is developed as shown in Appendix A6.5. Using the same parameters of both 50 and 200 hP IMs, the eigenvalues are depicted in Table 6.1. At the rated speed there are; two conjugate poles close to the supply frequency and are primarily associated with the stator dynamics, and two conjugate poles close to 30 Hz and are associated with the rotor dynamics, and a lightly-damped real pole which is mainly related to the mechanical dynamics [92]. Table 6.1 also shows that 50 hP IM has larger real part magnitude than the 200 hP implying higher damping.

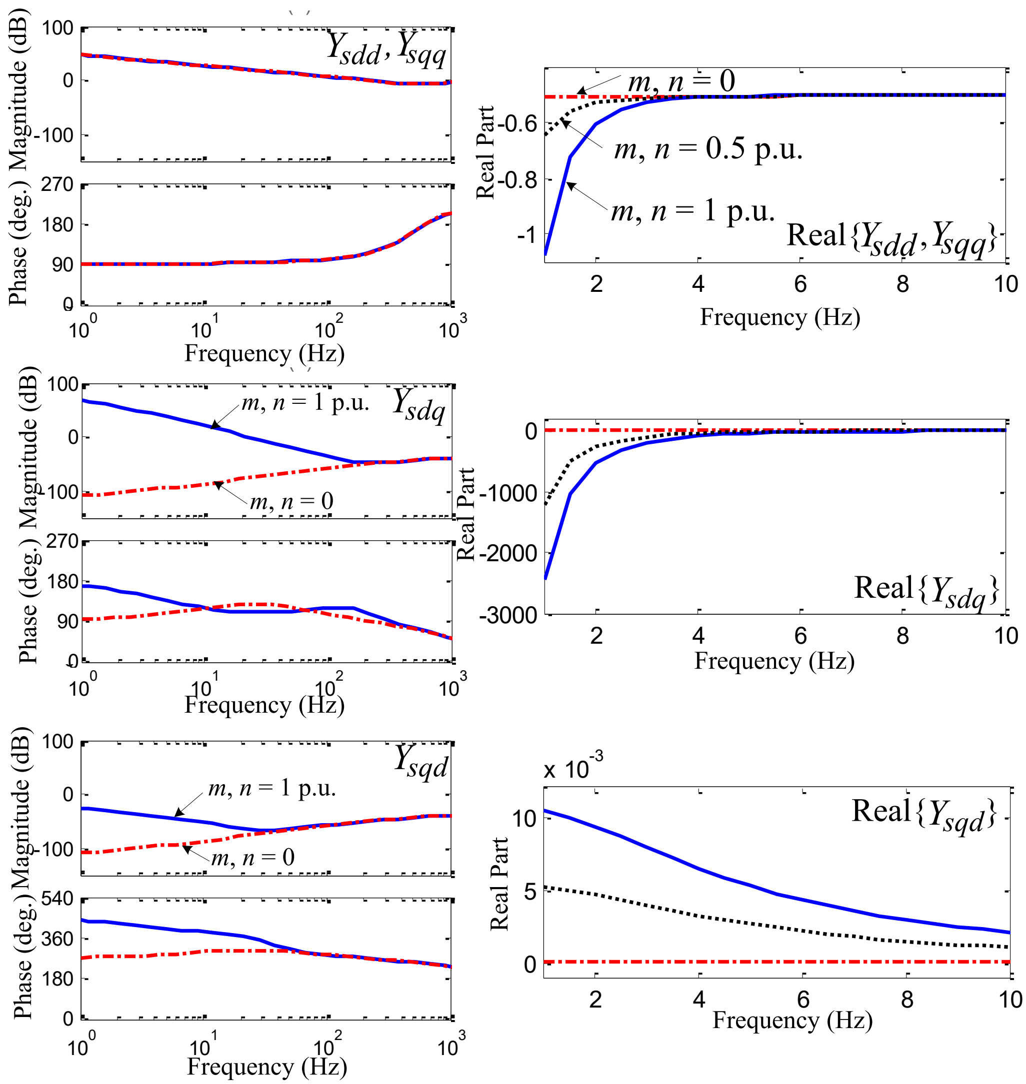

(a) (b)

Figure 6.4 Small-signal source admittance of the VSC with/without droop coefficients. (a) Frequency response. (b) Real part.

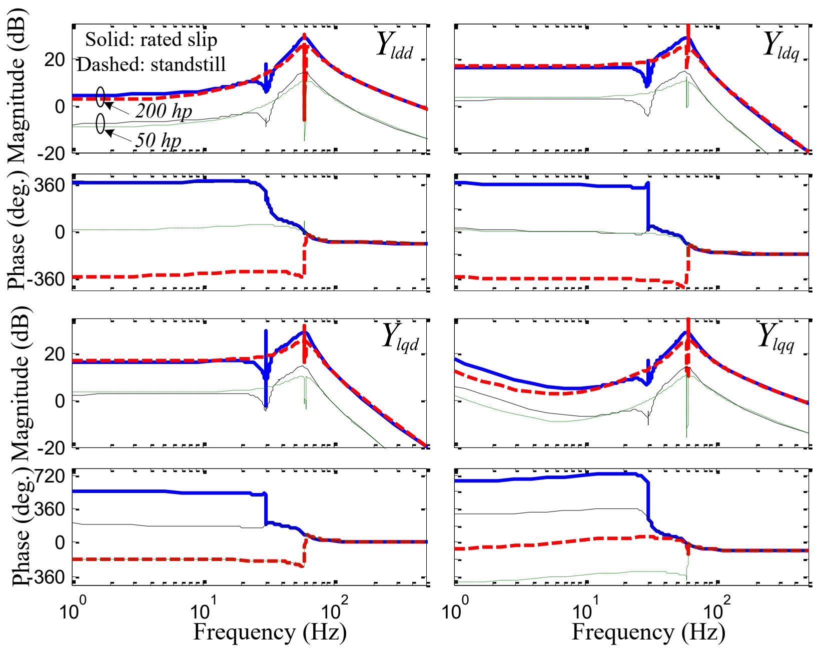

Figure 6.5 Small-signal load admittance of the direct online 200 and 50 hP IM at standstill and rated speed.

Table 6.1 Eigenvalues of the Induction Motor

hP	Rated Speed		Standstill	
200	Stator:	$-49.47 \pm j\,367.25$	Stator:	$-84.42 \pm j\,378.64$
	Rotor:	$-34.97 \pm j\,203.23$	Rotor:	$-0.83 \pm j\,377.01$
	Mechanical:	-2.55	Mechanical:	-0.92
50	Stator:	$-60 \pm j\,362.33$	Stator:	$-102.5 \pm j\,378.46$
	Rotor:	$-43.1 \pm j\,207.75$	Rotor:	$-1.43 \pm j\,377.02$
	Mechanical:	-2.77	Mechanical:	-1.01

12.4 Admittance-Based Stability Analysis

6.4.1 Approximated-Voltage-Source Converter-Model-Based Analysis

From the approximate source admittance of VSC in (6.25), the approximated source impedance can be obtained in the following, where $Z_s(s) = 1/Y_s(s)$:

$$[Z_{source}^{\sim}]_{2\times2} = [Y_{source}^{\sim}]_{2\times2}^{-1} = \begin{bmatrix} Z_s(s) & 0 \\ 0 & Z_s(s) \end{bmatrix}. \quad (6.37)$$

Using (6.37) and the load admittance of the IM in (6.36), the Nyquist matrix ratio is yielded as follows [96]:

$$[Y_{load}][Z_{source}] = \begin{bmatrix} Y_{ldd}(s)Z_s(s) & Y_{ldq}(s)Z_s(s) \\ Y_{lqd}(s)Z_s(s) & Y_{lqq}(s)Z_s(s) \end{bmatrix} \quad (6.38)$$

The matrix impedance ratio can be decomposed into equivalent four SISO subsystems and the corresponding Nyquist plots are shown in Figure 6.6. The analysis is based on one 200 hP IM as a common load in the isolated microgrid. The effect of adding an additional VSC unit in parallel to the original three units is also shown on the same figure. The added VSC positively affect the system stability by reducing the equivalent source impedance.

The first subsystem in Figure 6.6 is represented by a Bode plot in Figure 6.7. As shown, with the three-VSC case, there are two points of interaction between $Z_s(s)$ and $Y_{ldd}^{-1}(s)$ at A1 and A2. For the four VSCs case, the intersections occur at B1 and B2. Note that both A1 and B1 are stable with sufficient phase margin of 159.4° and 138.6°, respectively. However, the stability margin at the point A2 is -3° implying the unstable response. With the four-VSCs micro-grid, the phase margin of the point B2 is increased to 9° resulting in a lightly damped stable response [as concluded from Figure 6.6].

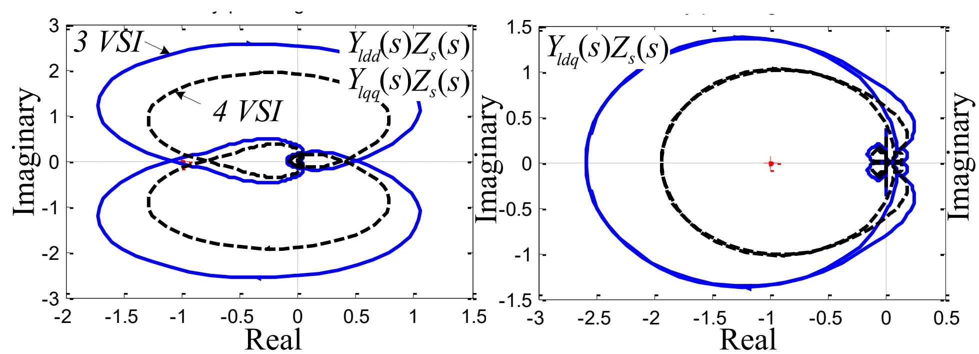

Figure 6.6 Nyquist stability criterion for the approximated source impedance of the VSC and the IM – Influence of the parallel connection of VSC units.

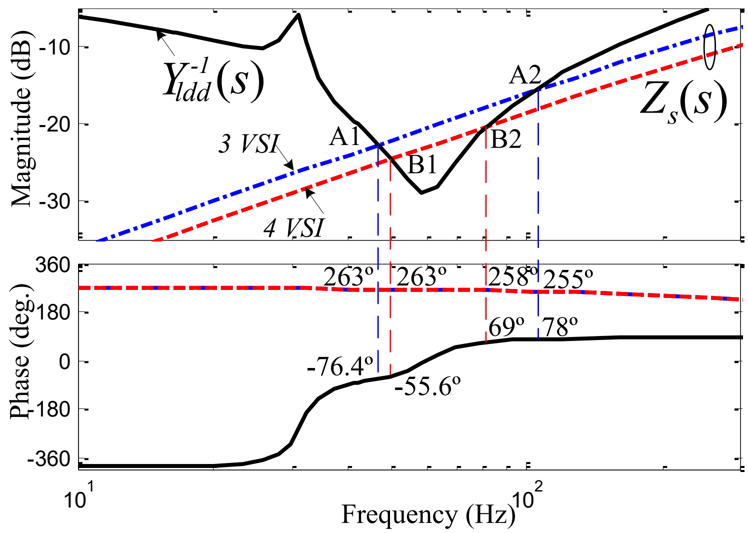

Figure 6.7 Nyquist stability criterion for the subsystem $Y_{load}(s)Z_{source}(s)$ in Figure 6.6.

6.4.2 Exact-Voltage-Source Converter-Model-Based Analysis

The preceding analysis is restricted to the condition of zero anti-diagonal (or diagonal) elements in the source (or load) impedance matrices. Otherwise, the exact model-based analysis should be followed. According to (6.39), the magnitudes of all eigenvalues (λ_i) of any square matrix M is bounded by the maximum ($\overline{\sigma}(M)$) and minimum ($\underline{\sigma}(M)$) singular values of the matrix M, respectively.

$$\underline{\sigma}(M) \leq |\lambda_i(M)| \leq \overline{\sigma}(M) \tag{6.39}$$

Therefore, a matrix norm of the ratio $Y_{load}(s)Z_{source}(s)$ that includes the maximum eigenvalues can be defined for MIMO systems and should be limited to be less than one so that no eigenvalue plot would encircle the $-1 + j0$ point [108]-[109]. This can be mathematically described by (6.40).

$$\overline{\sigma}(Z_{source}) < \underline{\sigma}(Z_{load}) \tag{6.40}$$

For MIMO systems with 2×2 source-load impedance/admittance matrices, the system stability is guaranteed around the point of connection if the maximum singular value of the source impedance is less than the minimum singular value of the load impedance.

Figure 6.8 shows the source-load interactions based on (6.40). It is shown that the interaction between the source and load might yield instabilities due to the unsatisfied condition in (6.40). Instabilities occur in a relatively wide frequency range (e.g., 30 Hz to 300Hz as shown in Figure 6.8).

To investigate the accuracy of the approximated source impedance of the VSC, the maximum singular value of both exact and approximated models have been obtained as shown in Figure 6.8. The approximated and exact impedance have similar responses starting from low frequencies (~10 Hz). However, at very low frequencies, below 10 Hz, there is a significant difference between the two impedances. Figure 6.8 also shows the exact impedance with different values of the LPF cut-off frequency (ω_c) in the power-sharing loop. As ω_c decreases from 1.0 p.u. to 0.25 p.u., the response of the source impedance changes in the very low frequency region.

In the small-signal sense, it is clear that IM loads induce resonant peaks in the motor admittance [around 30 and 60 Hz in Figure 6.5] which can violate the stable admittance ratio criterion between the load-side (IM) and equivalent source-side (VSC), particularly in the isolated mode of operation. Due to the weak nature of the equivalent source admittance in isolated microgrids and the close regulation characteristics of VSCs, instabilities are yielded. On the contrary, when a microgrid system is connected to a strong utility-grid, the overall source impedance will be small and, therefore, the source-load impedance interactions will be minimal. These interactions occur directly between an IM load and voltage-controlled VSCs with minimum coupling from the power-sharing controller (e.g., droop control) due to the frequency-scale separation between the voltage control dynamics and the low-bandwidth power sharing loops. It should be noted that using the control parameters of the VSC to avoid possible interaction dynamics (e.g., voltage control bandwidth) yields very limited shaping capability and directly affects the closed-loop performance. Therefore, there is a strong need to develop a second-degree-of-freedom active controller that reshapes the source admittance of the VSC locally at the instability-related frequency-range without affecting the overall closed-loop frequency response characteristics.

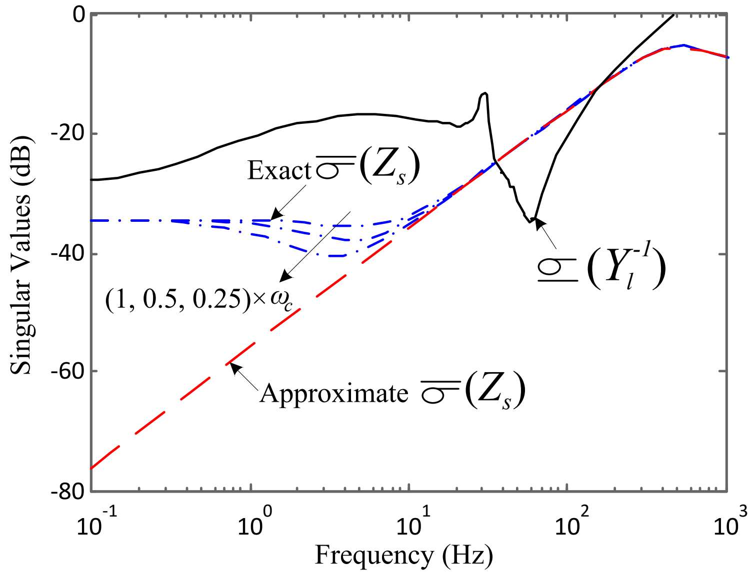

Figure 6.8 The approximated and exact source impedance of the VSC.

12.5 Active Stabilization of the Isolated AC Microgrids with High Penetration of Induction Motor Loads

Figure 6.2(b) shows the control structure of the VSI in the isolated microgrid systems with the proposed active damping controllers. The proposed compensation technique depends on feeding the *d-q* ac bus voltage into a compensator function ($C_n(s)$) and injecting the generated output into two possible points in the control structure of the VSC; the first and second injection points correspond to the voltage- and current-reference-based (VRC, CRB) compensators, respectively.

The compensation function is selected to have BPF characteristics so that the source impedance is only reshaped around the required frequency band without causing a deformation in other frequency ranges. The compensation function is given in the form of (6.41),

$$C_n(s) = K_n \frac{2\xi_n \omega_n s}{s^2 + 2\xi_n \omega_n s + \omega_n^2} \tag{6.41}$$

where K_n is the compensator gain; ξ_n is the damping ratio; ω_n is the operating frequency of the BPF and the subscript n equals 1 or 2 according to the activated compensation loop. An LPF can be also used instead of BPF in (6.41).

By considering the proposed compensator and following similar procedures to get (6.20), the compensated source admittance of the VSC is given as following, and is defined in Appendix A6.6.

$$\begin{bmatrix}\Delta I_{od}\\ \Delta I_{oq}\end{bmatrix} = \left[I_s^{comp}\right]^{-1}\left[V_s^{comp}\right]\begin{bmatrix}\Delta V_{od}\\ \Delta V_{oq}\end{bmatrix} = \underbrace{\begin{bmatrix}Y_{sdd}^{comp}(s) & Y_{sdq}^{comp}(s)\\ Y_{sqd}^{comp}(s) & Y_{sqq}^{comp}(s)\end{bmatrix}}_{\left[Y_{source}^{comp}\right]}\begin{bmatrix}\Delta V_{od}\\ \Delta V_{oq}\end{bmatrix} \tag{6.42}$$

6.5.1 Damping Capabilities

Figure 6.9(a) shows the effect of the VRB compensator ($C_1(s)$) on the Nyquist stability criterion. The operating frequency (ω_1) of the BPF is selected to be 377 rad/s so that the source impedance of the VSC is actively reshaped around the frequency of the lightly damped eigenvalues. The damping ratio (ξ_1) is selected to equal 0.2. As the compensator gain (K_1) increases from 10 to 12, a higher stability margin is added to the system. When ξ_1 is increased to 0.8, the system stability is still maintained but with considerable deformation in the source impedance. In a similar trend, the BPF-based compensator is replaced by an LPF operating at a lower cut-off frequency (0.5×377 rad/s). The system stability is obviously maintained but with a considerably high deformation in the low-frequency region of the source impedance of VSC.

The CRB compensator ($C_2(s)$) is also investigated as shown in Figure 6.9(b). With a damping ratio (ξ_2) equals 0.2 and a compensator gain (K_2) equals 10, the intersection around the 60 Hz region is completely avoided. However, the stability margin is reduced in the very low frequency (around 20 Hz). The source impedance can be improved by increasing the value of the damping ratio to be 0.8 so that the width of activity of the BPF compensator increases. As shown, with $\xi_2 = 0.8$ and with the increase of the compensator gain from 10 to 12, the system stability is satisfied but with significant deformation in the source impedance that would affect the behavior of the VSC. The behavior of the LPF-based compensator is also shown in Figure 6.9(b) and can provide sufficient stability margin.

The influence of the proposed VRB compensator on $Real\{Y_{sdd}(j\omega)\}$ is shown in Figure 6.10(a). With the BPF-based compensator, the magnitude of the negative admittance in the low-frequency range is significantly increased in the range up to 60 Hz and then the real part becomes positive up to 300 Hz. This shows that the proposed compensator increases the damping of the source admittance as seen from the IM side. Figure 6.10(a) shows the effect of the LPF-based compensator which actively shifts the real part to be positive up to 600 Hz. In Figure 6.10(b), $Real\{Y_{sdd}(j\omega)\}$ is negative in the low-mid frequency range of 30-420 Hz with the BPF-CRB compensator.

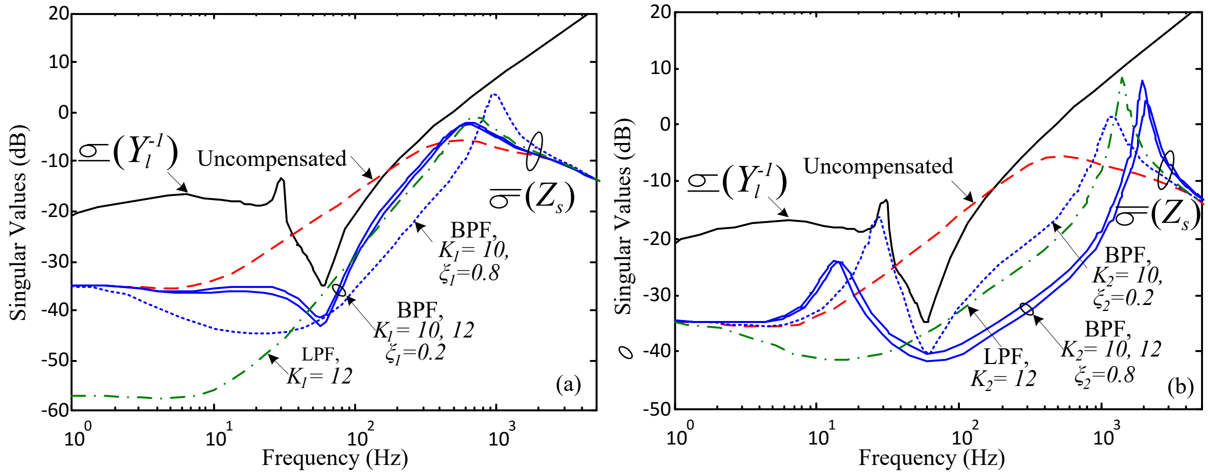

(a) (b)

Figure 6.9 Exact model-based Nyquist stability criterion with the proposed compensators. (a) voltage-reference-based. (b) current-reference-based.

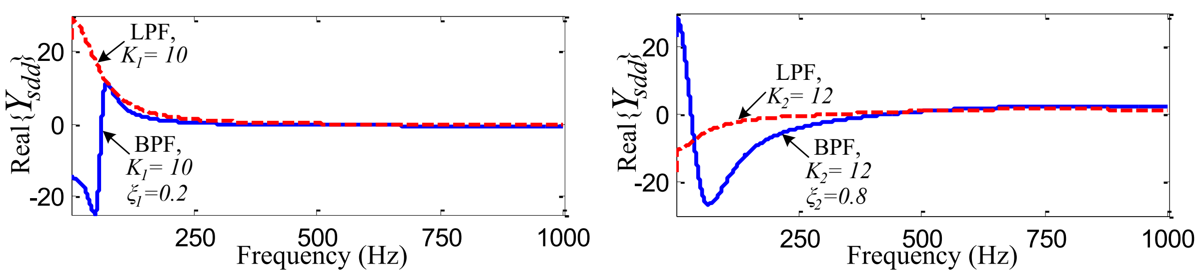

(a) (b)

Figure 6.10 Real part of the actively compensated source Admittance of VSC – $Real\{Y_{sdd}(j\omega)\}$. (a) voltage-reference-based. (b) current-reference-based.

6.5.2 Influence of the Proposed Compensators on the Tracking of the AC Voltage Controller

From Figure 6.2, and using the block diagram reduction rules, the transfer function that describes the ac voltage controller dynamics is given by (6.43) in which only one compensator is activated.

$$\frac{V_{od}}{V_{od}^*} = \frac{G_v(s)G_i(s)}{sC_f\left(G_i(s)+R_f+sL_f\right)+1+G_v(s)G_i(s)\left[1-C_1(s)-\frac{C_2(s)}{G_v(s)}\right]} \tag{6.43}$$

Figure 6.11 shows the frequency response of (6.43). For the uncompensated system, the voltage controller bandwidth is selected to be around 300 Hz. Figure 6.11(a) addresses the effect of using BPF-based compensator as compared to the uncompensated case. The compensators parameters are equal for a fair comparison. It is obvious that the VRB compensator has minimal effect on the ac voltage tracking as compared to the CRB. Figure 6.11(b) shows the influence of the LPF-based compensators on the voltage controller dynamics. Higher frequency range is affected as compared to the BPF-based compensators.

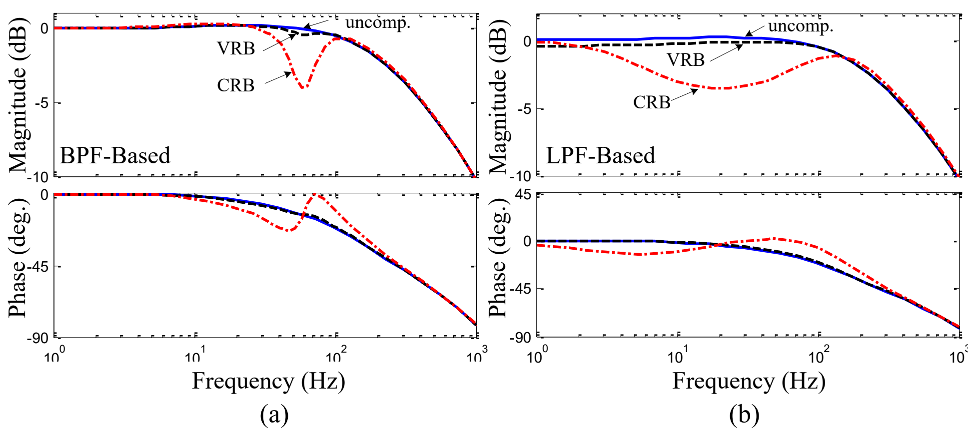

Figure 6.11 AC voltage controller tracking for the VRB and CRB compensated VSC. (a) Using the BPF. (b) Using the LPF.

12.6 Simulation Results

A 450 kVA isolated microgrid model is built under Matlab/Simulink® environment to evaluate the preceding theoretical analysis and validate the efficiency of the proposed compensators. The microgrid model is similar to that shown in Figure 6.1. The common load in the microgrid system is a 200 hP direct online IM rated at 460 Vac and 1785 rpm. A pure resistive load rated at 15kW (20 hP) is placed in parallel with the IM. Three 150 kVA DG units are considered in the model with the circuit structure and control topology as shown in Figure 6.2. The complete model entities are built using SimPowerSystem® toolbox. The VSCs are simulated using average-model-based blocks. The simulation type is discrete with a sample time of 50μs. The system parameters are given in the Appendix A6.7.

6.6.1 Operation of the Induction Motor in the Uncompensated Islanded AC Microgrid

The same control structure in Figure 6.2 is adopted for the ac microgrid but without the proposed active compensation loops. The free acceleration performance of the 200 hP IM under these conditions is shown in Figure 6.12(a). The response of the starting periods [up to 0.6 s] is relatively stable. At $t = 0.6$ s, the dynamics of IM successfully approach the steady state operating points. However, the system response is completely unstable after t = 0.6 s. The electromagnetic torque builds up and the motor speed decays to zero in a building-up manner. The simulation results in Figure 6.12(a) successfully validate the analytical findings in Figures 6.6 and 6.8. Figure 6.12(b) shows the same results but with the 50 hP IM. The system starts up successfully, and the steady-state operating point is reached. However, at t = 2.2 s, the system damping is degraded and the overall stability as completely violated.

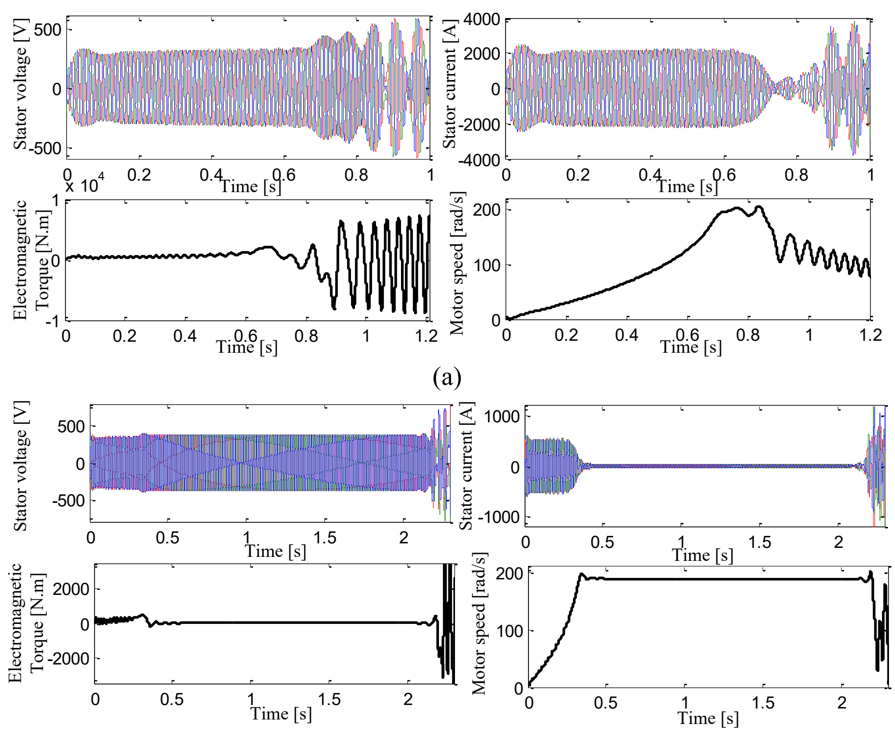

Figure 6.12 Free acceleration response of the IM supplied from the uncompensated isolated microgrid. (a) 200 hP IM. (b) 50 hP IM.

6.6.2 Operation of the Induction Motor in the Compensated Islanded AC Microgrid

Figure 6.13 shows the performance of the IM when supplied from the VRB-compensated isolated microgrid grid. As shown in Figure 6.13(a), the IM is loaded by 0.5 p.u. and 1.0 p.u. mechanical loads at t = 3 and 4.5 s, respectively. The proposed active compensator provides a highly damped performance in both cases. Even the start-up response is highly damped as compared to the uncompensated case in Figure 6.12(a). The well-damped electromagnetic torque in Figure 6.13(a) is reflected to the speed response. Figure 6.13(b) shows the voltages and currents responses of the IM stator.

The performance of an individual DG unit is investigated as shown in Figures 6.13(c)-6.13(d). The Local voltage and injected currents are highly damped. There is a slight steady-state reduction in the local frequency at both step loading instants by 0.3 and 0.5 rad/s whereas the magnitudes of the transient anti-peaks of the frequency response in both instants are 372.5 and 372.3 rad/s. It is clear that the proposed active compensator in the isolated microgrids provides sufficient damping capabilities.

Figure 6.14 shows the performance of one DG unit when the proposed compensator is tuned under two parameter sets that correspond to a high- and a low-damped performance. In both cases, the improved droop controllers in (6.13)-(6.14) are used. A large-signal step loading of 1.0 p.u. is applied at $t = 2s$. The influence of the high- and low-damped performance of the proposed compensator on the injected active power and local frequency is shown in Figures 6.14(a)-6.14(b), respectively. The lower-damped performance has low-frequency oscillations (in the range of few Hz) in both injected active power and local frequency which are mainly attributed to the electromechanical oscillation of the IM load that are reflected to the droop-based power-sharing scheme. However, as the compensator gain increases, these low-frequency oscillations are well-damped, which indicates that the proposed compensator has a suppressive influence on the oscillations of the injected active power and local frequency of the individual DG units.

It is worth mentioning that the simulation results in Figure 6.14 have been observed following different variations in the value of the ac-side capacitors from 1 p.u. to 2, 4, and 6 p.u. In all cases, the influence of the variation of the system capacitance is very minimal on harmonics of the input stator current and the steady-state performance. Moreover, the proposed compensators (with the same tuned parameters) provide similar damping capabilities in all cases.

A SLG fault is applied at t=4 s at the terminals of one DG units, and is cleared after 3 cycles. The compensated system performance is shown in Figure 6.15. The injected stator current is well-damped. The damped performance is reflected on the mechanical motor speed. The proposed compensator positively contributes to the fault ride through capabilities of the power converter.

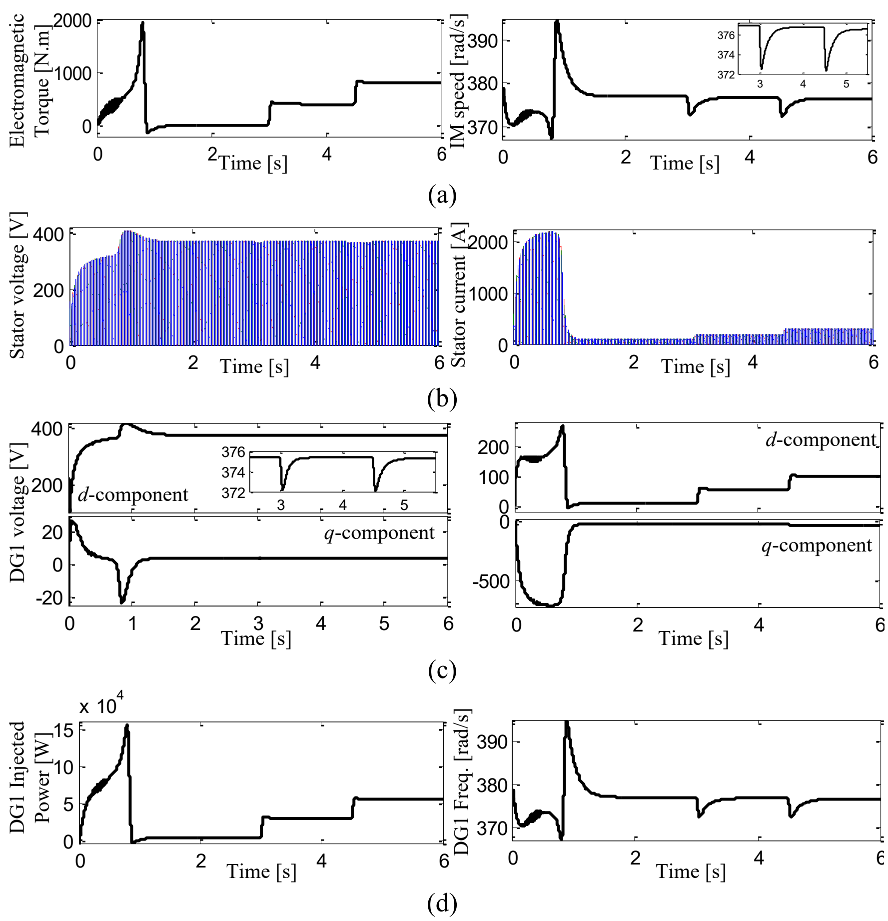

Figure 6.13 Actively VRB-compensated performance of the isolated microgrid-IM system (200 hP IM).

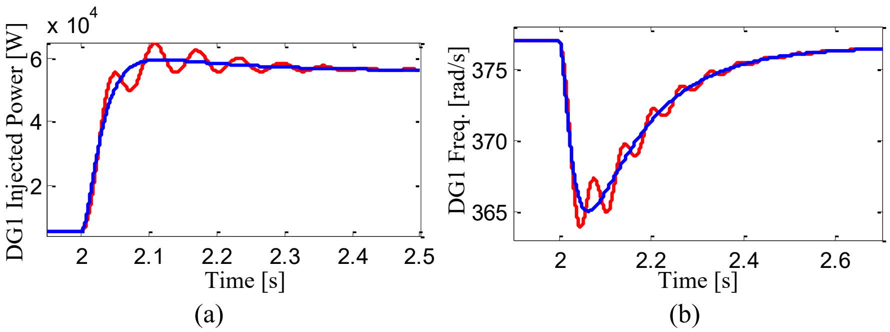

Figure 6.14 Influence of the proposed VRB compensator on the suppression of frequency and injected power oscillations.

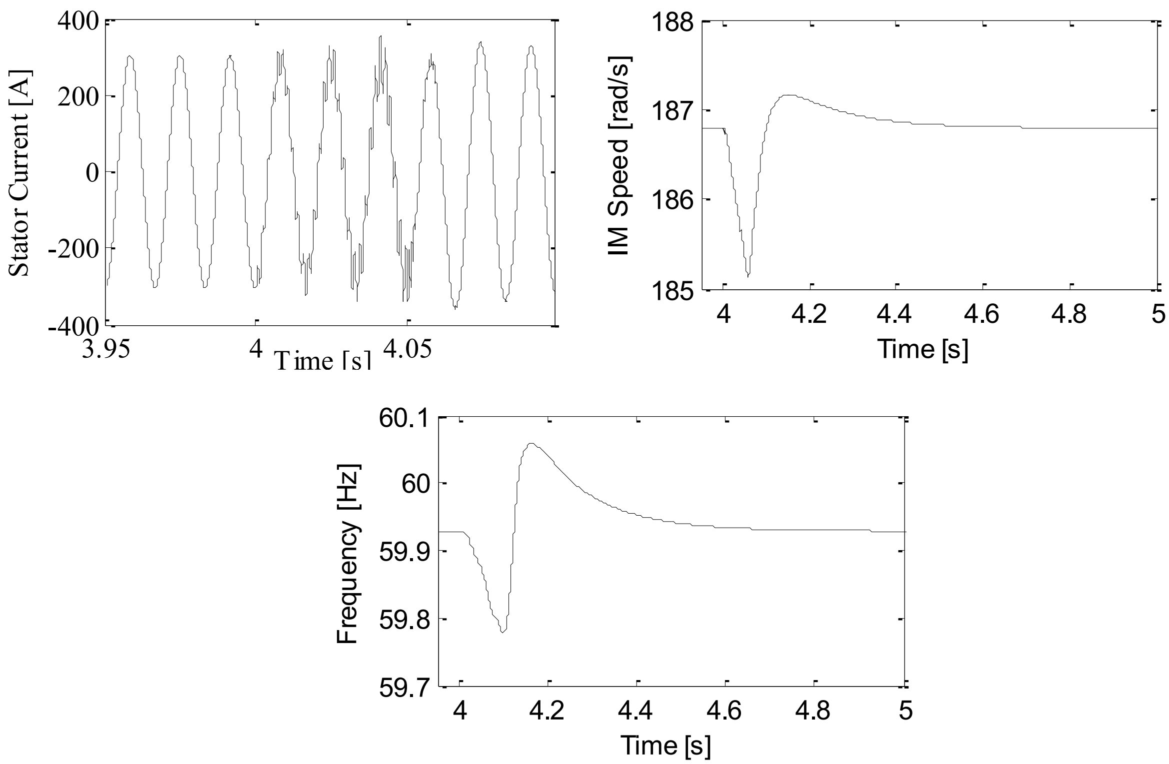

Figure 6.15 Performance of the compensated IM system following a SLG fault at the terminals of one DG units – fault is applied at $t = 4\ s$ and is cleared after 3 cycles.

6.7 Experimental Results

A 1.0 kVA laboratory-scale microgrid setup, as shown in Figure 6.16, is implemented. The experimental system parameters are given in Appendix A6.7.

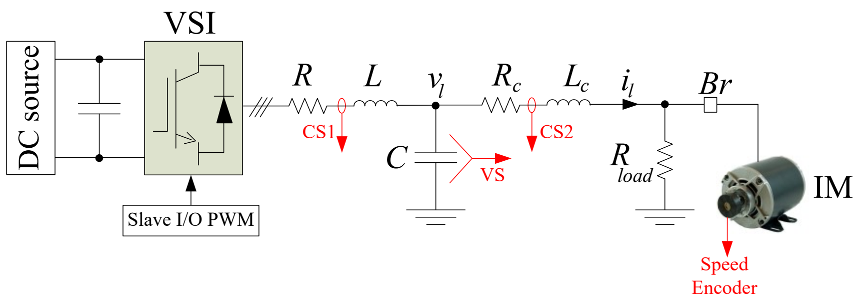

(a)

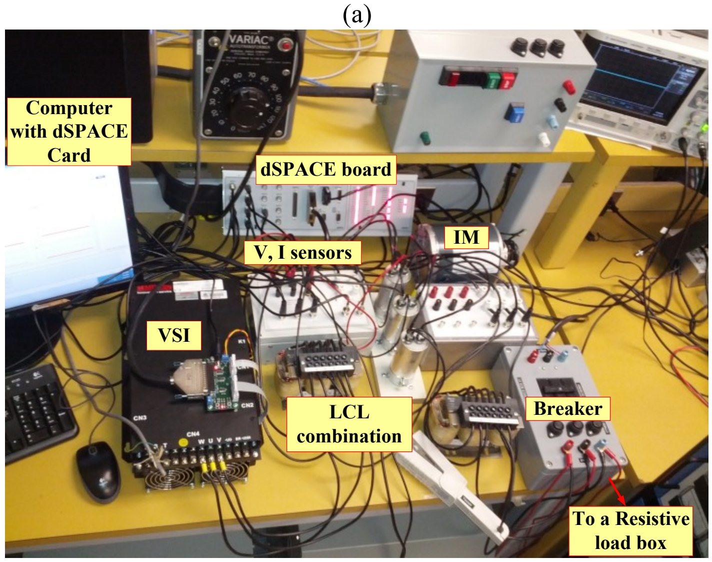

(b)

Figure 6.16 Laboratory verification. (a) Schematic diagram. (b) Hardware setup.

A Semistack intelligent power module, which includes gate drives, six IGBTs, and protection circuit is used as a VSC. The switching frequency is 10 kHz, which indicates that the proposed compensator can be effectively implemented under high sampling frequency. The inverter- and load-side inductor currents are measured by HASS-50-S current sensors (CS1, CS2) whereas the output ac voltage signal is measured by LEM-V-25-400 voltage sensors (VS). A QD200 speed encoder with a resolution of 2048 lines and a quadrature output of 5V-RS422A-Line-Driver is used to measure the IM speed.

The VSC control scheme, d-q orientation and the PWM generation are implemented on the dSPACE1104 control card supported with a TMS320F240-DSP coprocessor structure for PWM generation. The dSPACE1104 interfacing board is equipped with eight digital-to-analogue channels (DAC) and eight analogue-to-digital channels (ADC) to interface the measured signals to/from the control system. The software code is generated by the Real-Time-WorkShop in the Matlab/Simulink® environment.

6.7.1 Uncompensated System Performance – Starting of the Induction Motor

The system in Figure 6.16 is initially started on the 250 W resistive load. At steady-state conditions, the IM is started by closing the breaker (Br) at $t = t_o$. Before $t = t_o$, both voltage (v_l) and current (i_l) are stable [Figure 6.17]. However, the voltage and current signals continue for almost two cycles before the protection of the VSC system trips. It is noted that the voltage signal is superimposed by relatively high order harmonics. The frequency of these harmonics is around 4-6 times of the power frequency which lies in the mid-frequency region (between the power frequency and current control bandwidth). These kinds of oscillations are due to the Nyquist criterion mismatch, which usually occur in the medium-frequency range [Figure 6.8]. Figure 6.17(b) shows the corresponding ac current with a similar trend. The highest voltage and current peaks/dips are 1.275 p.u. and 1.1 p.u., respectively (circled in Figure 6.17).

6.7.2 Uncompensated System Performance – Switching-on a Resistive Load

The system starts on the 250 W resistive load. Instead of starting the IM at $t = t_o$, a 500 W (0.67 hP) resistive load is switched on. The system response is shown in Figure 6.18. Although the additional resistive load is higher than the IM load, the system response is well-damped without any significant oscillations. This implies that the interaction dynamics problem is mainly attributed to the input/output impedance mismatch due to the nature of the IM load.

6.7.3 Active Compensated System – Starting of the Induction Motor

The proposed VRB compensator is employed in the control structure of the VSC. The system is started on the 250 W resistive load, and the IM is switched-on at $t = t_o$. The system response is shown in Figure 6.19 with a highly damped performance. Figure 6.19(a) shows the voltage waveform before and after starting the IM. There is a negligible voltage dip of 0.075 p.u. after starting the IM that recovers quickly. The load current is shown in Figure 6.19(b). As shown in Figure 6.19(c), the maximum value of the IM inrush current is 0.91 p.u, as compared to 1.1 p.u. in the uncompensated case. The speed response is shown in Figure 6.19(d) with a well-damped response. The steady-state voltage and current signals are shown in Figure 6.19(e).

6.8 Conclusions

This chapter has introduced the modeling, analysis and stabilization of the isolated ac microgrids with the high penetration of direct online IM loads. Using the generalized Nyquist stability criterion, it has been shown that IMs load can significantly affect the stability of an isolated microgrid system. Proposed active compensation techniques from the VSC side are introduced to maintain the system stability. The proposed compensators have the following features. 1) They are designed and modeled using linear analysis tools which implies their simplicity. 2) They are efficient and satisfy the Nyquist criterion under large-signal disturbances (such as 1.0 p.u. instant loading). 3) They have a positive influence on the power-frequency oscillations of the individual DG units in isolated microgrids. 4) The "plug-and-play" feature of the future microgrids can be easily achieved with harsh dynamic loads, such as IMs.

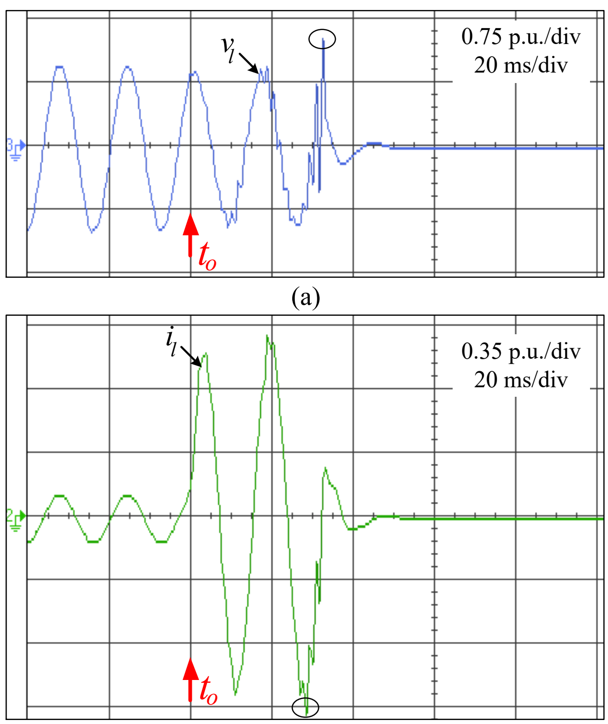

(b)

Figure 6.17 Uncompensated system response – Switching-on IM at t_o. (a) Terminal phase voltage. (b) Injected load current.

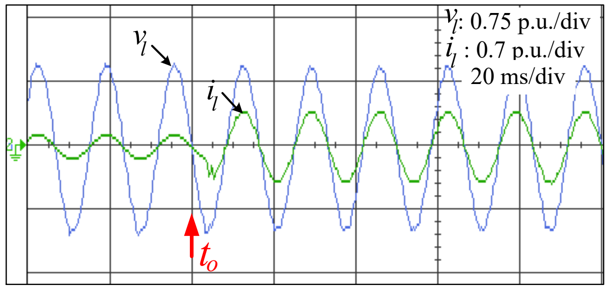

Figure 6.18 Uncompensated response – Switching-on additional resistive load at t_o.

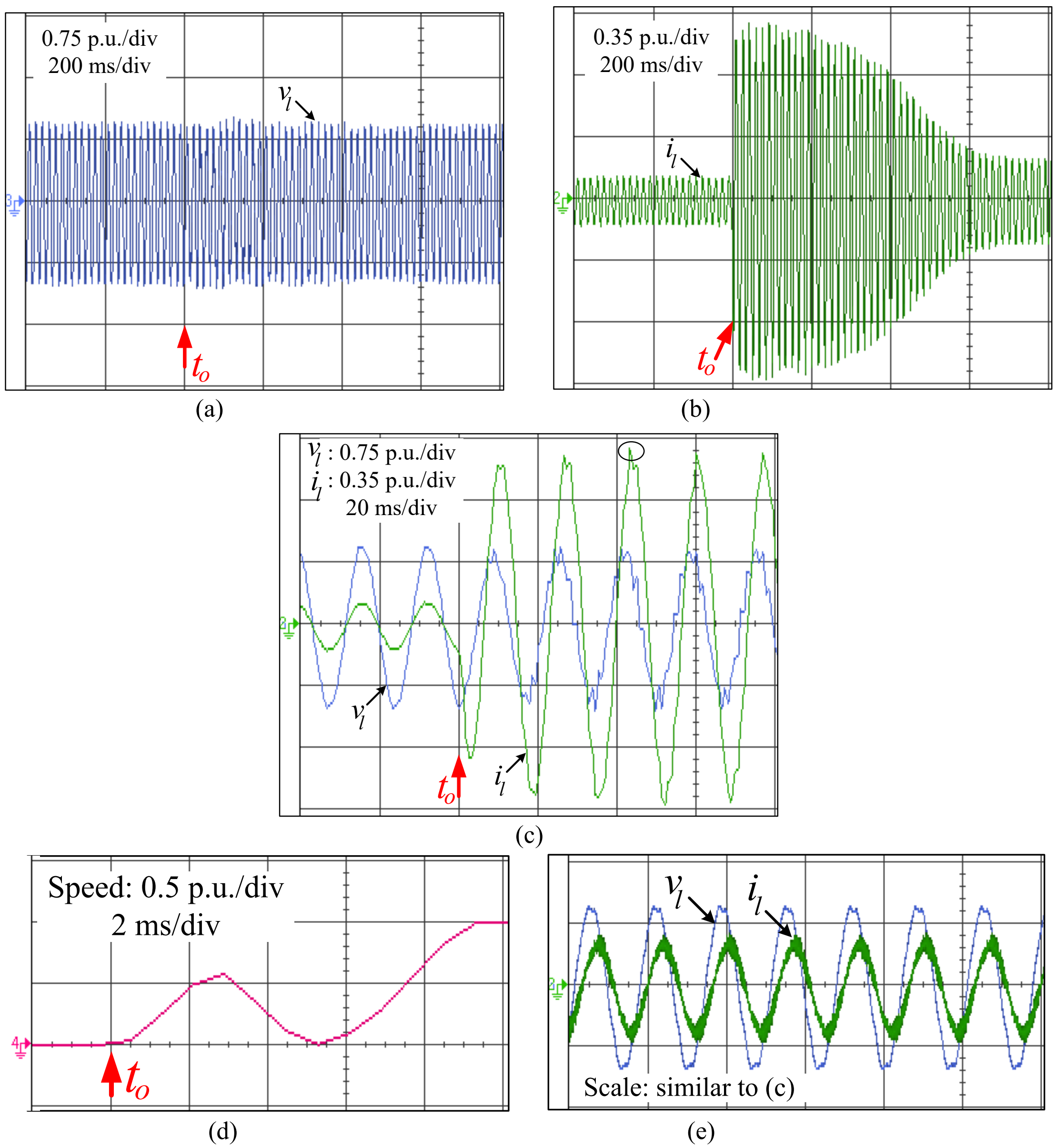

Figure 6.19 Active compensated system – Switching-on IM at t_o. (a) Phase voltage. (b) Total load current. (c) Phase voltage and load current – starting period. (d) Speed response of the IM. (e) Steady-state response of the phase voltage and the total load current.

Chapter 7

Networked Control and Power Management of Hybrid AC/DC Microgrids Supplying Variable Static and Dynamic Loads

This chapter addresses power management and control strategies of a hybrid microgrid system that comprises two ac and dc subgrids, each consists of multiple DG units and local loads. Both entities are interconnected by VSCs to facilitate a bidirectional power flow and increase the system reliability. The control of the interconnecting VSC can be achieved autonomously. However, it is shown that the autonomously controlled hybrid microgrid fails to operate following variations in the power generation characteristics of the local DG units (such as droop coefficients, set points, or loss/connection of the individual DG units, etc). A supervisory controller is therefore proposed and compared to the autonomous scheme. Small-signal stability analysis is conducted to investigate the influence of the communication delays on the system stability. The proposed active compensation technique in Chapter 6 has been utilized to accommodate direct-online IM loads at the ac-side of the Hybrid AC/DC Microgrid system. Time-domain simulations under Matlab/Simulink® environment are presented to show the effectiveness of the proposed techniques and the drawbacks of the conventional scheme.

7.1 Hybrid AC/DC System Structure

A generalized hybrid system, shown in Figure 7.1, is considered. The system comprises an ac subgrid that is formed by aggregating the individual ac DG units and distributed loads along a common ac bus. Similarly, the dc bus aggregates the corresponding individual DG units and loads to form a dc subgrid. The dc subgrid is interfaced to the ac system by one (or more) interconnecting VSC. In the grid-connected mode, any dc demand that exceeds the generation capacity of the individual dc DG units can be imported from the utility-grid via the interconnecting VSCs [80]. In the islanded mode, the operation of the hybrid system is more challenging. The interconnecting VSCs have to be properly controlled to manage the bidirectional power exchange to accommodate the excessive ac/dc demands with minimal power disruptions or load shedding. This objective should be accurately achieved regardless the control modes or parameters of the local DG units in both subgrids.

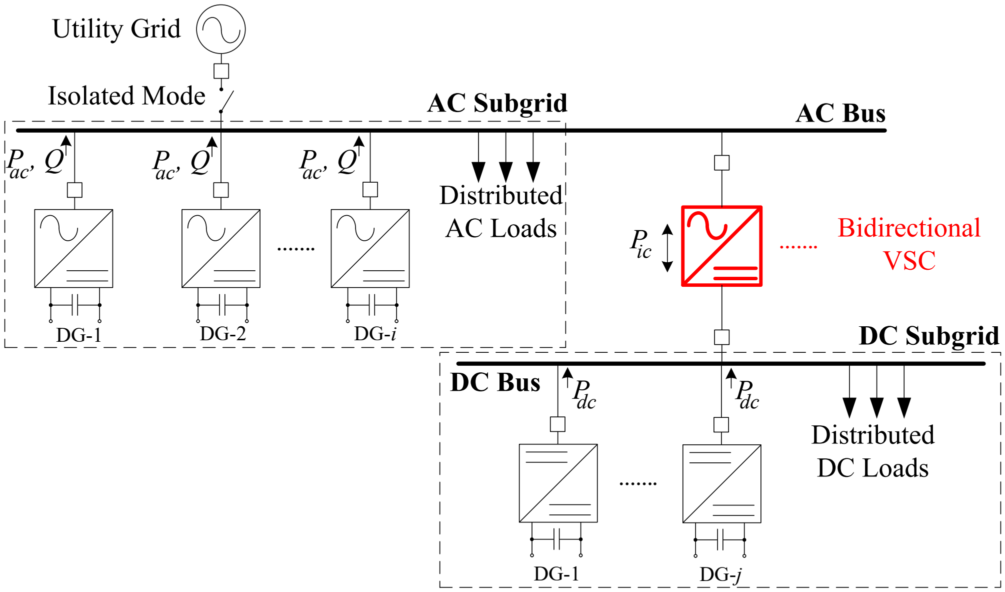

Figure 7.1 A hybrid ac/dc active distribution system.

Figure 7.2 shows the detailed hybrid system structure where the ac and dc subgrids are formed by "i" and "j" individual DG units, respectively, and are interfaced by "k" interconnecting VSCs. The ac systems are all controlled in the rotating d-q reference frame. The hybrid system models and control loops are detailed in Appendix 7.1.

7.1.1 AC Subgrid

The individual ac DG units consist of three-phase voltage-source inverters (VSIs) fed from two types of dc sources; 1) A dc current source to emulate a non-dispatchable DG units such as a PV or wind, and are current-controlled in the rotating reference frame. 2) A dc voltage source to represent dispatchable DG units which are controlled by the conventional droop scheme as detailed in the following.

Figure 7.3(a) shows the individual droop characteristics of two DG units in the ac subgrid. The operating frequency (ω_i) is linearly related to the corresponding injected active powers (P_{aci}) according to the droop coefficient (m_{aci}). The plot in Figure 7.3(a) is mathematically represented by (7.1) where the subscript i represents the DG unit number; ω_i^* is the no-load operating frequency whereas δ_i is the orientation angle.

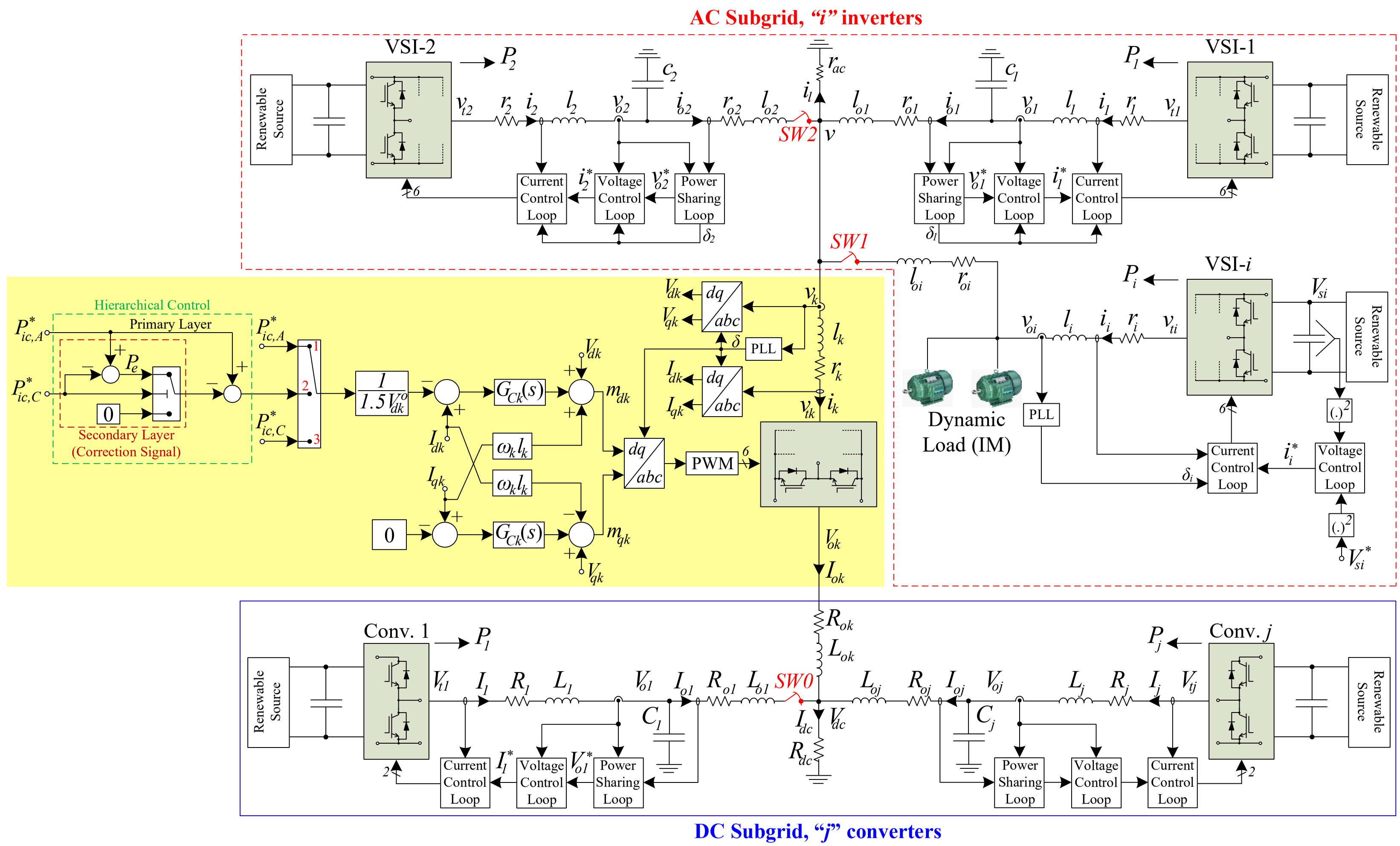

Figure 7.2 The hybrid system under study.

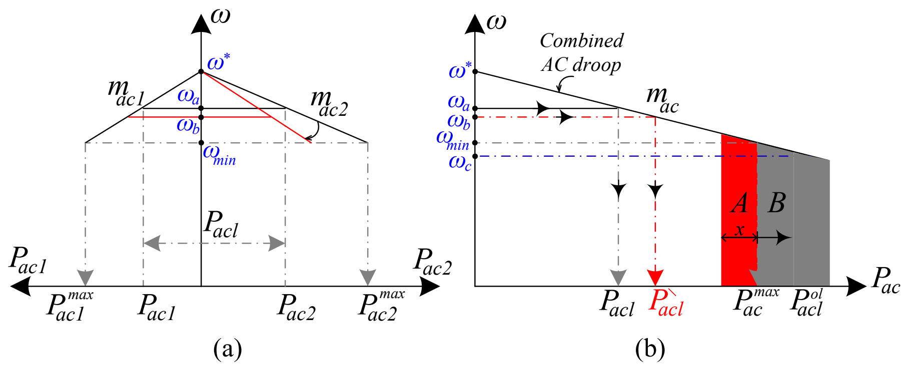

Figure 7.3 AC droop – The droop curve of unit-1 is mirrored for better representation. (a) Individual droop of two DG units. (b) Combined droop for the entire ac subgrid.

$$\begin{aligned} \omega_i &= \omega_i^* - m_{aci} P_{aci}, \\ \delta_i &= \int \omega_i \, dt. \end{aligned} \tag{7.1}$$

The injected active power from each individual DG unit (P_{aci}) is wirelessly determined to satisfy the common ac-load (P_{acl}), following the equality $m_{ac1}P_{ac1} = m_{ac2}P_{ac2}$ where $P_{acl} = P_{ac1} + P_{ac2}$ and hence one operating frequency prevails [ω_a in Figure 7.3(a)]. If the droop coefficient m_{ac2} is slightly increased, the power share from the DG unit-2 decreases to satisfy the same load at the expense of lower operating frequency (ω_b) and a higher share from the DG unit-1.

The reactive power of the ac-load can be shared among the individual DG units as well. The generated reactive power from each individual DG unit is related to the magnitude of the terminal ac voltage by the corresponding droop coefficient [87]. Active power support is the main concern of this work and hence the reactive power sharing is not shown here.

7.1.2 DC Subgrid

The individual dc DG units are half-bridge dc/dc converters fed from a dc voltage source. The conventional droop-based power sharing in the dc subgrid is shown in Figure 7.4(a). The terminal dc-link voltage of each dc/dc converter is drooped with the generated dc power (P_{dcj}) via the droop coefficient m_{dcj} as shown in (7.2),

$$V_{oj}^* = V_{oj}^n - m_{dcj} P_{dcj} \tag{7.2}$$

where V_{oj}^{*}, V_{oj}^{n} are the reference and no-load dc-link voltage of the dc/dc converter whereas the subscript j represents the individual DG unit in the dc subgrid. The injected dc power from each DG unit (P_{acj}) is wirelessly determined to supply the common dc-load (P_{dcl}), following the equality $m_{dc1}P_{dc1} = m_{dc2}P_{dc2}$ where $P_{dcl} = P_{dc1} + P_{dc2}$. Unlike the active power sharing in the ac subgrid, inaccurate dc power sharing is more likely yielded due to the transmission line losses that impose different voltages at the terminals of the individual DG units. This problem is also yielded in the reactive power sharing in ac subgrids. Some mitigation techniques can be implemented to enhance the power sharing accuracy as discussed in [87].

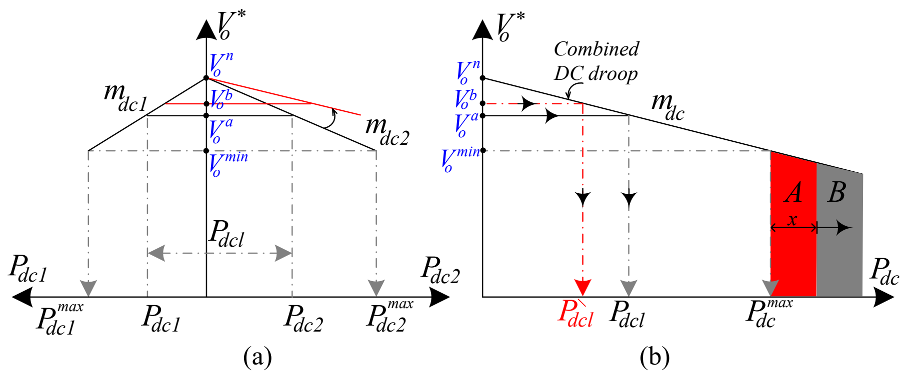

Figure 7.4 DC droop – The droop curve of unit-1 is mirrored for better representation – assume lossless transmission lines. (a) Individual droop of two DG units. (b) Combined droop for the entire dc subgrid.

7.1.3 The Interconnecting Voltage-Source Converter

As shown in Figure 7.2, the interconnecting converter is a three-phase PI current-controlled VSC in the rotating reference frame. The interconnecting VSC is not responsible for reactive power support and hence the q-component of the ac current is set to zero [69]. The d-component follows its reference to determine the amount of the active power. The reference value is defined from the power management algorithm; either using autonomous schemes [selector "1"], the proposed supervisory controller [selector "3"], or the hierarchical controller that combines both schemes [selector "2"].

7.2 Autonomous Power Management of the Hybrid AC/DC Microgrid

Referring to Figure 7.2, assume that the switch SW1 is open, and each subgrid comprises two droop-based DG units and are interconnected by one VSC. To operate the interconnecting VSC autonomously, the loading status in both subgrids should be determined without communication. This can be achieved indirectly by summing the individual droop characteristics of all individual DG units inside both subgrids as shown in Figures 7.3(b)-7.4(b) [69]. Based on Figure 7.3(b), the maximum generation capacity of the ac subgrid is P_{ac}^{max} which corresponds to the minimum allowed operating frequency (ω_{min}). The points (0, ω^*) and (P_{ac}^{max}, ω_{min}) form the augmented droop slope of the entire ac subgrid as described in (7.3),

$$P_{ac}^{max} = \frac{\omega^* - \omega_{min}}{m_{ac}} \tag{7.3}$$

where m_{ac} is the augmented droop coefficient of the entire ac subgrid. From Figure 7.3(a),

$$P_{ac}^{max} = P_{ac1}^{max} + P_{ac2}^{max} = \frac{\omega^* - \omega_{min}}{m_{ac1}} + \frac{\omega^* - \omega_{min}}{m_{ac2}} \tag{7.4}$$

$$\frac{1}{m_{ac}} = \frac{1}{m_{ac1}} + \frac{1}{m_{ac2}} \tag{7.5}$$

Generally, with "i" individual DG units, the droop coefficient of the entire ac subgrid is given by,

$$\frac{1}{m_{ac}} = \sum_i \frac{1}{m_{aci}} \tag{7.6}$$

Similarly, and referring to Figure 7.4 the augmented droop coefficient of the entire dc subgrid (m_{dc}) is given by (7.7).

$$\frac{1}{m_{dc}} = \sum_j \frac{1}{m_{dci}} \tag{7.7}$$

Using the combined droop plots in Figures 7.3(b)-7.4(b), the local loading of the ac and dc subgrids can be determined by measuring the dc voltage and frequency at the terminals of the interconnecting VSC. As shown in Figure 7.3(b), if the measured frequency is below the minimum threshold value ($\omega < \omega_{min}$), e.g., at $\omega = \omega_c$, the ac subgrid is detected overloaded and the amount of overload power is as follows.

$$P_{acl}^{ol} - P_{ac}^{max} = \frac{\omega^* - \omega_c}{m_{ac}} - \frac{\omega^* - \omega_{min}}{m_{ac}} = \frac{\omega_{min} - \omega_c}{m_{ac}} \tag{7.8}$$

From (7.8), both ω_{min} and m_{ac} are known from the combined droop plot; $\omega = \omega_c$ is measured at the ac terminals of the interconnecting VSC, and hence the amount of overload power ($P_{acl}^{ol} - P_{ac}^{max}$) is autonomously determined. As the ac subgrid is connected to the dc entity via the interconnecting VSC, the overload power can be compensated. The ac subgrid places a power request ($P_{ic,ac}$) to import the deficit. On the contrary, if $\omega > \omega_{min}$, the ac subgrid is detected underloaded and no external support is needed. Similar to the ac subgrid, the dc subgrid places a power request if the dc voltage is below the minimum threshold value [$V_o < V_o^{min}$ in Figure 7.4(b)] whereas no external support is needed when $V_o > V_o^{min}$. This scenario is mathematically formulated in (7.9) where the final power processed through the interconnecting VSC is $P_{ic,A}^* = -P_{ic,ac} + P_{ic,dc}$, which is positive in the rectification mode, negative in the inversion mode, and zero if both subgrids are over- or under-loaded.

$$P_{ic,ac} = \begin{cases} \frac{\omega_{min} - \omega}{m_{ac}}, & when\ \omega < \omega_{min} \\ 0, & else. \end{cases}, \tag{7.9a}$$

$$P_{ic,dc} = \begin{cases} \frac{V_o^{min} - V_o}{m_{dc}}, & when\ V_o < V_o^{min} \\ 0, & else. \end{cases}, \tag{7.9b}$$

$$P_{ic,A}^* = \begin{cases} 0, & when\ \omega < \omega_{min}\ \&\ V_o < V_o^{min} \\ -P_{ic,ac} + P_{ic,dc}, & else. \end{cases}. \tag{7.9c}$$

The generated power command ($P_{ic,A}^*$) in (7.9c) is then used to generate the current controller reference in the control structure of the interconnecting VSC as shown in Figure 7.2 [selector "1"]. The subscript "*ic,A*" represents the autonomous control of the interconnecting VSC. Note that a safety margin can be multiplied by the final value in (7.9c), e.g., 0.95, to ensure a safe operation [69].

7.2.1 Drawbacks of the Autonomous Strategy

The main drawback of the autonomous operation of the hybrid system is that the droop coefficients of the individual DG units have to be combined as shown in Figures 7.3(b)-7.4(b). The combined droop curves are obtained based on the pre-knowledge and fixed assumption of the droop characteristics of the individual DG units. However, this assumption may be violated due to:

1) The droop coefficients of the individual DG units are not only determined according to their kVA ratings but following variable economical conditions such as the fuel price, the selling price of the kWh, running cost, and any penalties imposed by the system operator or the market [112]-[115]. Therefore, the droop characteristics of some individual DG units may be static (constant), dynamic (variable slope, i.e., droop coefficient and/or set points), or optimized (highly nonlinear) [112].
2) Some individual DG units might be disconnected due to the scheduled maintenance [115] or unscheduled issues such as faults.
3) Some other new individual DG units might be connected to the system.

Based on the above reasons, it is clear that the pre-combined droop curves of the individual DG units might reflect a deceptive image of the actual loading condition inside the subgrid. For instance, refer to Figure 7.3(a) where the common ac frequency is ω_a and both DG units inject P_{ac1} and P_{ac2} to satisfy the common ac-load (P_{acl}). The same loading status is accurately reflected on the augmented droop curve in Figure 7.3(b); at $\omega = \omega_a$, $P_{ac} = P_{ac1} + P_{ac2}$. However, if the droop coefficient of the DG unit-2 is slightly increased [the new red line in Figure 7.3(a)], the operating frequency decreases to ω_b so that the ac subgrid satisfies the same ac-load. As shown in Figure 7.3(b), the measured ω_b reflects a loading of $P_{acl}^{\backslash}$ which is higher than the actual load (P_{acl}). The deviation from the accurate case depends on the difference $x = P_{acl}^{\backslash} - P_{acl}$. If the actual loading (P_{acl}) lies in zone-A, the ac subgrid will be detected overloaded and the interconnecting VSC may start to operate unnecessarily (if there is a surplus power on the dc side.) Any actual ac loading located in zone-B will be supported by a higher amount of power from the dc subgrid (i.e., the power flow via the interconnecting VSC is not minimized.)

Figure 7.4(a) shows the opposite situation where the dc droop coefficient (m_{dc2}) is slightly decreased [the new red line] whereas the dc-load is still the same. As a result, the common dc voltage of the dc subgrid increases from V_o^a to V_o^b. On the augmented droop curve [Figure 7.3(b)], V_o^b corresponds to $P_{dcl}^{\backslash}$ which less than the actual is loading inside the dc subgrid. If the actual loading (P_{dcl}) is in zone-A, the interconnecting VSC will not start to operate in spite of the actual overloading condition. Any actual loading in zone-B will be supported by less amount of power from the ac subgrid.

Note that the droop coefficients can be updated using a tertiary control layer so that the autonomous controller generates accurate references [70]. However, it is assumed in this chapter that the autonomous controller is not supported by any communication infrastructure.

7.2.2 Time-Domain Simulations

Based on Figure 7.2, two identical droop-based VSIs rated at 1.0 MVA forms the ac subgrid. The dc subgrid consists of two dc/dc converters rated at 1.0 MW. Both subgrids (2.0 MW generation capacities) are interconnected by an 1.0 MVA VSC.

7.2.2.1 Successful Operation

Consider the ideal case, i.e., the droop coefficients of all individual DG units are set to 1 p.u., and are static. Therefore, the augmented droop curve of both subgrids successfully reflects their actual loading condition. As shown in Figure 7.5 with $1.0\ \mathrm{p.u.}$ droop coefficients, both ac and dc subgrids are initially loaded by 1.0 MW before $t = 2.0$ s (i.e., underloaded) and hence the interconnecting VSC is not working. At $t = 2.0$ s, the dc subgrid load is suddenly increased to 2.25 MW (overloaded by 0.25 MW) whereas the ac subgrid load is kept unchanged. Therefore, the interconnecting VSC starts to operate and transmits 0.25 MW from the ac side so that the dc subgrid is maintained healthy at 2.0 MW.

7.2.2.2 False Operation

At $t = 1.5$ s, the droop coefficient of one individual dc DG unit (m_{dc1}) is initially changed to $0.7\ \mathrm{p.u.}$ and hence the augmented droop plot of the dc subgrid is no longer accurate. Referring to Figure 7.4(a), the reduction of m_{dc1} is followed by an increase in the common dc-link voltage such that the actual overloaded conditions might not be detected [zone-A.] This is clear from Figure 7.5 where the interconnecting VSC totally fails to start. The dc subgrid maintains the overloaded condition in spite of the availability of a surplus power at the ac side.

Another case is also shown in Figure 7.5 when m_{dc1} is reduced to 0.9 p.u. at $t = 1.5$ s such that the operation of the interconnecting VSC is in zone-B [Figure 7.4(b)]. The interconnecting VSC supports the dc subgrid with less amount of power than actually needed, which leaves the dc subgrid overloaded by 0.1 MW. Similar to Figure 7.3(a), m_{dc1} is increased to 1.1 p.u. so that the common dc-link voltage decreases under the same loading conditions. This is associated with a higher amount of transmitted power to the dc subgrid than actually needed, i.e., the interconnecting VSC is unnecessarily loaded. In other words, the power flow through the interconnecting VSC is not minimized in some cases.

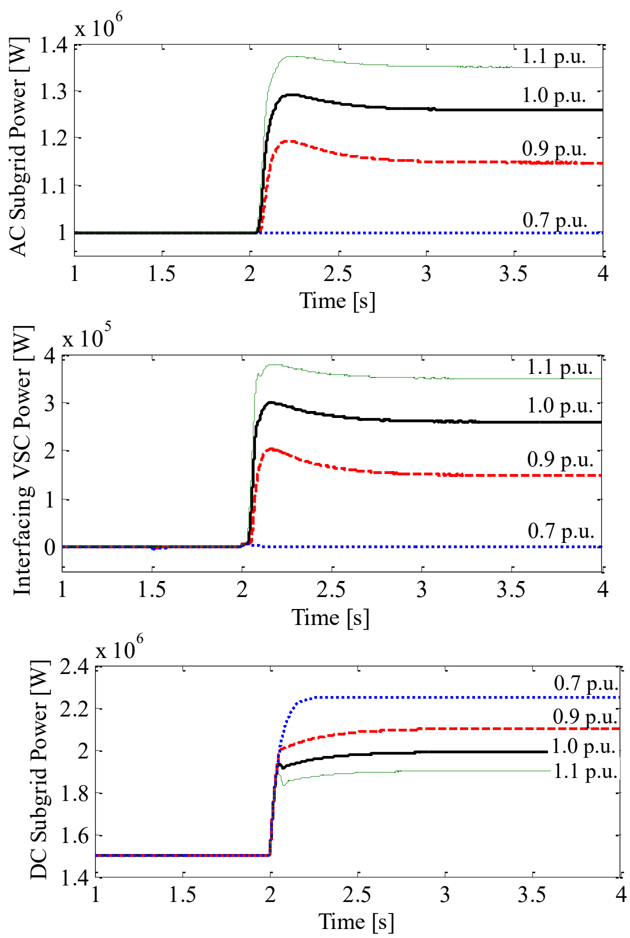

Figure 7.5 Autonomous operation of the hybrid system when the dc subgrid is overloaded at $t = 2$ s and m_{dc1} is varied from 0.7 to 1.1 p.u. at $t = 1.5$ s.

7.3 Networked Control and Supervisory Power Management Scheme

Motivated by the aforementioned difficulties and drawbacks of the autonomous schemes, an efficient supervisory power controller for the islanded hybrid system in Figure 7.2 is proposed. The controller is designed so that the hybrid system operates according to the following features:

- The power flows from the underloaded to the overloaded subgrid via the interconnecting VSC. No power transmission is allowed if both subgrids are under- or over-loaded.
- The priority of the power supply is given to the local load within the underloaded entity over exportation to the overloaded side. The power transmission should be automatically updated as the local loading increases in the underloaded subgrid.
- The supervisory controller is only implemented in the interconnecting VSCs to keep both subgrids under their own control scheme (i.e., droop-based, power control, etc.) This allows a flexible operation without imposing any requirements from the supervisory controller.
- Unlike the autonomous scheme, the operation of the hybrid system should be independent of the control topologies of the local DG units in both subgrids. For droop-based DG units, the operation should be flexible to accommodate any variations in the droop coefficients, set points, or connections/disconnection of units without affecting the power transfer. The intermittent nature of non-dispatchable resources is also considered.

7.3.1 Input Signals to the Supervisory Controller

As shown in Figure 7.6, the inputs to the supervisory controller are:

- *AC DG units:* each unit sends its maximum kVA (S_i^{max}) that can be generated and the active ($P_{ac,i}^{meas}$) and reactive (Q_i^{meas}) power measurements.
- *DC DG units:* they send their maximum power ($P_{dc,j}^{max}$) that can be generated and the actual power measurement ($P_{dc,j}^{meas}$).
- *Interconnecting VSCs:* they send their maximum active power that can be transmitted ($P_{ic,k}^{max}$) and the actual active power measurements ($P_{ic,k}^{meas}$).

Note that the power measurements are only needed at each DG unit as well as the interconnecting VSCs. This complies with IEEE 1547 standards where each DG unit of

0.25 MVA or more shall have provisions for monitoring the active and reactive powers [49]. On the other side, no measurements are needed at the terminals of loads.

The received quantities are summed together to obtain the amount of total powers (subscript "tot"), as shown in Table 7.1. The following quantities are then calculated,

$$P_{ac}^{cap} = \sqrt{(S_{tot}^{max})^2 - (Q_{tot}^{meas})^2},$$
$$P_{dc}^{cap} = P_{dc,tot}^{max}. \tag{7.10}$$

where the superscript "cap" denotes the power generation capacity, i.e., the maximum power that can be generated from the corresponding subgrid. This term is similar to the maximum power generation of the dc subgrid but is different in the ac subgrid to account for the local reactive power generation.

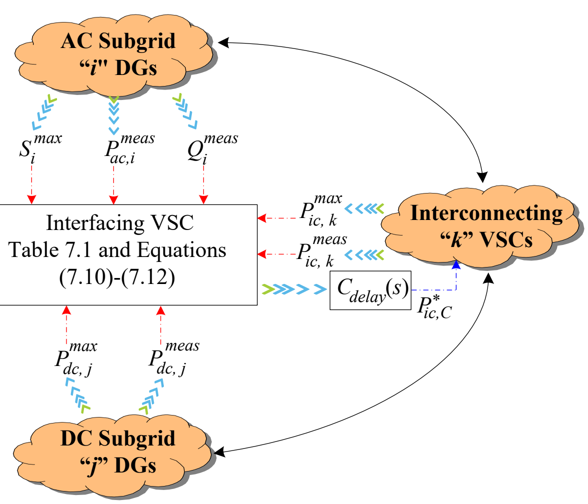

Figure 7.6 Input/output signals to/from the supervisory controller.

Table 7.1 Received Signals by the Supervisory Controller

AC Subgrid	DC Subgrid	Interfacing VSCs
$S_{tot}^{max} = \sum_{i=1}^{n_i} S_i^{max}$	$P_{dc,tot}^{max} = \sum_{j=1}^{n_j} P_{dc,j}^{max}$	$P_{ic,tot}^{max} = \sum_{k=1}^{n_k} P_{ic,k}^{max}$
$Q_{tot}^{meas} = \sum_{i=1}^{n_i} Q_i^{meas}$, $P_{ac,tot}^{meas} = \sum_{i=1}^{n_i} P_{ac,i}^{meas}$	$P_{dc,tot}^{meas} = \sum_{j=1}^{n_j} P_{dc,j}^{meas}$	$P_{ic,tot}^{meas} = \sum_{k=1}^{n_k} P_{ic,k}^{meas}$

7.3.2 Estimation of the Loading Conditions in the AC/DC Subgrids

Following the behavioral schematic of the hybrid system in Figure 7.7, the power flow through the interconnecting VSC ($P_{ic,tot}^{meas}$) is positive in the rectification and negative in the inversion mode. In the rectification mode, the actual power consumption inside the ac subgrid (P_{ac}^{load}) is the measured generated power from all individual ac DG units ($P_{ac,tot}^{meas}$) minus the power flowing through the interconnecting VSC. In the inversion mode, $P_{ac}^{load} = P_{ac,tot}^{meas} - (-P_{ic,tot}^{meas})$. In a similar manner, the actual loading in the dc subgrid (P_{dc}^{load}) can be estimated as shown in (7.11).

$$\begin{aligned} P_{ac}^{load} &= P_{ac,tot}^{meas} - P_{ic,tot}^{meas}, \\ P_{dc}^{load} &= P_{dc,tot}^{meas} + P_{ic,tot}^{meas}. \end{aligned} \tag{7.11}$$

Using (7.10)-(7.11), the subgrid is detected overloaded if $P_x^{cap} < P_x^{load}$ and is underloaded if $P_x^{cap} > P_x^{load}$ where the subscript x denotes ac or dc.

The power signals from all power electronic converters in the hybrid system are sent to the supervisory controller as long as the corresponding unit is healthy. Therefore, the generation and transmission capacity of both subgrids and interconnecting VSCs are continuously updated.

To ensure a safe operation of the interconnecting VSC and both subgrids, the maximum power that can be generated by all DG units in both subgrids, i.e., S_i^{max} and $P_{dc,j}^{max}$, are multiplied by a safety margin $\varepsilon = 0.95$. From (7.10), the safety margin reflects less power generation capacity than actually available in both subgrids to account for any fast changing transients or loading conditions.

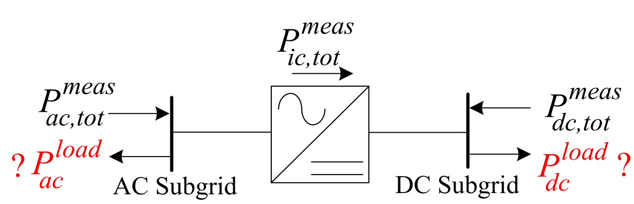

Figure 7.7 Estimation of the loading condition inside both subgrids.

7.3.3 Output Signals from the Supervisory Controller

As shown in Figure 7.6 and (7.12), the output signal is the amount of the power that has to be transmitted between both subgrids, i.e., the power command to the interconnecting VSCs ($P_{ic,C}^{*}$). The subscript "ic,C" denotes the supervisory scheme.

As shown, $P_{ic,C}^{*}$ has three different modes. The first is the rectification, shown in (7.12a). It is activated when the dc subgrid is overloaded ($P_{dc}^{load} > P_{dc}^{cap}$) and the ac subgrid is underloaded ($P_{ac}^{load} < P_{dc}^{cap}$). The first term ($\left|P_{dc}^{cap} - P_{dc}^{load}\right|$) denotes the amount of deficit power needed to satisfy the overload in the dc subgrid. The second term ($\left|P_{ac}^{cap} - P_{ac}^{load}\right|$) denotes the amount of the surplus power in the ac subgrid that can be exported. If the deficit dc power is initially less than the surplus ac power, the dc subgrid is completely supported. Similarly, if both quantities are equal, the output will be either and the dc subgrid will be totally supported. However, if the local ac load increases during this mode such that $\left|P_{ac}^{cap} - P_{ac}^{load}\right|$ becomes less than $\left|P_{dc}^{cap} - P_{dc}^{load}\right|$, the dc subgrid is then partially supported. The highest priority is given to supplying the local load inside the underloaded subgrid.

$$P_{ic,C}^{*} = \begin{cases} minimum\left\{\left|P_{dc}^{cap} - P_{dc}^{load}\right|, \left|P_{ac}^{cap} - P_{ac}^{load}\right|\right\}, & (7.12a) \\ when\ \left(P_{dc}^{load} > P_{dc}^{cap}\right)\ and\ \left(P_{ac}^{load} < P_{ac}^{cap}\right) & \\ -minimum\left\{\left|P_{dc}^{cap} - P_{dc}^{load}\right|, \left|P_{ac}^{cap} - P_{ac}^{load}\right|\right\}, & (7.12b) \\ when\ \left(P_{dc}^{load} < P_{dc}^{cap}\right)\ and\ \left(P_{ac}^{load} > P_{ac}^{cap}\right) & \\ 0, else & (7.12c) \end{cases}$$

The second mode of operation is the inversion, shown in (7.12b), when the dc subgrid is underloaded $\left(P_{dc}^{load} < P_{dc}^{cap}\right)$ simultaneous with an overloading condition in the ac side $\left(P_{ac}^{load} > P_{ac}^{cap}\right)$. P_{ic}^{*} is negative for the reversed power direction whereas $\left|P_{dc}^{cap} - P_{dc}^{load}\right|$ and $\left|P_{ac}^{cap} - P_{ac}^{load}\right|$ denote the amount of surplus and deficit powers, respectively. As shown in (7.12c), the interconnecting VSC is not working if both subgrids are simultaneously over- or under-loaded. The power command of the interconnecting VSC is used to determine the value of the current controller reference [Figure 7.2, selector "3"].

It is clear that the operation of the interconnecting VSC is independent of the droop characteristics of the individual DG units as it processes the amount of injected power from each DG unit regardless the mode of operation.

7.3.4 Parallel Operation of Multiple Interconnecting Converters

Parallel operation is considered either to increase the system reliability or the amount of power transmission between both subgrids. As shown in (7.13), the generated power command ($P_{ic,C}^{*}$) in (7.12) can be shared among parallel operated interconnecting VSCs according to their power ratings where $P_{ic,C}^{*} = \sum_{k=1}^{n_k} P_{ic,k}^{*}$.

$$P_{ic,k}^{*} = \left(\frac{P_{ic,k}^{max}}{P_{ic,tot}^{max}}\right) P_{ic,C}^{*} \tag{7.13}$$

7.3.5 Sensitivity Analysis – Influence of the Communication Delays

The small-signal stability analysis is conducted to investigate the influence of the communication delays on the system stability. Referring to Figure 7.6, $C_{delay}(s)$ represents the communication delay transfer function where τ_d is the communication delay time and s is the Laplace operator [116].

$$C_{delay}(s) = \frac{1}{1+\tau_d s} \tag{7.14}$$

For simplicity, the system in Figure 7.2 is considered in the small-signal stability analysis but with switches SW0, SW1, and SW2 opened. The small-signal state-space model is obtained under two modes of operation; rectification and inversion, assuming a full support from the underloaded toward the overloaded entity, and, therefore, the power command to the interconnecting VSC is as follows.

$$P_{ic,C}^{*} = \begin{cases} C_{delay}(s)\left(P_{dc}^{load} - P_{dc}^{cap}\right), & \text{recitifcation mode} \\ -C_{delay}(s)\left(P_{ac}^{load} - P_{ac}^{cap}\right), & \text{inversion mode} \end{cases} \tag{7.15}$$

The small-signal system models are detailed in Appendix A7.2 whereas the complete system parameters are given in Appendix A7.3. The small-signal state-space model considers the entire power circuit and controller dynamics of the hybrid system and consists of 26 states; 13 for the ac droop-based VSI, six for the dc droop-based dc/dc converter and seven for the interconnecting VSC. The most dominant Eigenvalues are investigated when the communication delay increases from 0.001 to 1.0 s. At $\tau_d = 1.0$ s, the most dominant Eigenvalue is relocated to -0.8 and $-4.9\ s^{-1}$ under the rectification and inversion modes as shown in Figures 7.8(a)-7.8(b), respectively.

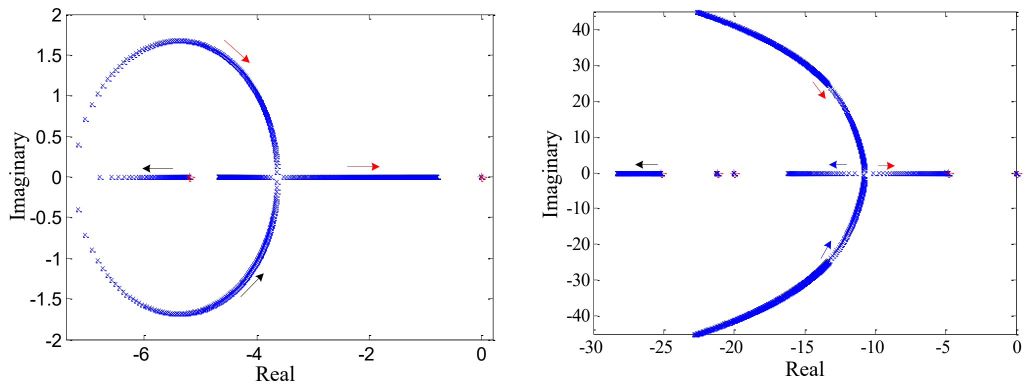

(a) (b)

Figure 7.8 The small-signal stability of the hybrid system – the communication delay (τ_d) increases from 0.001 to 1.0 s. (a) Rectification mode. (b) Inversion mode.

7.4 Evaluation Results

A large-signal time-domain model for the islanded hybrid system in Figure 7.2 is built under Matlab/Simulink to investigate the capabilities of the proposed supervisory controller. All model entities are built using SimPowerSystem® toolbox. The converters are simulated using average-model-based blocks. The ac subgrid comprises two droop-controlled VSIs and a PQ-controlled DG unit. Two 200 hp (0.15 MVA) direct-online IMs are connected to the ac subgrid. The influence of the dynamic loading on the operation of the supervisory controller is therefore investigated. The dc subgrid comprises two droop-controlled half-bridge dc/dc converters to supply a resistive load. The two entities are interconnected by one VSC. The no-load frequency and dc voltage of both subgrid is 60.8 Hz and 2500 v, respectively.

7.4.1 Static Loading Conditions

In this section, the switch SW1 in Figure 7.2 is open. Figure 7.9 shows the local loading conditions in each subgrid where the maximum allowed loading is 2.0 MW and is equally shared between the two DG units. The loading is initially 1.0 MW and increases to 2.3 and 2.5 MW at $t = 3$ and 9 s, respectively, in the overloaded case. The underload condition is 1.0 MW and increases to 1.3, 1.8, 2.0 MW at $t = 5, 7, 8$ s, respectively, and decreases back to 1.5 MW at $t = 9$ s.

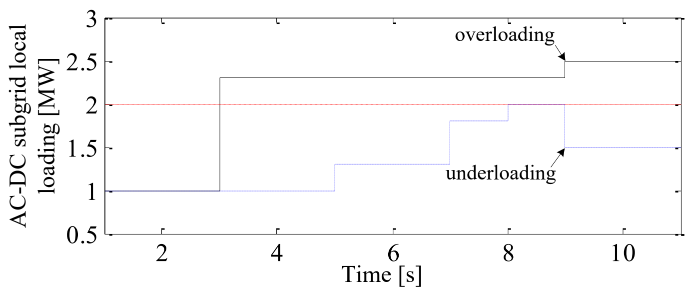

Figure 7.9 Local loading scenarios in both subgrids.

7.4.1.1 Rectification Mode

The local dc-load follows the overloaded plot in Figure 7.9 whereas the ac-load follows the underloaded curve so that the interconnecting VSC operates in the rectification mode. The complete system response is shown in Figures 7.10. The system performance can be described as following:

- $t = 0\ to\ 3$ s: Both subgrids are underloaded and hence the interconnecting VSC is not working.
- $t = 3\ to\ 5$ s: The dc subgrid is overloaded (2.3 MW) whereas the ac subgrid is still underloaded (1.0 MW). The interconnecting VSC starts to operate and transmit the 0.3 MW dc power deficit from the ac side. As result, the dc subgrid is maintained healthy at 2.0 MW and the ac subgrid generation increases to 1.3 MW. At $t = 4$ s, the droop coefficient of the dc DG unit-2 is decreased from 1.0 to 0.7 p.u. so that the dc subgrid voltage increases from 2375 to 2396 V. This variation does not affect the accuracy of the power transfer.

- $t = 5\ to\ 7$ s: The dc subgrid is still overloaded (2.3 MW) but the local ac-load increases from 1.0 to 1.3 MW. The amount of transmitted power through the interconnecting VSC is not affected but the ac subgrid generation increases to 1.6 MW to keep supporting the dc side. At $t = 6$ s, the droop coefficient of the dc DG unit-2 is increased from 0.7 to 1.1 p.u. This does not affect the accuracy of the power management.
- $t = 7\ to\ 8$ s: The dc subgrid is still overloaded and the local load inside the ac subgrid increases to 1.8 MW. Only 0.2 MW surplus ac power is available to support the 0.3 MW dc deficit. Based on (7.12), the supervisory controller generates the 0.2 MW power reference to the interconnecting VSC (select the minimum value). The priority is given to support the local load of the ac subgrid. The ac subgrid generation is 2.0 MW whereas the dc subgrid is partially supported and 0.1 MW dc load has to be shed. The operating frequency is at the minimum allowed value.
- $t = 8\ to\ 9$ s: The dc subgrid is still overloaded and the local load inside the ac subgrid increases to the full 2.0 MW. No surplus ac power is available and hence the interconnecting VSC will not operate. The dc subgrid load is not supported in this situation and the 0.3 MW overload has to be completely shed.
- $t = 9\ to\ 11$ s: The dc subgrid load increases to 2.5 MW whereas the ac subgrid load decreases to 1.5 MW. The interconnecting VSC operates again to import the full 0.5 MW dc deficit from the ac side.

Figure 7.11 shows the current response at the ac and dc sides of the interfacing converters as well as the total ac and dc loads in both subgrids. The current performance is well-damped and follows a similar trend to Figure 7.10.

7.4.1.2 Inversion Mode

Referring to Figure 7.9, the ac load follows the overloaded curve whereas the dc load follows the underloaded one. Therefore, a complementary scenario is yielded. The system performance is shown in Figure 7.12.

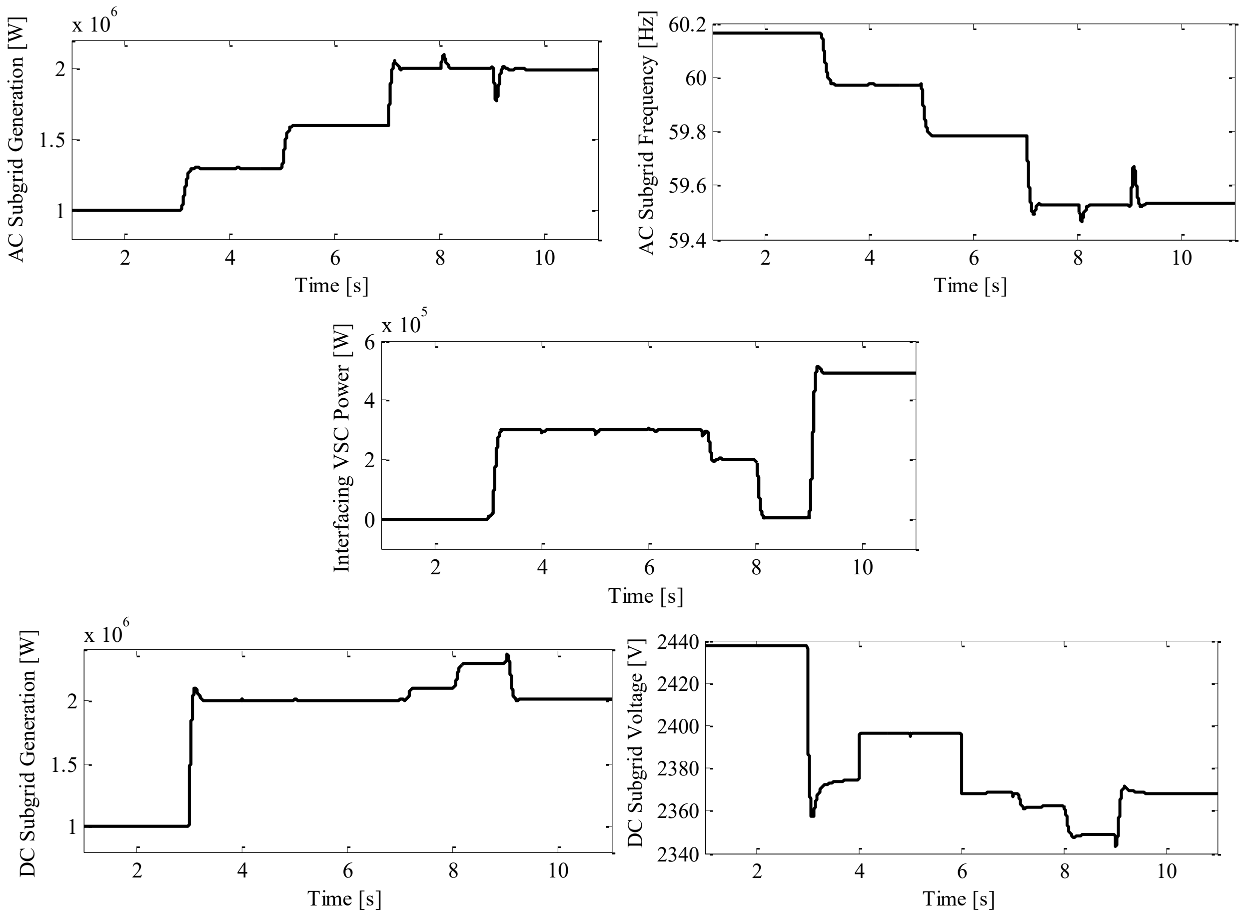

Figure 7.10 Power coordination of the hybrid system with over- and under-loaded conditions in the dc and ac subgrids, respectively (rectification mode).

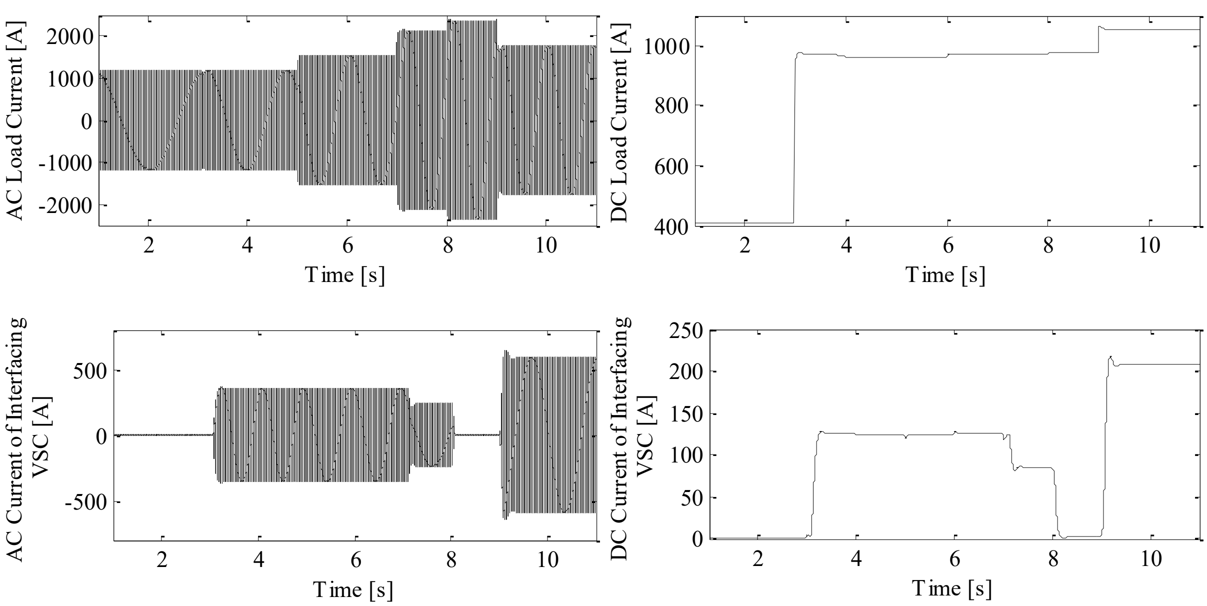

Figure 7.11 AC and DC current response of the hybrid system with over- and under-loaded conditions in the dc and ac subgrids, respectively (rectification mode).

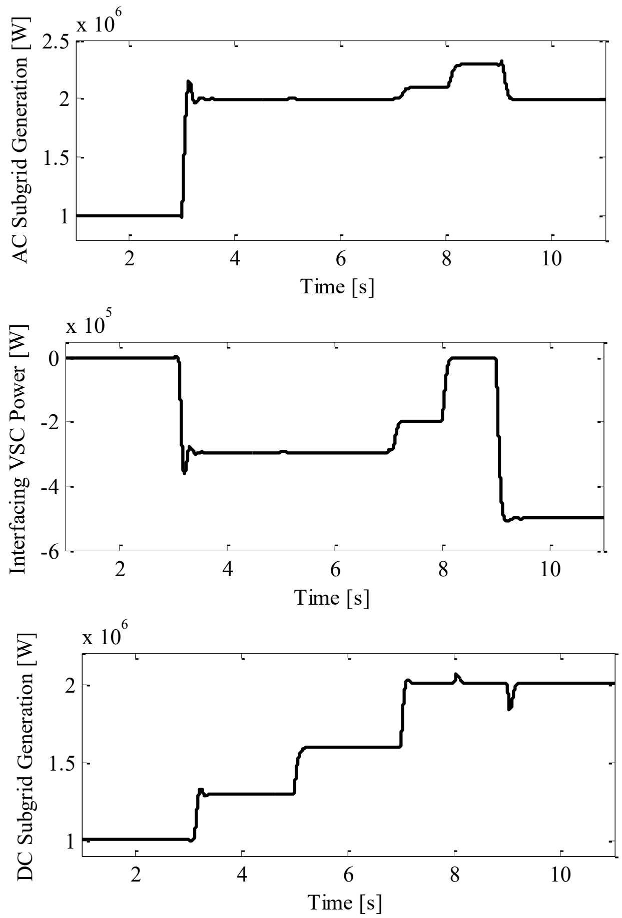

Figure 7.12 Power coordination of the hybrid system with over- and under-loaded conditions in the ac and dc subgrids, respectively (inversion mode).

7.4.1.3 Parallel Operation of the Interconnecting Converters

The parallel operation of two interconnecting VSCs is shown in Figure 7.13, under the same rectification mode shown in Figure 7.10. The amount of power transmitted between both subgrids via two interconnecting VSCs is shared according to their power ratings, where $P_{ic,1}^{max} = 2P_{ic,2}^{max}$.

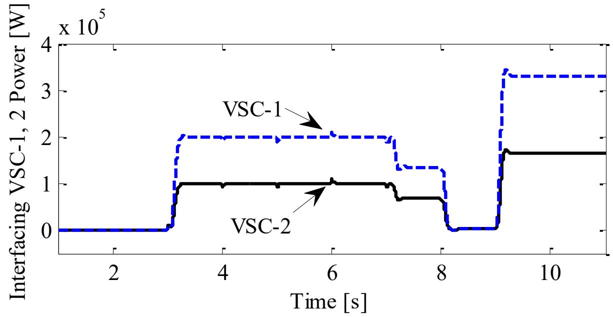

Figure 7.13 Power transfer through two parallel operated interconnecting VSCs – Same rectification scenario in Figure 7.10.

7.4.1.4 Hierarchical Control Structure of the Interconnecting Converters

To increase the reliability and maintain an adequate operation of the hybrid system, a hierarchical control strategy that combines both autonomous and supervisory schemes is adopted. As shown in Figure 7.2 (selector “2”), the difference between the autonomous and supervisory references generates the error signal (P_e). In the main layer, $P_{ic,A}^*$ is continuously generated but corrected by P_e as long as the communication network is healthy. If $P_{ic,C}^*$ is lost or fall to zero, P_e is set to zero and $P_{ic,A}^*$ is kept generated but with no correction.

As shown in Figure 7.14, the supervisory controller operates the interconnecting VSC in the rectification mode when the dc subgrid is overloaded by 0.25 MW at $t = 1.0$ s, with underloaded condition in the ac side. At $t = 2.0$ s, the droop coefficient of one dc DG unit is reduced to 0.95 p.u. In the meanwhile of the rectification process, the communication network fails to operate at $t = 3.0$ s. The hierarchical structure successfully switches the operation to the autonomous scheme. Note that the amount of the transferred power is less than needed due to the reduced dc droop coefficient at $t = 2.0$ s (a drawback of the autonomous scheme.) The communication network is restored within 1.0 s and the supervisory controller is seamlessly reactivated at $t = 4$ s.

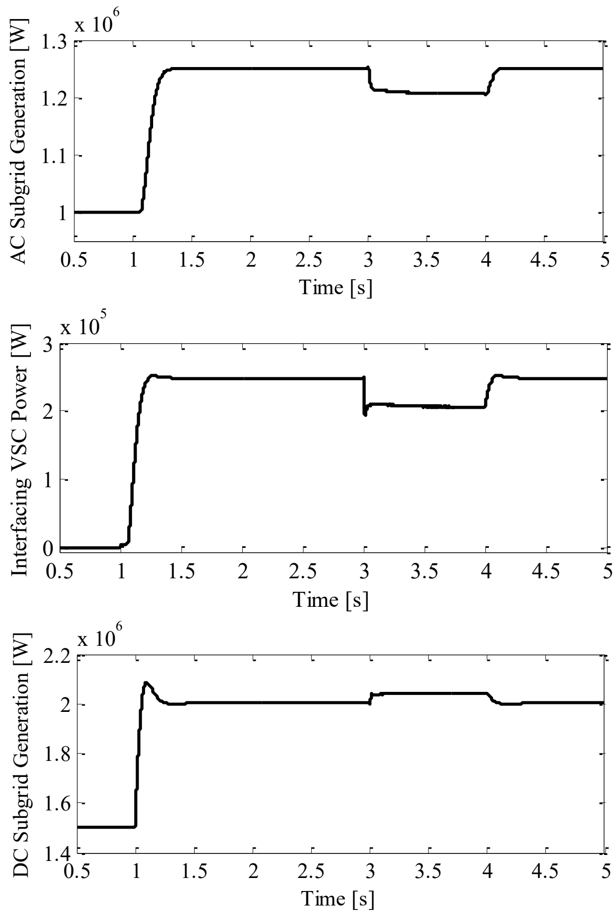

Figure 7.14 Transition from the supervisory to the autonomous control at $t = 3$ s and the restoration of the communication network at $t = 4$ s with over- and under-loaded conditions in the dc and ac subgrids, respectively (rectification mode).

7.4.2 Dynamic Loading Conditions

In this part, SW1 in Figure 7.2 is closed to consider the two 200 hp IM loads as well as the 0.3 MVA PQ-controlled DG unit. In order to accommodate the IMs in the islanded ac subgrid, the proposed active damping compensator in Chapter 6 has been implemented in the ac droop loop for all dispatchable DG units. Figure 7.15(a) shows the loading behavior in both subgrids. The power generation capacity of both entities is limited to 1.0 MVA so that the dynamic load has a considerable load share. It is also noted that the simulation time is significantly increased to 140 s for further investigations. The simulation type is discrete with a sample time of 35 μs and the actual simulation time of this scenario is $01^H:30^M:04^S$. The system response is described as following:

- $t = 0$ to 40 s: Both subgrids are underloaded at 0.5 MW. The IMs start in the free-acceleration mode, i.e., at no mechanical load. The interconnecting VSC is not working as shown in Figure 7.15(b).
- $t = 40$ to 60 s: A 800 N.m. mechanical load is applied on one IM at $t = 40$ s and hence the ac-load increases by 0.15 MW. The motor speed is decreased due to the full mechanical load as shown in Figure 7.15(c). The dc subgrid is also overloaded by 0.2 MW. As shown in Figure 7.15(b), the interconnecting VSC operates in the rectification mode to transmit the 0.2 MW to the dc side. The local generation in the dc subgrid is maintained healthy at 1.0 MW as shown in Figure 7.15(d).
- $t = 60$ to 80 s: The dc-load is fixed whereas the ac-load increases to 0.75 MW. Similar performance to the previous time interval is yielded. The ac subgrid generation increases as shown in Figure 7.15(e).
- $t = 80$ to 100 s: The dc-load decreases to 0.5 MW whereas the ac-load increases to 1.2 MW at $t = 80$ s. As shown in Figure 7.15(b), the interconnecting VSC operates in the inversion mode with a 0.2 MW reversed step power to support the ac side. At $t = 90$ s, the second IM is mechanically fully loaded so that the total ac-load increases to 1.35 MW. As the dc-load is 0.5 MW, a full support to the ac overload is still provided.
- $t = 100$ to 120 s: The dc-load increases to 0.7 MW and the ac-load is still the same. Only 0.3 MW surplus power is therefore available to support the ac side and hence 0.05 MW has to be shed.
- $t = 120$ to 140 s: The dc-load is 0.7 MW whereas the ac-load decreases to 0.9 MW. The interconnecting VSC is not working.

7.5 Conclusions

This chapter addresses the power management in a hybrid ac/dc active distribution system. The coordination schemes are achieved by an autonomous and a supervisory controller. It has been shown that the autonomously controlled interconnecting VSC is subjected to false operation in large scale hybrid systems. On the contrary, an effective supervisory controller is proposed which has the following features. 1) It is only implemented for the interconnecting VSCs whereas both subgrids are kept under their own control scheme. 2) It depends on the power measurements from the generation units only, not the loads, to decrease the number of measurement sensors and transmitted signals throughout the network. 3) It operates successfully regardless the control mode of the individual DG units in both subgrids. Therefore, the proposed controller can be generalized to different types of DG units as it only requires the active and reactive power measurements. 4) It can be generalized to large-scale hybrid systems. 5) The input signals are the average power measurements which are typically obtained using low-pass filters. Therefore, the communication bandwidth is not necessarily fast. 6) Parallel operation of multiple interconnecting VSCs can be easily considered so that the transmitted power between both subgrids is shared according to their power rating.

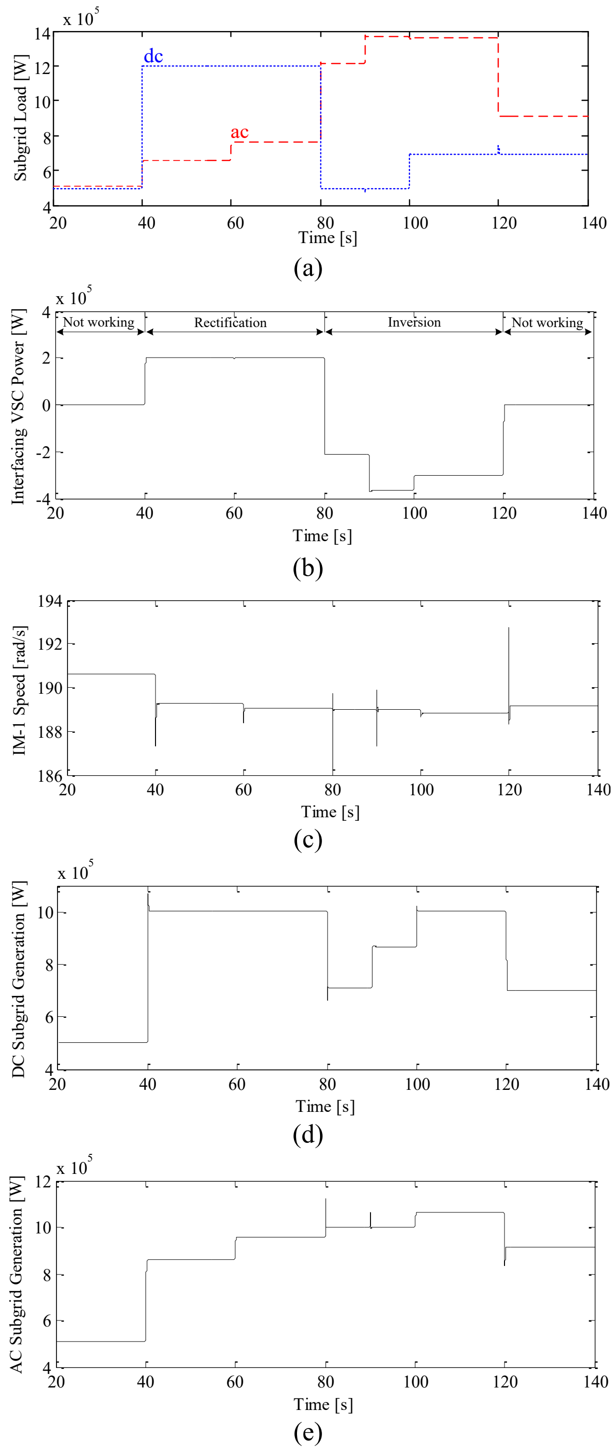

Figure 7.15 Power coordination of the hybrid system with IM loads – rectification mode from $t = 40$ to 80 s and inversion mode from $t = 80$ to 120 s.

Chapter 8

Summary and Future Work

8.1 Thesis Summary

This thesis has addressed the integration of the renewable energy resources to the active distribution systems using voltage- and current-source converters. To achieve the objectives of this thesis, different active compensation techniques and controllers have been proposed and developed for the interfacing converters. Time-domain simulations under Matlab/Simulink environment have been presented to validate the analytical results and show the effectiveness of the proposed controllers.

In Chapter 3, the integration of the CSC-based PV generators into the utility-grid has been investigated using the vector control topology. Using the small-signal dc-side impedance models of the PV generator and the interfacing CSC, the system stability has been investigated under different operating conditions. It is found that the variation of the weather conditions, particularly the insolation level, might affect the system stability. Therefore, active compensation techniques have been proposed to increase the system damping. Moreover, the lightly damped modes induced by the resonance of the CL filter of the CSC have been actively damped without affecting the conversion efficiency.

In the vector-controlled converters, the PLL is necessary to synchronize the converter to the utility-grid. However, the presence of the PLL negatively affects the system damping, particularly in the presence of a relatively high grid impedance. Therefore, a new control topology, i.e., the PSC, has been developed for the grid-connected CSC-based PV generator in Chapter 4. The PSC does not require a PLL due to its inherent synchronizing feature. The PSC-controlled CSCs provide a stable performance under the very weak grid conditions. Moreover, and unlike VSCs, the self-protection characteristic of CSCs against fault conditions gives them a very attractive feature for utility-grid integration.

The vector control strategy has been completely replaced by the PSC in Chapter 4 to avoid system instabilities under weak-grid conditions (due to the PLL). In Chapter 5, supplementary compensation loops have been proposed to facilitate the integration of CSCs to the very weak utility-grid under the vector control strategy. The proposed compensators successfully mitigate the negative influence of the PLL in the presence of high grid impedance. It could be possible to inject the full-rated active power into the utility-grid with $\mathrm{SCR} = 1.0$ using the proposed compensators.

In order to enhance the integration of the dynamic loads such as IMs into the large-scale active distribution systems, Chapter 6 has investigated the stability of VSC-based microgrids with high penetration of IM loads under the isolated mode of operation. Using the generalized Nyquist criterion, the system stability has been investigated under different operating conditions. Linear active compensation loops have been proposed to increase the system damping and maintain a stable performance under a wide range of operating points. The proposed compensators facilitate the 'plug-and-play' feature in the future microgrids.

A larger system level integration of DG units is considered in Chapter 7 where a dc subgrid is integrated to the ac microgrid in Chapter 6 using a bidirectional VSC. To enhance the bidirectional power flow, a centralized power management algorithm has been proposed. The algorithm is only developed for the bidirectional VSC; it is independent of the control structure of the local ac/dc DG units; and it provides an accurate and efficient operation under variable ac/dc loading/generation conditions, particularly under the isolated mode of operation. The proposed controllers facilitate the realization of the hybrid ac/dc active distribution systems.

8.2 Future Work

The following research directions can be followed as an extension out of this thesis:

- The utilization of the robust control theory to mitigate the dc-side interactions between the PV generator and the interfacing converter. The performance should be compared to the results of Chapter 3. In the literature, linear controllers have been proposed to decouple the dc-side dynamics between the PV generator and the interfacing converter [7]-[9]. Similarly, nonlinear controllers have been also proposed [25]. However, the robust control has not been addressed in the literature to improve the dynamic performance of the PV system following parameters and/or operating point variations. The future work includes the one-stage interfacing topology as well as multi-string topology, e.g., an interfacing centralized inverter with intermediate dc/dc converter.

- The development of the PSC for the CSC-based HVDC systems to 1) exploit the inherent short-circuit protection feature of CSCs as compared to VSCs, and 2) facilitate the interconnection to the very weak utility-grid systems. This includes a comparison study between the CSC- and VSC-based HVDC considering the dynamic stability and fault-ride through capabilities.
- The proposed supplementary compensators in Chapters 3, 5, and 6 can be implemented to enhance the stability of multiple DG units with uncertain operation of individual DG unit(s), e.g., reactive power support mode, active power mode, droop control, etc. Also, the switching of individual DG unit(s) with the associated variation in the equivalent capacitance of the overall system can be considered. First, the uncompensated system stability under different operating scenarios shall be investigated. Second, and based on the Nyquist stability criterion, the proposed compensators in this thesis can be designed and tuned to enhance the system stability margin.
- The improvement of the proposed supervisory power management controller for the hybrid ac/dc active distribution system. The reactive power support and ancillary services shall be considered in the supervisory scheme to support the ac subgrid. The supervisory controller algorithm should be improved to detect the communication loss and increase the system reliability by avoiding the single-point-failure scenario. Moreover, in Chapter 7, a simple approach to consider the communication delays has been followed. Therefore, the influence of the communication delays on the system stability and the accuracy of the bi-directional power flow should be considered thouroughly in the future.
- The consideration of different types of challenging loads, such as pulsating and non-linear loads, in the ac-side of the hybrid microgrid and the investigation of the corresponding influence on the overall system stability as well as the performance of the supervisory controller.

Bibliography

[1] F. Blaabjerg, Z. Chen, and S. B. Kjaer, “Power Electronics as efficient interface in dispersed power generation systems,” *IEEE Trans. Power Electron.*, vol. 19, no. 5, pp. 1184-1194, 2004.

[2] J. M. Carrasco, L. G. Franquelo, J. T. Bialasiewicz, E. Galván, R. C. P. Guisado, M. A. M. Prats, J. I. León, and N. M.-Alfonso, “Power-electronic systems for grid integration of renewable energy sources – a survey,” *IEEE Trans. Ind. Electron.*, vol. 53, no. 4, pp. 1002-1016, 2006.

[3] E. P. Wiechmann, P. Aqueveque, R. Burgos and J. Rodriguez, “On the efficiency of voltage source and current source inverters for high-power drives,” *IEEE Trans. Ind. Electron.*, vol. 55, no. 4, pp. 1771 – 1782, April 2008.

[4] B. Sahan, S. V. Araujo, C. Noding and P. Zacharias, “Comparative evaluation of three-phase current source inverters for grid interfacing of distributed and renewable energy system,” *IEEE Trans. Power Electron.*, vol. 26, no. 8, pp. 2304 – 2318, August 2011.

[5] P. Grbovi, F. Gruson, and F. Idir, “Turn-on performance of reverse blocking IGBT (RB-IGBT) and optimization using advanced gate driver,” *IEEE Trans. Power Electron.*, vol. 25, no. 4, pp. 970-980, 2010.

[6] M. Popat, B. Wu, F. Liu and N. Zargari, “Coordinated control of cascaded current-source converter based offshore wind farm,” *IEEE Trans. Sust. Energy*, vol. 3, no. 3, pp. 557 – 565, July 2012.

[7] P. P. Dash and M. Kazerani, “Dynamic modeling and performance analysis of grid-connected current-source inverter-based photovoltaic system,” *IEEE Trans. Sust. Energy*, vol. 2, no. 4, pp. 443 – 450, 2011.

[8] P. P. Dash and M. Kazerani, “A multi-level current-source inverter based grid-connected photovoltaic system,” *in Proc. 2011 NAPS Conf.*, pp. 1 – 6.

[9] P. P. Dash and M. Kazerani, “Harmonic elimination in a multilevel current-source inverter-based grid-connected photovoltaic system,” *in IEEE Ind. Electron. Society Conf.*, pp. 1001-1006, October 2012.

[10] A. Kavimandan and S. P. Das, “Control and protection strategy for a three-phase single-stage boost type grid-connected current source inverter for PV applications,” in *Proc. IEEE ICIT Int. Conf.*, pp. 1722 – 1727, 2013.

[11] D. Shen and P. Lehn, "Modeling, analysis and control of a current source inverter-based STATCOM," *IEEE Trans. Power Del.*, vol. 17, no. 1, pp. 248 –253, January 2002.

[12] Y. W. Li, M. Pande, N. R. Zargari, B. Wu, "An input power factor control strategy for high-power current-source induction motor drive with active front-end," *IEEE Trans. Power Electronic.*, vol. 25, no. 2, pp. 352 – 359, February 2010.

[13] R. E. T.-Olguin, A. Garces, M. Molinas, and T. Undeland, "Integration of offshore wind farm using a hybrid HVDC transmission connected by the PWM current-source converter," *IEEE Trans. Energy Convers.*, vol. 28, no. 1, pp. 125-134, March 2013.

[14] J. S.-Bassols, A. E.-Alvarez, E. P.-Araujo, O. G.-Bellmunt, "Current source converter series tapping of a LCC-HVDC transmission system for integration of offshore wind power plants," in *Proc. 11th IET AC and DC Power Transmission Int. Conf.*, 2015.

[15] E. R.-Cadaval, G. Spagnuolo, L. G. Franquelo, C.-A. R.-Paja, T. Suntio, and W.-M. Xiao, "Grid-connected photovoltaic generation plants – components and operation," *IEEE Ind. Electron. Mag.*, vol. 7, no. 3, pp. 6-20, 2013.

[16] European Photovoltaic Industry Association, "Global market outlook – for photovoltaics 2014-2015," *EPIA Technical Report*, June 2014.

[17] F. Katiraei and J. R. Aguero, "Solar PV integration challenges," *IEEE Power & Energy Mag.*, vol. 9, no. 3, pp. 62 –71, 2011.

[18] S. Mishra, D. Ramasubramanian, and P. C. Sekhar, "A seamless control methodology for a grid connected and isolated PV-diesel microgrid," *IEEE Trans. Power Syst.*, vol. 28, no. 4, pp. 4393-4404, November 2013.

[19] A. Yazdani, A. R. Fazio, H. Ghoddami, M. Russo, M. Kazerani, J. Jatskevich, K. Strunz, S. Leva, and J. A. Martinez, "Modeling guidelines and a benchmark for power system simulation studies of three-phase single-stage photovoltaic system," *IEEE Trans. Power Del.*, vol. 26, no. 2, pp. 1247-1264, April 2011.

[20] L. Zhang, K. Sun, Y. Xing, L. Feng, and H. Ge, "A modular grid-connected photovoltaic generation system based on DC bus," *IEEE Trans. Power Electron.*, vol. 26, no. 2, pp. 523-531, February 2011.

[21] R. Carbone, "Grid-connected photovoltaic systems with energy storage," in *Proc. Clean Electrical Power Int. Conf.*, pp. 760-767, 2009.

[22] A. Yazdani and P. P. Dash, "A control methodology and characterization of dynamics for photovoltaic (PV) system interfaced with a distribution network," *IEEE Trans. Power Del.*, vol. 24, no. 3, pp. 1538 – 1551, July 2009.

[23] T. Messo, J. Jokiapii, J. Puukko, and T. Suntio, “Determining the value of the dc-link capacitance to ensure stable operation of a three-phase photovoltaic inverter,” *IEEE Trans. Power Electron.*, vol. 29, no. 2, pp. 665-673, February 2014.

[24] L. Nousiainen, J. Puukko, A. Maki, T. Messo, J. Huusari, J. Jokipii, J. Viinamaki, D. Lobera, S. Valkealahti, and T. Suntio, “Photovoltaic generator as an input source for power electronic converters,” *IEEE Trans. Power Electron.*, in press.

[25] M. A. Mahmud, H. R. Pota, and M. J. Hossain, “Dynamic stability of three-phase grid-connected photovoltaic system using zero dynamic design approach,” *IEEE J. Photovolt.*, vol. 2, no. 4, pp. 564-571, October 2012.

[26] E. Figueres, G. Garcerá, J. Sandia, F. G.- Espín, and J. C. Rubio, “Sensitivity study of the dynamics of three-phase photovoltaic inverters with an LCL grid filter,” *IEEE Trans. Ind. Electron.*, vol. 56, no. 3, pp. 706-717, March 2009.

[27] M. Hanif, V. Khadkikar, W. Xiao, and J. L. Kirtely, “Two degrees of freedom active damping technique for LCL filter-based grid connected PV systems,” *IEEE Trans. Ind. Electron.*, vol. 61, no. 6, pp. 2795-2803, June 2014.

[28] M. Salo and H. Tuusa, “A vector controlled current-source PWM rectifier with a novel current damping method,” *IEEE Trans. Power Electron.*, vol. 15, no. 3, pp. 464 – 470, May 2000.

[29] F. Liu, B. Wu, N. R. Zargari and M. Pande, “An active damping method using inductor-current feedback control for high-power PWM current-source rectifier,” *IEEE Trans. Power Electron.*, vol. 26, no. 9, pp. 2580 – 2587, 2011.

[30] J. C. Wiseman and B. Wu, “Active damping control of a high-power PWM current-source rectifier for line-current THD reduction,” *IEEE Trans. Ind. Electron.,* vol. 52, no. 3, pp. 758 – 764, June 2005.

[31] ABB, “ABB HiPak™ – IGBT Module 5SNA 1200G450300,” 5SYA 1401-03 04-2012 datasheet, pp. 1-9, 2012.

[32] R. Lai, F. Wang, P. Ning, D. Zhang, D. Jiang, R. Burgos, D. Boroyevich, K. J. Karimi, And V. D. Immanuel, “A high-power-density converter,” *IEEE Ind. Electron. Mag.*, vol. 4, iss. 4, pp. 4-12, Dec. 2010.

[33] M. Bahrman and K. Johnson, “The ABCs of HVDC transmission technology,” *IEEE Power Energy Magazine*, vol. 5, iss. 2, pp. 32-44, 2007.

[34] S. M. Muyeen, R. Takahashi, and J. Tamura, “Operation and control of HVDC-connected offshore wind farm,” *IEEE Trans. Sust. Energy*, vol. 1, no. 1, pp. 30-37, April 2010.

[35] T. Ackermann, K. Garner, A. Gardiner, "Embedded wind generation in weak grids – economic optimization and power quality simulation," *Renew Energ*, volume 18, iss. 2, pp. 205-221, Oct. 1999.

[36] L. Zhang, L. Harnefors, and H.-P. Nee, "Interconnection of two very weak ac systems by VSC-HVDC links using power-synchronization control," *IEEE Trans. Power Syst.*, vol. 26, no. 1, pp. 344-355, Feb. 2011.

[37] A. E.-Alvarez, S. Fekriasl, F. Hassan, and O. G.-Bellmunt, "Advanced vector control for voltage source converters connected to weak grids," *IEEE Trans. Power Syst.*, in press.

[38] L. Harnefors, M. Bongiorno, and S. Lundberg, "Input-admittance calculation and shaping for controlled voltage-source converters," *IEEE Trans. Ind. Electron.*, vol. 54, no. 6, pp. 3323-3334, Dec. 2007.

[39] B. Wen, D. Boroyevich, R. Burgos, P. Mattavelli, and Z. Shen, "Analysis of D-Q small-signal impedance of grid-tied inverters," *IEEE Trans. on Power Electron.*, in press.

[40] D. Dong, B. Wen, D. Boroyevich, P. Mattavelli, and Y. Xue, "Analysis of phase-locked loop low-frequency stability in three-phase grid-connected power converters considering impedance interactions," *IEEE Trans. Ind. Electron.*, vol. 62, no. 1, pp. 310-321, Jan. 2015.

[41] Y. Huang, X. Yuan, J. Hu, P. Zhou, "Modeling of VSC connected to weak grid for stability analysis of DC-Link voltage control," *IEEE J. Emerg. Sel. Topics Power Electron.*, in press.

[42] J. Zhou, D. Hui, S. Fan, Y. Zhang, and A. M. Gole, "Impact of short-circuit ratio and phase-locked-loop parameters on the small-signal behavior of a VSC-HVDC converter," *IEEE Trans. Power Del.*, vol.29, no.5, pp.2287-2296, Oct. 2014.

[43] M. Durrant, H. Werner, and K. Abbott, "Model of a VSC HVDC terminal attached to a weak ac system," in *Proc. IEEE Control Applications Conf.*, vol. 1, pp. 178-182, June 2003.

[44] L. Zhang, L. Harnefors, and H.-P. Nee, "Power-synchronization control of grid-connected voltage-source converters," *IEEE Trans. on Power Syst.*, vol. 25, no. 2, pp. 809-820, May 2010.

[45] J. Sun, "Impedance-based stability criterion for grid-connected inverters," *IEEE Trans. Power Electron.*, vol. 26, no. 11, pp. 3075-3078, Nov. 2011.

[46] G. Liu, Y. Yang, P. Wang, W. Wang, D. Xu, "Stability control method based on virtual inductance of grid-connected PV inverter under weak grid," *in Proc. IEEE Ind. Electron. Society Conf.*, pp. 1867-1872, 2013.

[47] D. Yang, X. Ruan, and H. Wu, "Impedance shaping of the grid-connected inverters with LCL filter to improve its adaptability to the weak grid condition," *IEEE Trans. Power Electron.*, vol. 29, no. 11, pp. 5795-5805, Nov. 2014.

[48] J. Xu, S. Xie, T. Tang, "Improved control strategy with grid-voltage feedforward for LCL-filter-based inverter connected to weak grid," *IET Power Electron.*, vol. 7, iss. 10, pp. 2660-2671, 2014.

[49] IEEE 1547 Standard for Interconnecting Distributed Resources with Electric Power Systems, Oct. 2003.

[50] UL 1741 Standard for Inverters, Converters, Controllers and Interconnection System Equipment for Use with Distributed Energy Resources.

[51] S. Eftekharnejad, V. Vittal, G. T. Heydt, B. Keel, and J. Loehr, "Small signal stability assessment of power systems with increased penetration of photovoltaic generation – a case study," *IEEE Trans. Sust. Energy*, vol. 4, no. 4, pp. 960-967, 2013.

[52] M. Fazeli, J. B. Ekanayake, P. M. Holland, and P. Igic, "Exploiting PV inverters to support local voltage – a small-signal model," *IEEE Trans. on Energy Convers.*, vol. 29, no. 2, pp. 453-462, June 2014.

[53] W. Xiao, W. G. Dunford, P. R. Palmer, and A. Capel, "Regulation of photovoltaic voltage," *IEEE Trans. Ind. Electron.*, vol. 54, no. 3, pp. 1365-1374, 2007.

[54] R. G. Wandhare and V. Agarwal, "Precise active and reactive power control of the PV-DGS integrated with weak grid to increase PV penetration," in *Proc. IEEE Photovoltaic Specialist Conf.*, pp. 3150-3155, 2014.

[55] S. Eftekharnejad, V. Vittal, G. T. Heydt, B. Keel, and J. Loehr, "Impact of increased penetration of photovoltaic generation on power systems," *IEEE Trans. Power Syst.*, vol. 28, no. 2, pp. 893-901, 2013.

[56] B. Tamimi, C. Cañizares, and K. Bhattacharya, "System stability impact of large-scale and distributed solar photovoltaic generation – the case of Ontario, Canada," *IEEE Trans. Sust. Energy*, vol. 4, no. 3, pp. 680-688, 2013.

[57] K. M. Alawasa and Y. A.-R. I. Mohamed, "Impedance and damping characteristics of grid-connected VSCs with power synchronization control strategy," *IEEE Trans. Power Syst.*, vol. 30, no. 2, pp. 952-961, 2015.

[58] K. M. Alawasa, Y. A.-R. I. Mohamed, and W. Xu, "Active mitigation of subsynchronous interactions between PWM voltage-source converters and power networks," *IEEE Trans. Power Electron.*, vol. 29, no. 1, pp. 121-134, 2014.

[59] D. Boroyevich, I. Cvetković, D. Dong, R. Burgos, F. Wang, and F. Lee, "Future electronic power distribution systems – a contemplative view," in *Proc. OPTIM Int. Conf.*, pp. 1369-1380, 2010.

[60] T. L. Vandoorn, B. Meersman, J. D. M. De Kooning, and L. Vandevelde, "Transition from islanded to grid-connected mode of microgrids with voltage-based droop control," *IEEE Trans. Power Syst.*, vol. 28, no. 3, pp. 2545-2553, 2013.

[61] D. Salomonsson, L. Söder, and A. Sannino, "Protection of low-voltage dc microgrids," *IEEE Trans. Power Del.*, vol. 24, no. 3, pp. 1045-1053, July 2009.

[62] M. Saeedfard, M. Graovac, R.F. Dias, and R. Iravani, "DC power systems – challenges and opportunities," in *Proc. IEEE Power and Energy Society General Meeting*, pp. 1-7, 2010.

[63] M. Davari, and Y. A.-R. I. Mohamed, "Robust multi-objective control of VSC-based dc-voltage power port in hybrid ac/dc multi-terminal micro-grids," *IEEE Trans. Smart Grids*, vol. 4, no. 3, pp. 1597-1612, September 2013.

[64] M. Akbari, M. A. Golkar, and S. M. M. Tafreshi, "A PSO solution for improved voltage stability of a hybrid ac-dc microgrid," in *Proc. IEEE PES ISGT Conf.*, 2011.

[65] K-N. Areerak, S. V. Bozhko, G. M. Asher, L. De. Lillo, D. W. P. Thomas, "Stability study for a hybrid ac-dc more-electric aircraft power system," *IEEE Trans. Aerosp. Electron. Syst.*, vol. 48, no. 1, pp. 329-347, January 2012.

[66] A. Radwan and Y. Mohamed, "Assessment and mitigation of interaction dynamics in hybrid ac/dc distribution generation systems," *IEEE Trans. Smart Grid*, vol. 3, no. 3, pp. 1382-1393,September 2012.

[67] K. Kurohane, T. Senjyu, A. Yona, N. Urasaki, T. Goya, and T. Funabashi, "A hybrid smart ac/dc power system," *IEEE Trans. Smart Grid*, vol. 1, no. 2, pp. 199-204, September 2010.

[68] A. Ghazanfari, M. Hamzeh, H. Mokhtari, and H. Karimi, "Active power management of multihybrid fuel cell/supercapacitor power conversion system in a medium voltage microgrid," *IEEE Trans. Smart Grid*, vol. 3, no. 4, pp. 1903-1910, December 2012.

[69] P. C. Loh, D. Li, Y. K. Chai, and F. Blaabjerg, "Autonomous operation of ac-dc microgrids with minimized interlinking energy flow," *IET Power Electron.*, vol. 6, no. 8, pp. 1650-1657, 2013.

[70] P. C. Loh, D. Li, Y. K. Chai, and F. Blaabjerg, "Hybrid ac-dc microgrids with energy storages and progressive energy flow tuning," *IEEE Trans. Power Electron.*, vol. 28, no. 4, pp. 1533-1543, April 2013.

[71] P. C. Loh, D. Li, Y. K. Chai, and F. Blaabjerg, "Autonomous operation of hybrid microgrid with ac and dc subgrids," *IEEE Trans. Power Electron.*, vol. 28, no. 5, pp. 2214-2223, May 2013.

[72] P. C. Loh and F. Blaabjerg, "Autonomous control of interlinking converter with energy storage in hybrid ac-dc microgrid," *IEEE Trans. Ind. Appl.*, in press.

[73] J. M. Guerrero, P. C. Loh, T.-L. Lee, and M. Chandorkar, "Advanced control architecture for intelligent microgrids – part II: power quality, energy storage, and ac/dc microgrids," *IEEE Trans. Ind. Electron.*, vol. 60, no. 4, pp. 1263-1270, April 2013.

[74] N. Eghtedarpour and E. Farjah, "Power control and management in a hybrid ac/dc microgrid," *IEEE Trans. Smart Grid*, vol. 5, no. 3, pp. 1494– 1505, May 2014.

[75] R. Majumder, "A hybrid microgrid with dc connection at back to back converters," *IEEE Trans. Smart Grid*, in press.

[76] B. I. Rani, G. S. Ilango, and C. Nagamani, "Control strategy for power flow management in a PV system supplying dc loads," *IEEE Trans. Ind. Electron.*, vol. 60, no. 8, pp. 3185-3194, August 2013.

[77] L. N. Khanh, J.-J. Seo, Y.-S. Kim, and D.-J. Won, "Power-management strategies for a grid-connected PV-FC hybrid system," *IEEE Trans. Power Del.*, vol. 25, no. 3, pp. 1874-1882, July 2010.

[78] B. Belvedere, M. Bianchi, A. Borghetti, C. A. Nucci, M. Paolone, and A. Peretto, "A microcontroller-based power management system for standalone microgrids with hybrid power supply," *IEEE Trans. Sust. Energy*, vol. 3, no. 3, pp. 422-431, July 2012.

[79] B. Dong, Y. Li, Z. Zheng, and L. Xu, "Control strategies of microgrid with hybrid dc and ac buses," in *Proc. European Conf. on Power Electron. Appl.*, pp. 1-8, 2011.

[80] X. Liu, P. Wang, and P. C. Loh, "A hybrid ac/dc microgrid and its coordinated control," *IEEE Trans. Smart Grid*, vol. 2, no. 2, pp. 278-286, June 2011.

[81] S. Grillo, V. Musolino, L. Piegari, E. Tironi, and C. Tornelli, "DC islanded in ac smart grids," *IEEE Trans. Power Electron.*, vol. 29, no. 1, pp. 89-98, January 2014.

[82] E. Alegria, T. Brown, E. Minear, and R. H. Lasseter, "CERTS microgrid demonstration with large-scale energy storage and renewable generation," *IEEE Trans. Smart Grid*, in press.

[83] M. N. Ambia, A. Al-Durra, and S. M. Muyeen, "Centralized power control strategy for ac-dc hybrid microgrid system using multi-converter scheme," *in Proc. IEEE IECON*, pp. 843-848, 2011.

[84] M. Sechilariu, B. Wang, and F. Locment, "Building integrated photovoltaic system with energy storage and smart grid communication," *IEEE Trans. Ind. Electron.*, vol. 60, no. 44, pp. 1607-1618, April, 2013.

[85] T. Dragicevic, J. M. Guerrero, J. C. Vasquez, and D. Skrlec, "Supervisory control of an adaptive-droop regulated dc microgrid with battery management capability," *IEEE Trans. Power Electron.*, vol. 29, no. 2, pp. 695-706, February 2014.

[86] X. Lu, J. M. Guerrero, K. Sun, J. C. Vasquez, R. Teodorescu, and L. Huang, "Hierarchical control of parallel ac-dc converter interfaces for hybrid microgrids," *IEEE Trans. Smart Grid*, in press.

[87] J. M. Guerrero, J. C. Vasquez, J. Matas, L. G. de Vicuña, and M. Castilla, "Hierarchical control of droop-controlled ac and dc microgrids – a general approach toward standardization," *IEEE Trans. Ind. Electron.*, vol. 58, no. 1, pp. 158-172, January 2011.

[88] Y. Zhang, and H. Ma, "Theoretical and experimental investigation of networked control of parallel operation of inverters," *IEEE Trans. Ind. Electron.*, vol. 59, no. 4, pp. 1961-1970, April 2012.

[89] S. Anand, B. G. Fernandes, and J. M. Guerrero, "Distributed control to ensure proportional load sharing and improve voltage regulation in low voltage dc microgrid," *IEEE Trans. Power Electron.*, vol. 28, no. 4, pp. 1900-1913, April 2013.

[90] Y. Mohamed and A. Radwan, "Hierarchical control system for robust microgrid operation and seamless mode transfer in active distribution systems," *IEEE Trans. Smart Grid*, vol. 2, no. 2, pp. 352 – 362, June 2011.

[91] Y. Mohamed and E. El-Saadany,"Adaptive decentralized droop controller to preserve power sharing stability of paralleled inverters in distributed generation microgrids," *IEEE Trans. Power Electron.,* vol. 23, no. 6, pp. 2806-2816, 2008.

[92] C. Taylor, *Power System Voltage Stability*. New York: McGraw-Hill, 1994.

[93] B. M. Nomikos and C. D. Vournas, "Investigation of induction machine contribution to power system oscillations," *IEEE Trans. Power Syst.*, vol.20, no.2, pp. 916- 925, May 2005.

[94] P. Krause, O. Wasynczuk and S. Sudhoff, *Analysis of Electric Machinery and Drive Systems*, 2nd Edition, John Wiley and Sons, 2002.

[95] R. Turner, S. Walton and R. Duke, "A case study on the application of the nyquist stability criterion as applied to interconnected loads and sources on grids," *IEEE Trans. Ind. Electron.*, vol. 60, no. 7, pp. 2740-2749, 2013.

[96] N. Bottrell, M. Prodanovic and T. C. Green, "Dynamic stability of a microgrid with an active load," *IEEE Trans. Power Electron.*, in press.

[97] A. Radwan and Y. Mohamed, "Modeling, analysis, and stabilization of converter-fed ac microgrids with high penetration of converter-interfaced loads," *IEEE Trans. Smart Grid*, vol. 3, no. 3, pp. 1213-1225, 2012.

[98] A. Radwan and Y. Mohamed, "Analysis and active-impedance-based stabilization of voltage-source-rectifier loads in grid-connected and isolated microgrid applications," *IEEE Trans. Sust. Energy*, in press.

[99] G. Diaz, C. G.-Moran, J.G.-Aleixandre and A. Diez, "Composite loads in stand-alone inverter-based microgrids – modeling procedure and effects on load margin," *IEEE Trans. Power Syst.*, vol. 25, no. 2, pp. 894 –905, May 2010.

[100] M. Cespedes, L. Xing and J. Sun, "Constant-power load system stabilization by passive damping," *IEEE Trans. Power Electron.*, vol. 26, no. 7, pp. 1832 – 1836, Jul. 2011.

[101] Mitsubishi, "*PV-UD190MF5*". USA: Mitsubishi, 2007.

[102] T. Esram and P. L. Chapman, "Comparison of photovoltaic array maximum power point tracking techniques," *IEEE Trans. Energy Convers.*, vol. 22, no. 2, pp. 439-449, June 2007.

[103] A. Kahrobaeian, and Y. Mohamed, "Robust single-loop direct current control of LCL-filtered converter-based DG units in grid-connected and autonomous microgrid modes," *IEEE Trans. Power Electron,* vol.29, no.10, pp.5605-5619, Oct. 2014.

[104] P. Mitra, L. Zhang, and L. Harnefors, "Offshore wind integration to a weak grid by VSC-HVDC links using power-synchronization control – a case study," *IEEE Trans. Power Del.*, vol. 29, no. 1, pp. 453-461, 2014.

[105] N.-S. Choi, K.-W. Lee, and B.-M. Han, "A novel carrier based PWM for current source converter," in *Proc. IPEMC Conf.*, pp. 1945-1950, 2012.

[106] Z. Bai, H. Ma, D. Xu, B. Wu, Y. Fang, and Y. Yao, "Resonance damping and harmonic suppression for grid-connected current-source converter," *IEEE Trans. Ind. Electron.*, vol. 6, no. 7, pp. 3146-3154, July 2014.

[107] A. Yazdani and R. Iravani, *Voltage-Sourced Converters in Power Systems – Modeling, Control, and Applications*. Hoboken, New Jersey: John Wiley & Sons, 2010.

[108] Y. Ye, M. Kazerani, and V. H. Quintana, "Current-source converter based STATCOM – Modeling and control," *IEEE Trans. Power Del*. Vol. 20, no. 2, pp. 795-800, April 2005.

[109] *IEEE Recommended Practice for Industrial and Commercial Power System Analysis*, IEEE Standard 399-1997.

[110] M. Belkhayat, "Stability criteria for AC power systems with regulated loads," PhD thesis, Purdue Univ., West Lafayette, IN, USA, 1997.

[111] J. Maciejowski, *Multivariable Feedback Design*, Addision-Wesley, 1989.

[112] C. H.-Aramburo, T. Green, and N. Mugniot, "Fuel consumption minimization of a microgrid," *IEEE Trans. Ind. Appl.*, vol. 41, no. 3, pp. 673-681, 2005.

[113] E. Barklund, N. Pogaku, M. Prodanovic´, C. H.-Aramburo, and T. Green, "Energy management in autonomous microgrid using stability-constrained droop control of inverters," *IEEE Trans. Power Electron.*, vol. 23, no. 5, pp. 2346-2352, 2008.

[114] I. Nutkani, P. Loh, and F. Blaabjerg, "Droop scheme with consideration of operating cost," *IEEE Trans. Power Electron.*, vol. 29, no. 3, pp. 1047-1052, 2014.

[115] M. Ghazvini, Z. Vale, H. Morais, and B. Canizes, "A regulatory framework for short-term stochastic maintenance outage scheduling in smart grids," in *Proc. IEEE ISGT Europe Int. Conf.*, 2012.

[116] A. C.-Subirachs, A. R.-Alvarez, O. G.-Bellmunt, F. A.-C.-Figuerola, and A. S.-Andreu, "Centralized and distributed active and reactive power control of a utility connected microgrid using IEC61850," *IEEE Syst. J.*, vol. 6, no. 1, pp. 58-67, 2012.

Appendices

Appendix A3

A3.1 CSC Parameters

0.5 MVA, $4160\,V$, $R_s = 0.85\Omega$, $L_s = 4.6\,mH$, $C_s = 60\mu F$, $K_p^{dc} = 0.001, K_i^{dc} = 6.7, K_p^{ac} = 1, K_i^{ac} = 660$.

A3.2 PV Generator Parameters

$R_{dc} = 0.2\Omega$, $L_{dc} = 70mH$, $C_{dc} = 5000\mu F$, $I_{or} = 0.12\,\mu A$, $I_{sc} = 10\,A$, $I_{dc} = 200\,A$, $n_s = 50$, $N_s = 600$, $n_p = 750$, $A = 1.92$, $T = T_r = 300$ Kelvin, $\alpha_i = 0.002$ A/kelvin, $G = 1\,kW/m^2$, $q = 1.602 \times 10^{-19} c$, $K = 1.38 \times 10^{-23}$ J/Kelvin.

A3.3 Uncompensated dc-Side impedance ($\Delta \boldsymbol{Z_{csc}(s)}$)

$$K_{dc}(s) = sL_{dc} + R_{dc} - \frac{3}{2} m_d^{\circ} \frac{V_{sd}^{\circ}}{I_{dc}^{\circ}}$$

$$K_d(s) = \frac{3}{2}\left(s^2\left(L_s C_s \frac{V_{sd}^{\circ}}{I_{dc}^{\circ}}\right) + s\left(m_d^{\circ} L_s + R_s C_s \frac{V_{sd}^{\circ}}{I_{dc}^{\circ}}\right) + m_d^{\circ} R_s + m_q^{\circ} \omega^{\circ} L_s + (1 - \omega^{\circ 2} L_s C_s) \frac{V_{sd}^{\circ}}{I_{dc}^{\circ}}\right)$$

$$K_q(s) = -\frac{3}{2}\left(s\left(2\omega^{\circ} L_s C_s \frac{V_{sd}^{\circ}}{I_{dc}^{\circ}} - m_q^{\circ} L_s\right) + m_d^{\circ} \omega^{\circ} L_s - m_q^{\circ} R_s + \omega^{\circ} R_s C_s \frac{V_{sd}^{\circ}}{I_{dc}^{\circ}}\right)$$

$$K_{dq}(s) = \frac{sC_s R_a H(s) \omega^{\circ} L_s}{sC_s(R_s + sL_s)(1 - R_a H(s)) + G_{ac}(s) + 1}$$

$$K_{ddc}(s) = \frac{-G_{ac}(s) G_{dc}(s)}{sC_s(R_s + sL_s)(1 - R_a H(s)) + G_{ac}(s) + 1 + sC_s R_a H(s) \omega^{\circ} L_s K_{dq}(s)}$$

A3.4 DC-Side Current-Based Compensated Impedance ($\Delta \boldsymbol{Z_{csc}^n}$)

$$K_{ddc}^n(s) = \frac{\big(C_m(s) - (C_o(s) + 1) G_{dc}(s)\big) G_{ac}(s) + C_i(s)}{sC_s(R_s + sL_s)(1 - R_a H(s)) + G_{ac}(s) + 1 + sC_s R_a H(s) \omega^{\circ} L_s K_{dq}(s)}$$

A3.5 DC-Side Error-Based Compensated Impedance ($\Delta \boldsymbol{Z_{csc}^e}$)

$$K_{ddc}^e(s) = \frac{-\frac{Y_C}{s\,C_{dc}} - G_{ac}(s) G_{dc}(s)}{sC_s(R_s + sL_s)(1 - R_a H(s)) + G_{ac}(s) + 1 + sC_s R_a H(s) \omega^{\circ} L_s K_{dq}(s)}$$

Appendix A4

A4.1 System Parameters

CSC: $1\ MVA$, $F_{sw} = 1980\ Hz$, $C_f = 300\ \mu F$, $L_{dc} = 5\ mH$, $K_d = 1.0$,$K_\delta = 0.5 \times 10^{-6}$, $G_i(s) = 3 + 100/s$, $G_v(s) = 0.001 + 100/s$.

Utility-Grid: 13800 V, $60\ Hz$, $X/R\ ratio = 20$, $SCR = 5$.

PV Generator: $N_s = 460$, $N_p = 410$, $n_s = 50$, $A = 1.25$, $R_s = 0.2231\ \Omega$, $R_{sh} = 1011.15\ \Omega$, $I_{or} = 38.061\ nA$, $T = 298\ K$.

A4.2 Small-Signal Modeling of the Grid-Connected CSC-Based PV Generator with the PSC

- Frame Transformation

$$T_{\delta v} = \begin{bmatrix} V_q^\circ & -V_d^\circ \end{bmatrix}^T, T_{\delta i} = \begin{bmatrix} I_q^\circ & -I_d^\circ \end{bmatrix}^T, T_{\delta iw} = \begin{bmatrix} I_{wq}^\circ & -I_{wd}^\circ \end{bmatrix}^T.$$

- Small-Signal Model of the Power Circuit in (4.1) and (4.3)

$$\begin{bmatrix} \Delta \dot{V_d} \\ \Delta \dot{V_q} \\ \Delta \dot{I}_{dc}^2 \end{bmatrix} = \underbrace{\begin{bmatrix} 0 & \omega^\circ & 0 \\ -\omega^\circ & 0 & 0 \\ \frac{-3I_d^\circ}{L_{dc}} & \frac{-3I_q^\circ}{L_{dc}} & \frac{V_{dc}^\circ}{I_{dc}^\circ L_{dc}} \end{bmatrix}}_{A_p} \begin{bmatrix} \Delta V_d \\ \Delta V_q \\ \Delta I_{dc}^2 \end{bmatrix} + \underbrace{\begin{bmatrix} -1/C_f & 0 \\ 0 & -1/C_f \\ \frac{-3V_d^\circ}{L_{dc}} & \frac{-3V_q^\circ}{L_{dc}} \end{bmatrix}}_{B_{p1}} \begin{bmatrix} \Delta I_d \\ \Delta I_q \end{bmatrix} + \underbrace{\begin{bmatrix} 1/C_f & 0 \\ 0 & 1/C_f \\ 0 & 0 \end{bmatrix}}_{B_{p2}} \begin{bmatrix} \Delta I_{wd} \\ \Delta I_{wq} \end{bmatrix} +$$

$$\underbrace{\begin{bmatrix} 0 \\ 0 \\ \frac{2I_{dc}^\circ}{L_{dc}} \end{bmatrix}}_{B_{p3}} \Delta V_{dc}.$$

- Small-Signal Model of the Power Controller in (4.4)

$$\Delta \dot{\delta} = k_\delta \Delta P^* \underbrace{-1.5k_\delta \begin{bmatrix} I_d^\circ & I_q^\circ \end{bmatrix}}_{B_{\delta v}} \begin{bmatrix} \Delta V_d^c \\ \Delta V_q^c \end{bmatrix} \underbrace{-1.5k_\delta \begin{bmatrix} V_d^\circ & V_q^\circ \end{bmatrix}}_{B_{\delta i}} \begin{bmatrix} \Delta I_d^c \\ \Delta I_q^c \end{bmatrix}$$

- **Small-Signal Model of the Voltage Controller in (4.6)**

$$\Delta\dot{\varphi_v} = \underbrace{-\frac{k_{iv}}{V^\circ}\begin{bmatrix} V_d^\circ & V_q^\circ \end{bmatrix}}_{B_v}\begin{bmatrix}\Delta V_d^c \\ \Delta V_q^c\end{bmatrix} + k_{iv}\Delta V^*,$$

$$\begin{bmatrix}\Delta I_{wd}^c \\ \Delta I_{wq}^c\end{bmatrix} = \underbrace{\begin{bmatrix}1 \\ 0\end{bmatrix}}_{C_v}\Delta\varphi_v + \underbrace{\begin{bmatrix} -\frac{V_d^\circ k_{pv}}{V^\circ} - k_d & -\frac{V_q^\circ k_{pv}}{V^\circ} \\ 0 & -k_d \end{bmatrix}}_{D_{v1}}\begin{bmatrix}\Delta V_d^c \\ \Delta V_q^c\end{bmatrix} + \underbrace{\begin{bmatrix}k_{pv} \\ 0\end{bmatrix}}_{D_{v2}}\Delta V^*.$$

- **State-Space Model in (4.9)**

$$A_{in} = \begin{bmatrix} A_p + [B_{p2}D_{v1} \quad 0_{3\times1}] & B_{p2}C_v & B_{p2}(D_{v1}T_{\delta v} - T_{\delta iw}) \\ [B_v \quad 0] & 0 & B_v T_{\delta v} \\ [B_{\delta v} \quad 0] & 0 & B_{\delta v}T_{\delta v} + B_{\delta i}T_{\delta i} \end{bmatrix}$$

$B_{inp} = [0_{3\times1} \quad 0 \quad k_\delta]^T$, $B_{inv} = [B_{p2}D_{v2} \quad k_{iv} \quad 0]^T$, $B_{indc} = [B_{p3} \quad 0 \quad 0]^T$, $B_{ini} = [B_{p1} \quad 0_{1\times2} \quad B_{\delta i}]^T$.

- **Closed-Loop Transfer Functions in (4.10)-(4.11)**

$$A_{cl} = \begin{bmatrix} A_{in} + [0_{5\times2} \quad B_{indc}G_{pv} \quad 0_{5\times2}] & B_{ini} \\ [B_g \quad 0_{2\times3}] & A_g \end{bmatrix}, B_{clv} = \begin{bmatrix} B_{inv} \\ 0_{2\times1}\end{bmatrix}, B_{clp} = \begin{bmatrix} B_{inp} \\ 0_{2\times1}\end{bmatrix}.$$

$C_{clp} = 1.5[I_d^\circ \quad I_q^\circ \quad 0 \quad 0 \quad 0 \quad V_d^\circ \quad V_q^\circ]$, $C_{clv} = [\frac{V_d^\circ}{V^\circ} \quad \frac{V_q^\circ}{V^\circ} \quad 0_{1\times5}]$.

- **State-Space Model in (4.13)**

$$A_z = \begin{bmatrix} A_{in} + \begin{bmatrix} 0_{5\times2} & \begin{pmatrix} B_{inp}k_{pi} \\ +B_{indc}G_{pv}\end{pmatrix} & 0_{5\times2}\end{bmatrix} & B_{inp} \\ [0 \quad 0 \quad k_{ii} \quad 0 \quad 0] & 0 \end{bmatrix}, B_z = \begin{bmatrix} B_{ini} \\ 0_{1\times2}\end{bmatrix}, C_z = \begin{bmatrix} 1 & 0 & 0_{1\times4} \\ 0 & 1 & 0_{1\times4}\end{bmatrix}, \text{where}$$

$$G_{pv} = -\frac{1}{2I_{dc}^\circ}\left(\frac{N_s}{N_p}\right)\left(\frac{n_s V_t R_{sh}}{I^\circ R_{sh} exp\{V_D^\circ/n_s V_t\} + n_s V_t} + R_s\right).$$

- **State-Space Model of the Utility-Grid in (4.2)**

$$\begin{bmatrix}\Delta\dot{I_d} \\ \Delta\dot{I_q}\end{bmatrix} = \underbrace{\begin{bmatrix} -R_g/L_g & \omega^\circ \\ -\omega^\circ & -R_g/L_g\end{bmatrix}}_{A_g}\begin{bmatrix}\Delta I_d \\ \Delta I_q\end{bmatrix} + \underbrace{\begin{bmatrix} 1/L_g & 0 \\ 0 & 1/L_g\end{bmatrix}}_{B_g}\begin{bmatrix}\Delta V_d \\ \Delta V_q\end{bmatrix}.$$

- **Final State-Space Model in (4.15)**

$$A_{tot} = \begin{bmatrix} A_{cl} + [0_{7\times2} \quad B_{clp}k_{pi} \quad 0_{7\times4}] & B_{clp} \\ [0_{1\times2} \quad k_{ii} \quad 0_{1\times4}] & 0 \end{bmatrix}$$

Appendix A5

A5.1 System Parameters

CSC: 1 MVA, 13.8 kV, $F_{sw} = 1980$ Hz ,$C_f = 200\ \mu F$, $\mathrm{G}_i(s) = 10^{-4} + (400/s)$, $\mathrm{G}_v(s) = 10^{-3} + (7.5/s)$, $\mathrm{G}_\delta(s) = 180 + (3200/s)$, k = 0.3.

Utility-Grid: 36 MVA, 13.8 kV, 60 Hz, XR = 7.0.

A5.2 Small-Signal Modeling of the Grid-Connected CSC

- PLL Model

$$\begin{bmatrix} \Delta\dot{\delta} \\ \Delta\dot{\varphi}_\delta \end{bmatrix} = \underbrace{\begin{bmatrix} 0 & 1 \\ 0 & 0 \end{bmatrix}}_{A_\delta} \begin{bmatrix} \Delta\delta \\ \Delta\varphi_\delta \end{bmatrix} + \underbrace{\begin{bmatrix} 0 & K_{p\delta}/V_d^\circ \\ 0 & K_{i\delta}/V_d^\circ \end{bmatrix}}_{B_\delta} \begin{bmatrix} \Delta V_d^c \\ \Delta V_q^c \end{bmatrix},$$

$$\Delta\omega = \underbrace{\begin{bmatrix} 0 & 1 \end{bmatrix}}_{C_\delta} \begin{bmatrix} \Delta\delta \\ \Delta\varphi_\delta \end{bmatrix} + \underbrace{\begin{bmatrix} 0 & K_{p\delta}/V_d^\circ \end{bmatrix}}_{D_\delta} \begin{bmatrix} \Delta V_d^c \\ \Delta V_q^c \end{bmatrix}.$$

- Frame Transformation

$$\begin{bmatrix} \Delta V_d^c \\ \Delta V_q^c \end{bmatrix} = \begin{bmatrix} \Delta V_d \\ \Delta V_q \end{bmatrix} + \underbrace{\begin{bmatrix} V_q^\circ \\ -V_d^\circ \end{bmatrix}}_{\delta_v} \Delta\delta, \begin{bmatrix} \Delta I_d^c \\ \Delta I_q^c \end{bmatrix} = \begin{bmatrix} \Delta I_d \\ \Delta I_q \end{bmatrix} + \underbrace{\begin{bmatrix} I_q^\circ \\ -I_d^\circ \end{bmatrix}}_{\delta_i} \Delta\delta,$$

$$\begin{bmatrix} \Delta I_{wd}^c \\ \Delta I_{wq}^c \end{bmatrix} = \begin{bmatrix} \Delta I_{wd} \\ \Delta I_{wq} \end{bmatrix} + \underbrace{\begin{bmatrix} I_{wq}^\circ \\ -I_{wd}^\circ \end{bmatrix}}_{\delta_{iw}} \Delta\delta.$$

- Power Circuit Model

$$\begin{bmatrix} \Delta\dot{V}_d \\ \Delta\dot{V}_q \end{bmatrix} = \underbrace{\begin{bmatrix} 0 & \omega^\circ \\ -\omega^\circ & 0 \end{bmatrix}}_{A_p} \begin{bmatrix} \Delta V_d \\ \Delta V_q \end{bmatrix} + \underbrace{\begin{bmatrix} -1/C_f & 0 \\ 0 & -1/C_f \end{bmatrix}}_{-B_p} \begin{bmatrix} \Delta I_d \\ \Delta I_q \end{bmatrix} + \begin{bmatrix} B_p \end{bmatrix} \begin{bmatrix} \Delta I_{wd} \\ \Delta I_{wq} \end{bmatrix}.$$

$$\begin{bmatrix} \Delta\dot{I}_d \\ \Delta\dot{I}_q \end{bmatrix} = \underbrace{\begin{bmatrix} -R_g/L_g & \omega^\circ \\ -\omega^\circ & -R_g/L_g \end{bmatrix}}_{A_g} \begin{bmatrix} \Delta I_d \\ \Delta I_q \end{bmatrix} + \underbrace{\begin{bmatrix} 1/L_g & 0 \\ 0 & 1/L_g \end{bmatrix}}_{B_g} \begin{bmatrix} \Delta V_d \\ \Delta V_q \end{bmatrix}$$

- **Current Control Model**

$$\begin{bmatrix}\Delta\dot{\varphi}_{id}\\ \Delta\dot{\varphi}_{iq}\end{bmatrix} = \underbrace{\begin{bmatrix}K_{ii} & 0\\ 0 & K_{ii}\end{bmatrix}}_{B_i}\begin{bmatrix}\Delta I_d^*\\ \Delta I_q^*\end{bmatrix} - [B_i]\begin{bmatrix}\Delta I_d^c\\ \Delta I_q^c\end{bmatrix},$$

$$\begin{bmatrix}\Delta I_{wd}^c\\ \Delta I_{wq}^c\end{bmatrix} = \begin{bmatrix}\Delta\varphi_{id}\\ \Delta\varphi_{iq}\end{bmatrix} + \underbrace{\begin{bmatrix}K_{pi} & 0\\ 0 & K_{pi}\end{bmatrix}}_{D_i}\begin{bmatrix}\Delta I_d^*\\ \Delta I_q^*\end{bmatrix} - [D_i]\begin{bmatrix}\Delta I_d^c\\ \Delta I_q^c\end{bmatrix} + \underbrace{\begin{bmatrix}-k & -\omega^{\circ} C_f\\ \omega^{\circ} C_f & -k\end{bmatrix}}_{D_{i1}}\begin{bmatrix}\Delta V_d^c\\ \Delta V_q^c\end{bmatrix}.$$

- **Outer Loop Model**

$$\Delta\dot{\varphi}_v = \underbrace{[K_{iv} \quad 0]}_{B_o}\begin{bmatrix}\Delta V_d^c\\ \Delta V_q^c\end{bmatrix}, \begin{bmatrix}\Delta I_d^*\\ \Delta I_q^*\end{bmatrix} = \underbrace{\begin{bmatrix}0\\ 1\end{bmatrix}}_{C_o}\Delta\varphi_v + \underbrace{\begin{bmatrix}\frac{-P^*}{1.5V_d^{\circ 2}} & 0\\ K_{pv} & 0\end{bmatrix}}_{D_o}\begin{bmatrix}\Delta V_d^c\\ \Delta V_q^c\end{bmatrix} - \begin{bmatrix}\Delta y_d\\ \Delta y_q\end{bmatrix}.$$

- **Active Compensation Model**

$$A_c = \begin{bmatrix}-2\xi_d\omega_d & -2\xi_d\omega_d k_d & 0 & 0\\ \omega_d/2\xi_d k_d & 0 & 0 & 0\\ 0 & 0 & -\omega_{ff} & 0\\ 0 & 0 & 0 & -\omega_q\end{bmatrix}, B_c = \begin{bmatrix}0 & 0\\ 0 & 0\\ -\omega_f k_f & 0\\ 0 & \omega_q k_q\end{bmatrix},$$

$$B_{cw} = [2\xi_d\omega_d k_d \quad 0 \quad 0 \quad 0]^T,$$

$$C_c = \begin{bmatrix}1 & 0 & 0 & 0\\ 0 & 0 & 1 & 1\end{bmatrix}.$$

- **Final State-Space Models**

$$A_{conv_{un}} =$$

$$\begin{bmatrix}A_p + B_p(D_iD_o + D_{i1}) & B_p & B_pD_iC_o & [-B_p(\delta_{iw} + D_i\delta_i - (D_iD_o + D_{i1})\delta_v) \quad 0_{2\times1}]\\ B_iD_o & 0_{2\times2} & B_iC_o & [B_iD_o\delta_v - B_i\delta_i \quad 0_{2\times1}]\\ B_o & 0_{1\times2} & 0 & [B_o\delta_v \quad 0]\\ B_\delta & 0_{2\times2} & 0_{2\times1} & A_\delta + [B_\delta\delta_v \quad 0_{2\times1}]\end{bmatrix}_{7\times7},$$

$$B_{conv_{un}} = \begin{bmatrix}-B_p - B_pD_i\\ -B_i\\ 0_{3\times2}\end{bmatrix}, B_{conv1_{un}} = \begin{bmatrix}-B_pD_i\\ -B_i\\ 0_{3\times2}\end{bmatrix}, C_{conv_{un}} = \begin{bmatrix}1 & 0 & 0_{1\times5}\\ 0 & 1 & 0_{1\times5}\end{bmatrix},$$

$$A_{tot_{un}} = \begin{bmatrix}A_{conv_{un}} & B_{conv_{un}}\\ [B_g \quad 0_{2\times5}] & A_g\end{bmatrix}_{9\times9}.$$

$$A_{tot_{comp}} = \begin{bmatrix} A_{conv_{comp}} & B_{conv_{comp}} \\ [B_g \quad 0_{2\times 9}] & A_g \end{bmatrix}_{13\times 13}$$, where

$$A_{conv_{comp}} = \begin{bmatrix} A_{conv_{un}} & B_{conv1_{un}} C_c \\ \begin{pmatrix} [B_c + B_{cw} D_\delta \quad 0_{4\times 3} \quad B_{cw} C_\delta] \\ +[0_{4\times 5} \quad B_c \delta_v + B_{cw} D_\delta \delta_v \quad 0_{4\times 1}] \end{pmatrix} & A_c \end{bmatrix}_{11\times 11}, B_{conv_{comp}} = \begin{bmatrix} B_{conv_{un}} \\ 0_{4\times 2} \end{bmatrix}.$$

Appendix A6

A6.1 Exact Source Admittance of the VSC in the Islanded Mode of Operation

$$[C1] = \begin{bmatrix} \frac{R_f+sL_f+G_i(s)}{G_i(s)} & 0 \\ 0 & \frac{R_f+sL_f+G_i(s)}{G_i(s)} \end{bmatrix}, [C2] = \begin{bmatrix} \frac{-I_q^{\circ}L_f}{G_i(s)} & 0 \\ \frac{I_d^{\circ}L_f}{G_i(s)} & 0 \end{bmatrix},$$

$$[V1] = \begin{bmatrix} -G_v(s) & -\omega_s^* C_f \\ \omega_s^* C_f & -G_v(s) \end{bmatrix}, [V2] = \begin{bmatrix} H & 0 \\ 0 & H \end{bmatrix}, [V3] = \begin{bmatrix} 0 & G_v(s) \\ 0 & 0 \end{bmatrix}, [T1] = \begin{bmatrix} 1 & 0 \\ 0 & 1 \end{bmatrix},$$

$$[T2] = \begin{bmatrix} sC_f & -\omega_s^* C_f \\ \omega_s^* C_f & sC_f \end{bmatrix}, [T3] = \begin{bmatrix} 0 & 0 \\ V_{od}^{\circ} C_f & 0 \end{bmatrix},$$

$$[P1] = \begin{bmatrix} -1.5(m+m_d s)G_p(s)I_{od}^o & -1.5(m+m_d s)G_p(s)I_{oq}^o \\ -1.5(n+n_d s)G_q(s)I_{oq}^o & 1.5(n+n_d s)G_q(s)I_{od}^o \end{bmatrix},$$

$$[P2] = \begin{bmatrix} -1.5(m+m_d s)G_p(s)V_{od}^o & 0 \\ 0 & -1.5(n+n_d s)G_q(s)V_{od}^o \end{bmatrix},$$

$$[V_s] = [V1] - [C1][T2] + [V3][P1] - [C1][T3][P1] - [C2][P1] ,$$

$$[I_s] = [C1][T3][P2] + [C2][P2] - [V3][P2] - [V2] + [C1][T1].$$

A6.2 Exact Source Admittance of the VSC Considering the Reference Frame Transformation

$$[T_\delta] = \begin{bmatrix} \cos\delta_j^o & \sin\delta_j^o \\ -\sin\delta_j^o & \cos\delta_j^o \end{bmatrix},$$

$$[T_v] = \begin{bmatrix} T_{v,11} \\ T_{v,21} \end{bmatrix} = \begin{bmatrix} -V_{od}^o \sin\delta_j^o + V_{oq}^o \cos\delta_j^o \\ -V_{od}^o \cos\delta_j^o - V_{oq}^o \sin\delta_j^o \end{bmatrix},$$

$$[T_i] = \begin{bmatrix} T_{i,11} \\ T_{i,21} \end{bmatrix} = \begin{bmatrix} -I_{odj}^o \sin\delta_j^o - I_{oqj}^o \cos\delta_j^o \\ I_{odj}^o \cos\delta_j^o - I_{oq}^o \sin\delta_j^o \end{bmatrix}.$$

A6.3 Approximated Source Admittance of the VSC in the Isolated AC Microgrid

$[V_s^{\sim}] = [V1] - [C1][T2]$, $[I_s^{\sim}] = -[V2] + [C1][T1]$;

where $\pm\omega^* C_f = 0$ in $[V1]$ and $[T2]$.

A6.4 Small-Signal Admittance Model of the Direct-Online Induction Motor

$[S1] = \begin{bmatrix} R_s + sL_s & -\omega L_s \\ \omega L_s & R_s + sL_s \end{bmatrix}$, $[S2] = \begin{bmatrix} sL_m & -\omega L_m \\ \omega L_m & sL_m \end{bmatrix}$, $[S3] = \begin{bmatrix} -I^{\circ}_{sq}L_s - I^{\circ}_{rq}L_m \\ I^{\circ}_{sd}L_s + I^{\circ}_{rd}L_m \end{bmatrix}$,

$[R1] = \begin{bmatrix} -(R_r + sL_r) & (\omega - \omega_r)L_r \\ -(\omega - \omega_r)L_r & -(R_r + sL_r) \end{bmatrix}$, $[R2] = \begin{bmatrix} sL_m & -(\omega - \omega_r)L_m \\ (\omega - \omega_r)L_m & sL_m \end{bmatrix}$,

$[R3] = \begin{bmatrix} -I^{\circ}_{sq}L_m - I^{\circ}_{rq}L_r \\ I^{\circ}_{sd}L_m + I^{\circ}_{rd}L_r \end{bmatrix}$, $[R4] = \begin{bmatrix} I^{\circ}_{sq}L_m + I^{\circ}_{rq}L_r \\ -I^{\circ}_{sd}L_m - I^{\circ}_{rd}L_r \end{bmatrix}$, $[M1] = \begin{bmatrix} -\frac{3}{4}\frac{PL_m}{Js}I^{\circ}_{rq} & \frac{3}{4}\frac{PL_m}{Js}I^{\circ}_{rd} \end{bmatrix}$,

$[M2] = \begin{bmatrix} \frac{3}{4}\frac{PL_m}{Js}I^{\circ}_{sq} & -\frac{3}{4}\frac{PL_m}{Js}I^{\circ}_{sd} \end{bmatrix}$, $[M3] = \begin{bmatrix} \frac{-1}{Js} \end{bmatrix}$.

A6.5 State-Space Model of the Direct Online Induction Motor

$\Delta X^{\cdot} = A\,\Delta X + B\,\Delta U$; where $[\Delta X]^T$ is the state vector and equals $[\Delta I_{sq}\ \Delta I_{sd}\ \Delta I_{rq}\ \Delta I_{rd}\ \Delta\omega_r]$; $[\Delta U]^T$ is the input vector and equals $[\Delta V_{sq}\ \Delta V_{sd}\ \Delta V_{rq}\ \Delta V_{rd}\ \Delta T_L]$; $A = -E^{-1}F$; $B = E^{-1}$.

$$E = \begin{bmatrix} L_s & 0 & L_m & 0 & 0 \\ 0 & L_s & 0 & L_m & 0 \\ L_m & 0 & L_r & 0 & 0 \\ 0 & L_m & 0 & L_r & 0 \\ 0 & 0 & 0 & 0 & -J \end{bmatrix},$$

$$F = \begin{bmatrix} R_s & \omega L_s & 0 & \omega L_m & 0 \\ -\omega L_s & R_s & -\omega L_m & 0 & 0 \\ 0 & (\omega - \omega_r)L_m & R_r & (\omega - \omega_r)L_r & -I^{\circ}_{sd}L_m - I^{\circ}_{rd}L_r \\ -(\omega - \omega_r)L_m & 0 & -(\omega - \omega_r)L_r & R_r & I^{\circ}_{sq}L_m + I^{\circ}_{rq}L_r \\ \frac{3}{4}PL_mI^{\circ}_{rd} & -\frac{3}{4}PL_mI^{\circ}_{rq} & -\frac{3}{4}PL_mI^{\circ}_{sd} & \frac{3}{4}PL_mI^{\circ}_{sq} & 0 \end{bmatrix}$$

A6.6 Actively Compensated Source Admittance of the VSC

$[V1]^{comp} = \begin{bmatrix} (C_1(s) - 1)G_v(s) + C_2(s) & -\omega^*_s C_f \\ \omega^*_s C_f & (C_1(s) - 1)G_v(s) + C_2(s) \end{bmatrix}$,

$[I^{comp}_s]$ and $[V^{comp}_s]$ are equal to $[I_s]$ and $[V_s]$ but replace $[V1]$ by $[V1]^{comp}$.

A6.7 System Parameters

- Simulink Model

VSC:*150 kVA, 460 V, 60 Hz,* L_f = 2 mH, R_f = 0.15 Ω, C_f = 45 μF, $m = 0.8\times10^{-5}$, $n = 1\times10^{-4}$, ω_c = 30 rad/sec, H = 0.7, $G_v(s)$= 0.165 + 400/s, $G_i(s)$= 50 + 15300/s.

IM: *200 hP, 460 V, 60Hz, 1785 rpm,* R_s = 0.01818 Ω, L_m = 9.415 mH, $L_s = L_r$ = (0.19+L_m) mH, R_r = 0.009956 Ω, J = 2.6 kg.m^2, P = 2.

- Experimental Setup

VSI: 250 *Vac,* 350 *Vdc,* F_{sw} = 10 *kHz,* L = 1.2 *mH,* R = 0.2 *Ω,* C = 50 *μF,* L_c = 1.2 *mH,* R_c = 0.2 *Ω,* C_{dc} = 2040 *μF,* ac voltage controller = *1 + 1/s,* ac current controller = *0.6 + 0.01/s.*
Resistive Load*:* 250 *W,* 500 *W at* 208 *Vac.*
IM: 0.25hP*,* three-phase*,* 208 *V,* 60 *Hz,* 1725 *rpm.*

Appendix A7

A7.1 Large Signal Model of the Hybrid AC/DC System

In the following; $\vec{u}_{\boldsymbol{n}} = \left(U_{\boldsymbol{dn}} + \boldsymbol{j}U_{\boldsymbol{qn}}\right)e^{j\delta_n(t)} = \boldsymbol{U_n}e^{j\delta_{\boldsymbol{n}}(t)}$ is a three-phase space-vector that is decomposed into the equivalent d-q components, in the rotating reference frame; $\delta_{\boldsymbol{n}}(t)$ is the orientation angle and is obtained from (7.1) in the droop-controlled VSCs, and from a PLL in the interconnecting VSCs or the PQ-controlled DGs. The system model is based on the power circuits in Figure 7.2.

- VSI in the AC Subgrid, "$\boldsymbol{i}$" Inverter, Dispatchable DG

Power Circuit:

$$\vec{v}_{ti} - \vec{v}_{oi} = r_i\vec{\imath}_i + l_i\frac{d\vec{\imath}_i}{dt},$$

$$\vec{v}_{oi} - \vec{v} = r_{oi}\vec{\imath}_{oi} + l_{oi}\frac{d\vec{\imath}_{oi}}{dt},$$

$$c_i\frac{d\vec{v}_{oi}}{dt} = \vec{\imath}_i - \vec{\imath}_{oi},$$

$$\vec{v} = r_{ac}\vec{\imath}_l$$

Current and Voltage Control:

$$\boldsymbol{V_{ti}} = (\boldsymbol{I_i^*} - \boldsymbol{I_i})\underbrace{\left(K_{PCi} + \frac{K_{ICi}}{s}\right)}_{G_{Ci}(s)} + \boldsymbol{j}\omega_i l_i \boldsymbol{I_i} + \boldsymbol{V_{oi}}$$

$$\boldsymbol{I_i^*} = (\boldsymbol{V_{oi}^*} - \boldsymbol{V_{oi}})\underbrace{\left(K_{PVi} + \frac{K_{IVi}}{s}\right)}_{G_{Vi}(s)} + \boldsymbol{j}\omega_i c_i \boldsymbol{V_{oi}} + H_i\boldsymbol{I_{oi}}$$

Power Calculation:

$$p_i + \boldsymbol{j}q_i = 1.5\left(V_{odi} - jV_{oqi}\right)\boldsymbol{I_{oi}},$$

$$P_i + \boldsymbol{j}Q_i = \frac{\omega_{fi}}{s + \omega_{fi}}(p_i + \boldsymbol{j}q_i)$$

- DC/DC Converter in the DC Subgrid, "j" Converter

Power Circuit:

$$V_{tj} - V_{oj} = R_j I_j + L_j \frac{dI_j}{dt},$$

$$V_{oj} - V_{dc} = R_{oj} I_{oj} + L_{oj} \frac{dI_{oj}}{dt},$$

$$C_j \frac{dV_{oj}}{dt} = I_j - I_{oj},$$

$$V_{dc} = R_{dc} I_{dc}.$$

Current and Voltage Control:

$$V_{tj} = \left(I_j^* - I_j\right) \underbrace{\left(K_{PCj} + \frac{K_{ICj}}{s}\right)}_{G_{Cj}(s)}$$

$$I_j^* = \left(V_{oj}^* - V_{oj}\right) \underbrace{\left(K_{PVj} + \frac{K_{IVj}}{s}\right)}_{G_{Vj}(s)} + H_j I_{oj}$$

Power Calculation:

$$P_j = \frac{\omega_{fj}}{s + \omega_{fj}} V_{oj} I_{oj}$$

- Interconnecting VSC, "k" Converter

The following model is for the rectification mode. The current direction is reversed for the inversion operation.

Power Circuit:

$$\vec{v}_k - \vec{v}_{tk} = r_k \vec{\imath}_k + l_k \frac{d\vec{\imath}_k}{dt},$$

$$C_k \frac{dV_{ok}}{dt} = 1.5\left(m_{dk} I_{dk} + m_{qk} I_{qk}\right) - I_{ok},$$

$$V_{ok} - V_{dc} = R_{ok} I_{ok} + L_{ok} \frac{dI_{ok}}{dt}$$

Current Control:

$$\boldsymbol{V_{tk}} = -(\boldsymbol{I_k^*} - \boldsymbol{I_k})\underbrace{\left(K_{PCk} + \frac{K_{ICk}}{s}\right)}_{G_{Ck}(s)} - j\omega_k l_k \boldsymbol{I_k} + \boldsymbol{V_k},$$

$$I_{dk}^* = \frac{P_{ic,k}^*}{1.5V_{dk}^{\circ}},$$

$$I_{qk}^* = 0.$$

Power Calculation:

$$P_{ic,k}^{meas} = \frac{\omega_{fk}}{s + \omega_{fk}} V_{ok} I_{ok}$$

A7.2 Small-Signal State-Space Model of the Hybrid AC/DC System

In the following, X, U are the state and input vectors; A and B are the state and input matrices; Δ represents a small perturbation of the variable.

- VSC in the AC Subgrid

$$\Delta \dot{X}_{vsi} = A_{vsi}\Delta X_{vsi} + B_{vsi}\Delta U_{vsi}$$

where

$\Delta X_{vsi} =$

$[\Delta I_{di} \quad \Delta I_{qi} \quad \Delta I_{odi} \quad \Delta I_{oqi} \quad \Delta V_{odi} \quad \Delta V_{oqi} \quad \Delta P_{ac} \quad \Delta Q \quad \Delta\delta_i \quad \Delta\varphi_{vdi} \quad \Delta\varphi_{vqi} \quad \Delta\varphi_{cdi} \quad \Delta\varphi_{cqi}]^T$

and $\Delta U_{vsi} = [\Delta I_{dk} \quad \Delta I_{qk}]^T$ such that the pairs $(\Delta\varphi_{vdi}, \Delta\varphi_{vqi})$, $(\Delta\varphi_{cdi}, \Delta\varphi_{cqi})$ represent the state of the integrator of the PI voltage and current controllers in the d-q reference frame. The state and input matrices are:

$A_{vsi} =$

$$\begin{bmatrix} \begin{pmatrix} A_p^{ac} + B_{p1}^{ac}D_{i1}^{ac}D_{v2}^{ac} + B_{p1}^{ac}D_{i2}^{ac} \\ +[0_{6\times2} \quad B_{p2}^{ac}R_{ac} \quad 0_{6\times2}] \end{pmatrix}_{6\times6} & \begin{pmatrix} B_{p1}^{ac}D_{i1}^{ac}D_{v1}^{ac}C_d^{ac} \\ +[-m_{ac}B_{p3}^{ac} \quad 0_{6\times2}] \end{pmatrix}_{6\times3} & \left(B_{p1}^{ac}D_{i1}^{ac}C_v^{ac}\right)_{6\times2} & \left(B_{p1}^{ac}C_i^{ac}\right)_{6\times2} \\ (B_d^{ac})_{3\times6} & (A_d^{ac})_{3\times3} & 0_{3\times2} & 0_{3\times2} \\ [0_{2\times4} \quad B_{v2}^{ac}]_{2\times6} & (B_{v1}^{ac}C_d^{ac})_{2\times3} & 0_{2\times2} & 0_{2\times2} \\ (B_{i1}^{ac}D_{v2}^{ac} + B_{i2}^{ac})_{2\times6} & (B_{i1}^{ac}D_{v1}^{ac}C_d^{ac})_{2\times3} & (B_{i1}^{ac}C_v^{ac})_{2\times3} & 0_{2\times2} \end{bmatrix},$$

$B_{vsi} = \begin{bmatrix} \left(-B_{p2}^{ac} R_{ac}\right)_{6\times 2} \\ 0_{7\times 2} \end{bmatrix}$, which are obtained in terms of the state-space models of the power circuit and controllers, as following:

State-Space Model of the Power Circuit of the VSC in the AC Subgrid:

$$A_p^{ac} = \begin{bmatrix} -r_i/l_i & \omega_i^{\circ} & 0 & 0 & -1/l_i & 0 \\ -\omega_i^{\circ} & -r_i/l_i & 0 & 0 & 0 & -1/l_i \\ 0 & 0 & -r_{oi}/l_{oi} & \omega_i^{\circ} & 1/l_{oi} & 0 \\ 0 & 0 & -\omega_i^{\circ} & -r_{oi}/l_{oi} & 0 & 1/l_{oi} \\ 1/c_i & 0 & -1/c_i & 0 & 0 & \omega_i^{\circ} \\ 0 & 1/c_i & 0 & -1/c_i & -\omega_i^{\circ} & 0 \end{bmatrix}, B_{p1}^{ac} = \begin{bmatrix} 1/l_i & 0 \\ 0 & 1/l_i \\ 0_{4\times 1} & 0_{4\times 1} \end{bmatrix}, B_{p2}^{ac} =$$

$$\begin{bmatrix} 0_{2\times 1} & 0_{2\times 1} \\ -1/l_{oi} & 0 \\ 0 & -1/l_{oi} \\ 0_{2\times 1} & 0_{2\times 1} \end{bmatrix}, B_{p3}^{ac} = \begin{bmatrix} I_{qi}^{\circ} \\ -I_{di}^{\circ} \\ I_{oqi}^{\circ} \\ -I_{odi}^{\circ} \\ V_{oqi}^{\circ} \\ -V_{odi}^{\circ} \end{bmatrix}.$$

State-Space Model of the Droop Loop of the VSC in the AC Subgrid:

$$A_d^{ac} = \begin{bmatrix} -\omega_{fi} & 0 & 0 \\ 0 & -\omega_{fi} & 0 \\ -m_{aci} & 0 & 0 \end{bmatrix},$$

$$B_d^{ac} = \begin{bmatrix} 0 & 0 & 1.5\omega_{fi} V_{odi}^{\circ} & 1.5\omega_{fi} V_{oqi}^{\circ} & 1.5\omega_{fi} I_{odi}^{\circ} & 1.5\omega_{fi} I_{oqi}^{\circ} \\ 0 & 0 & -1.5\omega_{fi} V_{oqi}^{\circ} & 1.5\omega_{fi} V_{odi}^{\circ} & 1.5\omega_{fi} I_{oqi}^{\circ} & -1.5\omega_{fi} I_{odi}^{\circ} \\ 0 & 0 & 0 & 0 & 0 & 0 \end{bmatrix}, C_d^{ac} = \begin{bmatrix} 0 & -n_{aci} & 0 \\ 0 & 0 & 0 \end{bmatrix}.$$

State-Space Model of the Voltage Controller of the VSC in the AC Subgrid:

$$B_{v1}^{ac} = \begin{bmatrix} K_{IVi} & 0 \\ 0 & K_{IVi} \end{bmatrix}, B_{v2}^{ac} = -B_{v1}^{ac}, C_v^{ac} = I_{2\times 2}, D_{v1}^{ac} = \begin{bmatrix} K_{PVi} & 0 \\ 0 & K_{PVi} \end{bmatrix},$$

$$D_{v2}^{ac} = \begin{bmatrix} 0 & 0 & H_i & 0 & -K_{PVi} & -\omega_i^{\circ} c_i \\ 0 & 0 & 0 & H_i & \omega_i^{\circ} c_i & -K_{PVi} \end{bmatrix}.$$

State-Space Model of the Current Control of the VSC in the AC Subgrid:

$B_{i1}^{ac} = \begin{bmatrix} K_{ICi} & 0 \\ 0 & K_{ICi} \end{bmatrix}$, $B_{i2}^{ac} = \begin{bmatrix} -K_{ICi} & 0 & 0 & 0 & 0 & 0 \\ 0 & -K_{ICi} & 0 & 0 & 0 & 0 \end{bmatrix}$, $D_{i1}^{ac} = \begin{bmatrix} K_{PCi} & 0 \\ 0 & K_{PCi} \end{bmatrix}$,

$D_{i2}^{ac} = \begin{bmatrix} -K_{PCi} & -\mathring{\omega}_i l_i & 0 & 0 & 1 & 0 \\ -\mathring{\omega}_i l_i & -K_{PCi} & 0 & 0 & 0 & 1 \end{bmatrix}$, $C_i^{ac} = I_{2\times 2}$.

Model of the AC Resistive Load in the AC Subgrid:

$R_{ac} = \begin{bmatrix} r_{ac} & 0 \\ 0 & r_{ac} \end{bmatrix}$.

- DC/DC Converter in the DC Subgrid

$$\Delta \dot{X_{dc}} = A_{dc}\Delta X_{dc} + B_{dc}\Delta U_{dc}$$

where $\Delta X_{dc} = [\Delta I_j \quad \Delta I_{oj} \quad \Delta V_{oj} \quad \Delta P_{dc} \quad \Delta\varphi_{Vj} \quad \Delta\varphi_{Cj}]^T$, $\Delta U_{dc} = \Delta V_{dc}$ and $\Delta\varphi_{Vj}$, $\Delta\varphi_{Cj}$ represent the state of the integrator of the PI voltage and current controllers. The state and input matrices are:

$A_{dc} =$

$$\begin{bmatrix} \begin{pmatrix} A_p^{dc} + \begin{bmatrix} -B_{p1}^{dc}K_{PCj} & 0_{3\times 2} \end{bmatrix} \\ +\begin{bmatrix} 0_{3\times 1} & K_{PCj}H_jB_{p1}^{dc} & 0_{3\times 1} \end{bmatrix} \end{pmatrix}_{3\times 3} & \left(-m_{dcj}K_{PCj}K_{PVj}B_{p1}^{dc}\right)_{3\times 1} & \left(B_{p1}^{dc}K_{PCj}\right)_{3\times 1} & \left(B_{p1}^{dc}\right)_{3\times 1} \\ [0 \quad \omega_{fj}V_{oj} \quad \omega_{fj}I_{oj}]_{1\times 3} & \left(-\omega_f\right)_{1\times 1} & 0 & 0 \\ \begin{bmatrix} 0 & 0 & 0 \\ -K_{ICj} & H_jK_{ICj} & 0 \end{bmatrix}_{2\times 3} & \begin{bmatrix} -m_{dcj}K_{IVj} \\ -m_{dcj}K_{PVj}K_{ICj} \end{bmatrix}_{2\times 1} & \begin{bmatrix} 0 \\ K_{ICj} \end{bmatrix}_{2\times 1} & 0_{2\times 1} \end{bmatrix},$$

$$B_{dc} = \begin{bmatrix} \begin{pmatrix} -B_{p1}^{dc}K_{PVj}K_{PCj} \\ +B_{p2}^{dc} \end{pmatrix}_{3\times 1} \\ 0 \\ -K_{IVj} \\ -K_{PVj}K_{ICj} \end{bmatrix}.$$

where,

$$A_p^{dc} = \begin{bmatrix} -R_j/L_j & 0 & -1/L_j \\ 0 & -R_{oj}/L_{oj} & -1/L_{oj} \\ 1/C_j & -1/C_j & 0 \end{bmatrix}, B_{p1}^{dc} = \begin{bmatrix} 1/L_j \\ 0 \\ 0 \end{bmatrix}, B_{p2}^{dc} = \begin{bmatrix} 0 \\ -1/L_{oj} \\ 0 \end{bmatrix}.$$

- Interfacing Converter (Rectification Mode)

$$\Delta \dot{X_{ic}} = A_{ic}\Delta X_{ic} + B_{ic1}\Delta U_{ic1} + B_{ic2}\Delta U_{ic2} + B_{ic3}\Delta U_{ic3} + B_{ic4}\Delta U_{ic4}$$

where $\Delta X_{ic} = [\Delta I_{dk} \quad \Delta I_{qk} \quad \Delta V_{dck} \quad \Delta P_{ick} \quad \Delta P_{ick}^* \quad \Delta\varphi_{cdk} \quad \Delta\varphi_{cqk}]^T$, $\Delta U_{ic1} = \Delta P_{ac}$, $\Delta U_{ic2} = [\Delta V_{dk} \quad \Delta V_{qk}]^T$, $\Delta U_{ic3} = \Delta I_{ok}$, $\Delta U_{ic4} = \Delta P_{dc}$ such that the pairs $(\Delta\varphi_{cdk}, \Delta\varphi_{cqk})$ represent the state of the integrator of the PI current controllers in the d-q reference frame; $[\Delta V_{dk} \quad \Delta V_{qk}]^T = R_{ac}[\Delta I_{odi} \quad \Delta I_{oqi}]^T - R_{ac}[\Delta I_{dk} \quad \Delta I_{qk}]^T$, $\Delta I_{ok} = \frac{\Delta V_{dck}}{R_{dc}} - \Delta I_{oj}$. The state and input matrices are:

$$A_{ic} = \begin{bmatrix} \begin{pmatrix} A_p^{ic} + \begin{bmatrix} B_{p1}^{ic}D_{i1}^{ic} & 0_{3\times1} \end{bmatrix} \\ +\begin{bmatrix} 0_{3\times2} & B_{p1}^{ic}D_{i4}^{ic} \end{bmatrix} \end{pmatrix}_{3\times3} & \left(B_{p1}^{ic}D_{i2}^{ic}C_c^{ic}\right)_{3\times2} & \left(B_{p1}^{ic}C_i^{ic}\right)_{3\times2} \\ [0_{2\times2} \quad B_{c2}^{ic}]_{2\times3} & \left(A_c^{ic}\right)_{2\times2} & 0_{2\times2} \\ \begin{bmatrix} B_{i1}^{ic} & 0_{2\times1} \end{bmatrix}_{2\times3} & \left(B_{i2}^{ic}C_c^{ic}\right)_{2\times2} & 0_{2\times2} \end{bmatrix},$$

$$B_{ic1} = \begin{bmatrix} -m_{ack}B_{p3}^{ic} \\ 0_{2\times1} \\ 0_{2\times1} \end{bmatrix}, B_{ic2} = \begin{bmatrix} B_{p2}^{ic} + B_{p1}^{ic}D_{i3}^{ic} \\ 0_{2\times2} \\ 0_{2\times2} \end{bmatrix}, B_{ic3} = \begin{bmatrix} B_{p4}^{ic} \\ B_{c1}^{ic} \\ 0_{2\times1} \end{bmatrix},$$

$$B_{ic4} = \begin{bmatrix} 0_{3\times1} \\ B_{c3}^{ic} \\ 0_{2\times1} \end{bmatrix}.$$

which are obtained in terms of the state-space models of the power circuit and controllers, as follows.

State-Space Model of the Power Circuit of the Interconnecting VSC:

$$A_p^{ic} = \begin{bmatrix} -r_k/l_k & \omega_k^\circ & -m_{dk}^\circ/l_k \\ -\omega_k^\circ & -r_k/l_k & -m_{qk}^\circ/l_k \\ 1.5m_{dk}^\circ/C_k & 1.5m_{qk}^\circ/C_k & 0 \end{bmatrix}, B_{p1}^{ic} = \begin{bmatrix} -V_{dck}^\circ/l_k & 0 \\ 0 & -V_{dck}^\circ/l_k \\ 1.5I_{dk}^\circ/C_k & 1.5I_{qk}^\circ/C_k \end{bmatrix}, B_{p2}^{ic} = \begin{bmatrix} 1/l_k & 0 \\ 0 & 1/l_k \\ 0 & 0 \end{bmatrix}, B_{p3}^{ic} = \begin{bmatrix} I_{qk}^\circ \\ -I_{dk}^\circ \\ 0 \end{bmatrix}, B_{p4}^{ic} = \begin{bmatrix} 0 \\ 0 \\ -1/C_k \end{bmatrix}.$$

State-Space Model of the Current Control of the Interconnecting VSC:

$B_{i1}^{ic} = \begin{bmatrix} K_{ICk} & 0 \\ 0 & K_{ICk} \end{bmatrix}$, $B_{i2}^{ic} = -B_{i1}^{ic}$, $C_{i}^{ic} = \begin{bmatrix} 1/V_{dck}^{\circ} & 0 \\ 0 & 1/V_{dck}^{\circ} \end{bmatrix}$, $D_{i1}^{ic} = \begin{bmatrix} K_{PCk}/V_{dck}^{\circ} & \omega_k^{\circ} l_k/V_{dck}^{\circ} \\ -\omega_k^{\circ} l_k/V_{dck}^{\circ} & K_{PCk}/V_{dck}^{\circ} \end{bmatrix}$,

$D_{i2}^{ic} = \begin{bmatrix} -K_{PCk}/V_{dck}^{\circ} & 0 \\ 0 & -K_{PCk}/V_{dck}^{\circ} \end{bmatrix}$, $D_{i3}^{ic} = \begin{bmatrix} 1/V_{dck}^{\circ} & 0 \\ 0 & 1/V_{dck}^{\circ} \end{bmatrix}$, $D_{i4}^{ic} = \begin{bmatrix} -m_{dk}^{\circ}/V_{dck}^{\circ} \\ -m_{qk}^{\circ}/V_{dck}^{\circ} \end{bmatrix}$.

State-Space Model of the Centralized Power Control of the Interconnecting VSC:

$A_{c}^{ic} = \begin{bmatrix} -\omega_{fk} & 0 \\ 1/\tau_d & -1/\tau_d \end{bmatrix}$, $B_{c1}^{ic} = \begin{bmatrix} \omega_{fk} V_{dck}^{\circ} \\ 0 \end{bmatrix}$, $B_{c2}^{ic} = \begin{bmatrix} \omega_{fk} I_{ok}^{\circ} \\ 0 \end{bmatrix}$, $B_{c3}^{ic} = \begin{bmatrix} 0 \\ 1/\tau_d \end{bmatrix}$, $C_{c}^{ic} =$
$\begin{bmatrix} 0 & 1/1.5V_{dk}^{\circ} \\ 0 & 0 \end{bmatrix}$.

- Interfacing Converter (Inversion Mode)

Similar to the inversion mode but exchanging the following matrices:

$B_{ic1} = \begin{bmatrix} -m_{ack} B_{p3}^{ic} \\ B_{c3}^{ic} \\ 0_{2\times1} \end{bmatrix}$, $B_{ic4} = [0_{7\times1}]$, $B_{c3}^{ic} = \begin{bmatrix} 0 \\ -1/\tau_d \end{bmatrix}$.

- Entire System Model

$$[\Delta\dot{X}_{vsi} \quad \Delta\dot{X}_{ic} \quad \Delta\dot{X}_{dc}]^T = \left[A_{sys}\right]_{26\times26} [\Delta X_{vsi} \quad \Delta X_{ic} \quad \Delta X_{dc}]^T$$

where

$A_{sys} =$

$$\begin{bmatrix} (A_{vsi})_{13\times13} & [B_{vsi} \quad 0_{13\times5}]_{13\times7} & 0_{13\times6} \\ \begin{pmatrix} [0_{7\times6} \quad B_{ic1} \quad 0_{7\times6}] \\ +[0_{7\times2} \quad B_{ic2}R_{ac} \quad 0_{7\times9}] \end{pmatrix}_{7\times13} & \begin{pmatrix} A_{ic} + [-B_{ic2}R_{ac} \quad 0_{7\times5}] \\ +[0_{7\times2} \quad B_{ic3}/R_{dc} \quad 0_{7\times4}] \end{pmatrix}_{7\times7} & [0_{7\times1} \quad -B_{ic3} \quad 0_{7\times1} \quad B_{ic4} \quad 0_{7\times2}]_{7\times6} \\ 0_{6\times13} & [0_{6\times2} \quad B_{dc} \quad 0_{6\times4}]_{6\times7} & (A_{dc})_{6\times6} \end{bmatrix}.$$

A7.3 System Parameters

- VSC-1, 2: 1 MVA, $v_{ac} = 690$ V, $V_{dc} = 2500$ V, $F_{sw} = 2$ kHz, $r_i = 0.01\ \Omega$, $l_i = 1$ mH, $c_i = 50$ μF, $G_{Ci}(s) = 1.5 + \frac{175}{s}$, $G_{Vi}(s) = 0.1 + \frac{50}{s}$.
- DC/DC converters-1, 2: 1 MW, $V_{dc} = 3500/2500$ V, $F_{sw} = 2$ kHz, $R_j = 0.05\ \Omega$, $L_j = 1$ mH, $C_j = 4700$ μF, $G_{Cj}(s) = 2.5 + \frac{250}{s}$, $G_{Vj}(s) = 4 + \frac{19.2}{s}$.
- PQ-Controlled VSI: 0.3 MW, $v_{ac} = 690$ V, $V_{dc} = 2500$ V, $F_{sw} = 2$ kHz, $r_i = 0.01\ \Omega$, $l_i = 1$ mH, $C_i = 4700$ μF, $G_{Ci}(s) = 2.1 + \frac{21}{s}$, $G_{Vdci}(s) = 0.0003 + \frac{0.01}{s}$.
- Interconnecting VSC: 1 MW, $v_{ac} = 690$ V, $V_{dc} = 2500$ V, $F_{sw} = 2$ kHz, $r_k = 0.01\ \Omega$, $l_k = 1$ mH, $G_{Ck}(s) = 1.55 + \frac{250}{s}$.